
Moiré physics in the semiconductor MoSe₂/WS₂ heterostructure

Borislav Polovnikov



München, 2024

**Moiré physics in the semiconductor
MoSe₂/WS₂ heterostructure**

Borislav Polovnikov

Dissertation
an der Fakultät für Physik
der Ludwig-Maximilians-Universität
München

vorgelegt von
Borislav Polovnikov
aus Minsk, Belarus

München, den 15. April 2024

Erstgutachter: Prof. Dr. Alexander Högele

Zweitgutachter: Prof. Dr. Jonathan Finley

Tag der mündlichen Prüfung: 13. Juni 2024

Zusammenfassung

Atomar dünne Übergangsmetall-Dichalkogenide sind Halbleiter mit direkter Bandlücke und stellen eine sehr vielversprechende Plattform sowohl für optoelektronische Anwendungen als auch für die Quantengrundlagenforschung dar. In Monolagen zeichnen sie sich durch eine starke Licht-Materie-Kopplung aus, die durch fest gebundene Elektron-Loch-Paare, sogenannte Exzitonen, vermittelt wird. Mehrschichtige Heterostrukturen hingegen haben sich als wertvolle Modellsysteme für die Realisierung von korrelierten elektronischen Zuständen etabliert. Der geometrische Moiré-Effekt in gestapelten van der Waals Heterostrukturen spielt bei dieser Entwicklung eine wichtige Rolle, da kritische Parameter des Moiré-Potentials über die Materialien der einzelnen Lagen und deren gegenseitige Rotation kontrolliert werden können.

Die $\text{MoSe}_2/\text{WS}_2$ Heterostruktur zeichnet sich durch nahezu resonante Leitungsbandkanten aus, was starke Hybridisierungseffekte und elektrostatische Kontrolle ihres energetischen Grundzustands ermöglicht. Bei kleinen Verdrehungswinkeln hat das Moiré-Potential sogenannte Moiré Exzitonen zur Folge, die optische Untersuchungen von elektronischen Zuständen mit Signaturen des Fermi-Hubbard-Modells, korrelationsinduzierten Magnetismus oder korrelierter Mott-Isolator Zustände ermöglichen. Das komplexe Zusammenspiel von Intra- und Interlagen-Effekten hat jedoch lange Zeit die grundlegende Bandstruktur und die Eigenschaften der Moiré Exzitonen verschleiert. In dieser Arbeit werden diese Fragen im Rahmen einer umfassenden theoretischen und experimentellen Studie von $\text{MoSe}_2/\text{WS}_2$ Heterostrukturen geklärt. Wir verwenden eine Probenarchitektur mit zwei Elektroden, die es uns erlaubt, gleichzeitig sowohl das elektrische Feld als auch die Ladungsträgerdotierung zu kontrollieren. In Kombination mit zusätzlichen Parametern wie der Temperatur oder senkrechten Magnetfeldern untersuchen wir das Verhalten der Moiré Exzitonen in einem erweiterten Parameterbereich und entwickeln theoretische Modelle, um die beobachteten experimentellen Daten zu erklären.

Zunächst charakterisieren wir die Moiré Exzitonen, indem wir ihre Dispersion mit senkrechten elektrischen Feldern in Weißlichtreflexion und Schmalband-Modulationsspektroskopie untersuchen. Wir stellen ein Kontinuumsmodell auf, das eine theoretische Beschreibung der beobachteten Exzitonen ermöglicht, und auf das wir anschließend aufbauen, um das exzitonische Verhalten als Funktion von Elektronendotierung zu untersuchen. Mittels elektrostatischer Modellierung decken wir ein bisher unbekanntes Dotierungsverhalten auf, das schichtweise abläuft, wobei das erste und zweite Elektron pro Moiré-Zelle nacheinander Moiré-Potentialminima zunächst in der MoSe_2 und dann in der WS_2 Lage besetzen. Schließlich untersuchen wir die dotierungsabhängige Spin-Suszeptibilität des entstehenden Bilagen-Elektronengitters, die auf das Auftreten von elektrostatisch abstimmbarem Ruderman-Kittel-Kasuya-Yosida-Magnetismus schließen lässt. Unsere Ergebnisse etablieren $\text{MoSe}_2/\text{WS}_2$ als ein einzigartiges System für die Erforschung von Coulomb-korrelierten Zuständen in zweischichtigen Spin-Ladungsgittern und bieten eine Motivation für zukünftige experimentelle und theoretische Arbeiten zur Vielteilchenphysik in $\text{MoSe}_2/\text{WS}_2$.

Abstract

Atomically thin Transition Metal Dichalcogenides are direct band gap semiconductors and present a very fertile ground for both optoelectronic applications and fundamental quantum research. In their monolayer limit, they are characterized by inherently strong light-matter coupling mediated by tightly bound electron-hole pairs known as excitons. Multilayer heterostructures, on the other hand, have attracted considerable interest as model systems for band engineering and implementations of previously elusive correlated electronic states. The geometric moiré interference effect in stacked van der Waals heterostructures plays an integral role in this development, since critical parameters of the long-range moiré potential can be engineered via the constituent layer materials and their rotational alignment.

The MoSe₂/WS₂ heterostructure is characterized by near-resonant alignment of its conduction band edges which implies significant hybridization effects and electrostatic tunability of its energetic ground state. For small twist angles, the presence of a moiré potential leads to the emergence of distinct moiré excitons that allow to study electronic states optically, with signatures of Fermi-Hubbard model physics, correlation-induced magnetism, or correlated Mott-insulator states. The complex interplay of intralayer exciton mixing with interlayer electron tunneling, however, has long obscured the fundamental band structure and the nature of the bright moiré excitons. In this thesis, we clarify these questions by presenting a comprehensive theoretical and experimental study of angle-aligned MoSe₂/WS₂ heterostructures. We employ a dual gate field-effect device architecture that allows us to simultaneously control both out-of-plane electric fields as well as charge carrier doping. In combination with additional tunable parameters such as temperature or perpendicular magnetic fields, we study the behavior of the moiré excitons in an extended parameter range and develop theoretical models in order to explain the observed experimental data.

First, we determine the nature of the bright moiré excitons by studying their dispersion with perpendicular electric fields in white light reflectance and narrow-band modulation spectroscopy. We present a continuum model that allows us to accurately describe the low-energy exciton physics and which we subsequently build upon to study the exciton behavior in the presence of electron doping. By means of electrostatic modeling, we establish evidence of a previously unseen charging behavior that proceeds layer-by-layer, with the first and second electron per moiré cell consecutively occupying moiré potential pockets first in the MoSe₂ and then in the WS₂ layer. Finally, we study the doping-dependent spin-susceptibility of the emerging bilayer electron lattice that suggests the presence of electrostatically tunable Ruderman-Kittel-Kasuya-Yosida magnetism. Our results establish MoSe₂/WS₂ as a unique system to explore Coulomb-correlated states in bilayer spin-charge lattices and provide compelling motivation for future experimental and theoretical work on many-body phenomena in MoSe₂/WS₂.

Contents

1	Introduction	1
2	Fundamentals of transition metal dichalcogenides	5
2.1	Overview of two-dimensional van der Waals materials	6
2.2	Basic band structure considerations: from graphene to layered semiconductors	9
2.3	Optoelectronics in transition metal dichalcogenide monolayers	12
2.3.1	Wannier-Mott excitons and the role of dielectric screening	12
2.3.2	Charged excitonic complexes	14
2.3.3	Response to external fields: excitonic valley Zeeman and Stark effects .	15
2.4	Summary	17
3	Experimental techniques	19
3.1	Sample fabrication	20
3.1.1	Essentials of nanofabrication	20
3.1.2	Field-effect devices for electric field and charge density control	22
3.2	Dilution refrigeration and low-temperature position control	23
3.3	Confocal microscopy and spectroscopy	26
3.3.1	Differential reflectance spectroscopy	26
3.3.2	Photoluminescence spectroscopy	30
3.3.3	Modulation spectroscopy	31
3.4	Experimental challenges and solutions	31
3.4.1	Landé-factors and position drift with changing magnetic field	32
3.4.2	Charge doping blockades	33
3.4.3	Data complexity and software-driven automatization for data acquisition and analysis	33
4	Theoretical models	35
4.1	Moiré geometry in bilayer van der Waals structures	35

4.2	Lattice reconstruction as an obstacle to moiré physics in commensurate bilayers	38
4.3	Continuum models for excitons in incommensurate bilayers	39
4.3.1	Two-dimensional moiré band folding	40
4.3.2	Exciton mixing through phenomenological moiré potentials and inter-layer coupling	42
4.3.3	Limiting cases of the effective model	44
4.4	Charge doping in periodic moiré lattices	47
4.5	Interaction of excitons and periodic charge lattices	52
5	Moiré physics in MoSe₂/WS₂ heterostructures	55
5.1	Sample overview and initial characterization	56
5.2	Field-induced hybridization of moiré excitons and the role of band alignment .	64
5.2.1	Modeling of moiré excitons	64
5.2.2	Interlayer excitons in modulation spectroscopy	65
5.2.3	Real space distribution of moiré exciton states	66
5.3	Charge doping and the role of the moiré potential	68
5.3.1	Exciton localization in the moiré cell and intralayer sensing	68
5.3.2	From moiré to Hubbard: discretization of the density of states by on-site Coulomb repulsion	72
5.4	Magneto-optical signatures of bilayer spin-susceptibility	75
6	Summary and outlook	81
	Appendix A Software development in Python	85
	Bibliography	91
	Acknowledgments	107
	List of publications	109
	List of abbreviations	111

Introduction

No exaggeration could possibly overstate the surge in scientific progress throughout the last century. A hundred years ago, the Nobel committee recognized the dawn of quantum physics and awarded the 1921 Nobel prize to Albert Einstein for the discovery of the photoelectric effect [1]. Today, state of the art technologies harvest our understanding of materials science and quantum mechanics to routinely control light on the single-photon level [2, 3]. The extent of physical discoveries that led to fundamental upheavals of our societies is difficult to comprehend and can hardly be covered in a single work [4–6]. A big number of the 20th century's most disruptive innovations, however, manifest themselves in the advent of the modern semiconductor industry which came to permeate through almost every aspect of our modern life and became fundamental to the emerging information age.

The main characteristic of a semiconducting system is as simple as it is far-reaching and boils down to an energetic gap in its fundamental excitations. Through the process of doping, it is possible to control both the prevalence and the coupling of such excitations to other systems, allowing to exploit them in a range of electronic and photonic applications. As a materials class, the family of semiconductors includes some of the most versatile compounds, with use cases spanning from computing and memory storage through energy production and power electronics to logic, light emission and sensing [4].

At the present day, conventional electronics is almost entirely dominated by elemental silicon which is one of the most abundant materials in the earth's crust. In the same time, innovations in photonic technologies and the emergence of new computing paradigms [7, 8] drive the demand for alternative materials that could overcome the limitations of traditional silicon which is thwarted by its indirect band gap. While some classical semiconductors such as germanium or gallium arsenide already proved invaluable for specific edge applications, the recent decades have also seen a growing research interest in the role of dimensionality. The effects of quantum confinement and size quantization emerged as vital parameters for exploiting light-matter coupling in low-dimensional semiconductor structures, with the example of zero-dimensional quantum dots having already entered their phase of commercialization with the introduction of the QLED screen technology [9]. In the two-dimensional corner, on the other hand, the

family of the atomically thin *transition metal dichalcogenides* (TMDs) [10] has recently emerged as a very promising candidate platform for both optoelectronic applications and fundamental quantum research.

One of the most important properties of TMDs lies in their direct band gap in the visible spectral range. In their monolayer limit, TMDs are characterized by extraordinarily large effective masses of charge carriers and very pronounced light-matter interaction, which is dominated by tightly bound electron-hole pairs known as excitons. Multilayer TMD structures, on the other side, have attracted ever increasing attention in the framework of van der Waals engineering which promoted them as valuable model systems for two-dimensional condensed matter physics [11]. In particular the so-called moiré effect – a geometric interference pattern that generally appears in slightly mismatched periodic structures – has enabled the discovery of numerous unprecedented phenomena mediated by strong Coulomb interactions. The behavior of excitons in the presence of such moiré effects, as well as their interaction with free charge carriers, provides a non-invasive spectroscopic probe of moiré induced phenomena and established TMD bilayers as a uniquely fertile ground for basic research in solid-state physics.

With the formidable abundance of exotic phases observed in most TMD heterostructures, the scientific literature has long focused on the commonly studied MoSe₂/WSe₂ [12] and WS₂/WSe₂ [13] which are characterized by large conduction and valence band offsets of hundreds of meV. The less prominent combination MoSe₂/WS₂, on the other hand, exhibits resonantly aligned conduction bands [14] and has only recently begun to gain attention in the framework of correlated states [15, 16]. The resonance condition between MoSe₂ and WS₂ implies significant hybridization effects and electrostatic tunability of the fundamental band alignment between the two monolayers, rendering MoSe₂/WS₂ both more complex yet interesting at the same time. The goal of this thesis was to explore the effects of the moiré pattern in this specific heterostructure and to establish fundamental understanding of its low-energy excitonic physics.

The results of this work are mainly based on optical spectroscopy. To introduce the notions necessary to understand and contextualize the experimental data, we proceed after the introductory Chapter 1 by giving a general overview of the optoelectronics of TMDs in Chapter 2. We introduce the family of TMDs in the context of two-dimensional van der Waals materials and establish the properties of excitons and their behavior in the presence of externally applied fields or free charge carriers.

In Chapter 3, we present the main experimental methodology employed in this work. To study the low-energy physics of excitons, it is important to establish control over a range of experimentally tunable parameters such as temperature, charge density, electric or magnetic fields, spatial sample positions or the optical excitation. We provide a self-contained discussion of how to perform cryogenic spectroscopy on layered semiconductor structures and explain

the fundamentals of state of the art technologies such as sub-Kelvin cooling by dilution refrigerators.

Chapter 4 deals with the theoretical models that have been either adapted or developed for the evaluation of the experimental results of this work. In particular, we present an extensive discussion of the moiré effect in TMD heterobilayers and explain both its geometric origin as well as its implications on band folding and exciton mixing. Moreover, we provide a clarified discussion of electrostatics in planar semiconductor structures that is relevant to modeling of the excitonic behavior in the presence of periodic charge carrier lattices in moiré structures.

Subsequently, we present the main experimental results of this work together with their theoretical discussion in Chapter 5. In particular, we discuss the exciton physics in angle-aligned $\text{MoSe}_2/\text{WS}_2$ heterostructures and provide a comprehensive description of the effects of the moiré pattern. By studying the dispersion of the moiré excitons with perpendicular electric fields, we establish the presence of a complex interplay of resonant interlayer tunneling with non-resonant moiré potentials that leads to very distinctive electrostatics of the studied samples. As a result, we find evidence for a peculiar layer-by-layer charging behavior that enables the formation of bilayer lattices of electrons correlated across two layers. We perform measurements of doping-dependent spin susceptibility that indicate antiferromagnetic exchange interactions and suggest the presence of electrostatically tunable Ruderman-Kittel-Kasuya-Yosida magnetism, establishing $\text{MoSe}_2/\text{WS}_2$ as a novel platform for studies of bilayer Hubbard model physics with exotic magnetic phases on frustrated lattices.

Finally, we give a summary of this thesis in Chapter 6 and provide an outlook for future research directions related to the $\text{MoSe}_2/\text{WS}_2$ system. Notably, the scope of this work is naturally limited to questions that can be addressed with methods of optical spectroscopy and – apart from the collaboration on many-body theory with Fabian Grusdt and Annabelle Bohrdt – with phenomenological low-energy models. For this reason, there is a range of questions that can be addressed by dedicated *ab initio* theoretical studies as well as by complementary experimental probes such as transport measurements or scanning tunneling microscopy, providing opportunities for future collaborations in the field. Importantly, we wish to emphasize that this thesis itself is the result of collaborative work and would not be possible without the contribution of several people. The spectroscopic experiments have notably been carried out together with Johannes Scherzer and Subhradeep Misra, whereas the theoretical models have been developed together with Anvar S. Baimuratov and Henning Schlömer. The results of this work have been published, partly verbatim, in Refs. [17, 18].

Fundamentals of transition metal dichalcogenides

We take a point of view in the spirit of Wolfgang Pauli's famous quote "*God made the bulk; the surface was created by the devil*" and emphasize the fundamental difference between the surface of a given material and its bulk. A surface – or more generally an interface between two materials – can be characterized by the discontinuities in the dielectric environment and the electronic dispersion that impose distinctive governing principles upon the mobile charge carriers. The surface to volume ratio of a given sample has therefore far-reaching physical consequences that can be controlled by manipulating the thickness of a material layer. Historically, this idea has been demonstrated in classical semiconductor heterostructures where well-defined interfaces enabled the confinement of charge carriers to two dimensions. Some of the most prominent highlights of the 20th century physics, such as the discovery of the quantum hall effect [19] or the development of quantum well lasers [20], have only been made possible by meticulous control of interfaces in molecular beam epitaxy.

Layered van der Waals (vdW) materials provide an alternative route to quantum confinement and present a natural limit in terms of how thin a device can be made. Loosely speaking, a vdW material is defined by strong planar covalent bonds and weak vdW forces between individual atomic planes. By going to the atomically flat monolayer limit of such a layered compound, the notion of bulk loses its applicability altogether – the material *becomes* the surface. In recent years, vdW materials emerged as an increasingly important platform for fundamental condensed matter research, and the goal of this Chapter is to give a high-level introduction to the physics of these materials. In particular, we will focus on a certain class within them called *transition metal dichalcogenides* (TMDs). In presenting TMDs, we will motivate the enthusiasm of the scientific community for this class of materials and establish some important notions of semiconductor optoelectronics that will be used throughout this work.

We start by giving a general overview of the field of vdW materials in section 2.1 and introduce some important compounds that are used extensively in this thesis. Motivated by the common honeycomb geometry in these materials, we subsequently introduce some basic results on the Brillouin zone and the band structure in hexagonal two-dimensional (2D) crystals

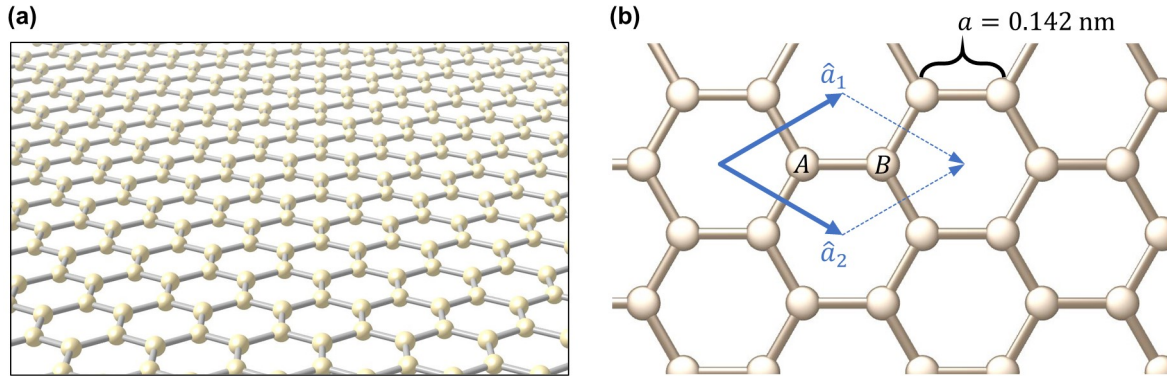


Figure 2.1: Basic crystal structure of monolayer graphene. (a) Three-dimensional view on the hexagonal graphene lattice. (b) Top view illustrating the lattice geometry and the graphene unit cell spanned by the vectors \hat{a}_1 and \hat{a}_2 . The unit cell contains two carbon atoms denoted by A and B in the figure. This and other crystal structures in this work have been visualized by the VESTA software package [21].

in section 2.2 and characterize the low-energy bands that dominate the optoelectronic physics in TMDs. In section 2.3, we build upon the established band structure and familiarize ourselves with the light-matter coupling in TMDs. The latter is dominated by tightly bound electron-hole pairs known as excitons, and we dedicate subsections 2.3.1-2.3.3 to explain the basic physics of these quasi-particles as well as their response to experimentally tunable parameters such as temperature, charge density, or electric and magnetic fields. Finally, we give a brief summary of this Chapter with an emphasis on TMD physics in section 2.4.

2.1 | Overview of two-dimensional van der Waals materials

If the family of vdW materials had a mother, it would undoubtedly be graphene. It was the first monoatomic 2D crystal that retained a persistent and continuous interest of the physics community [22–27]. As illustrated schematically in Fig. 2.1, graphene is a monolayer of carbon atoms arranged in a hexagonal honeycomb lattice that occurs naturally in the form of planar atomic sheets in graphite [28]. Whereas graphite itself is an ordinary material that can be found in pencils or car electrodes, a pioneering study by the later Nobel laureates Andre Geim and Konstantin Novoselov showed that monolayer graphene presents remarkable electronic properties with an unprecedented electron mobility [29], and triggered a natural gold rush in research on two-dimensional materials in general.

The appeal of graphene arises from the simultaneous simplicity of its physics and the di-

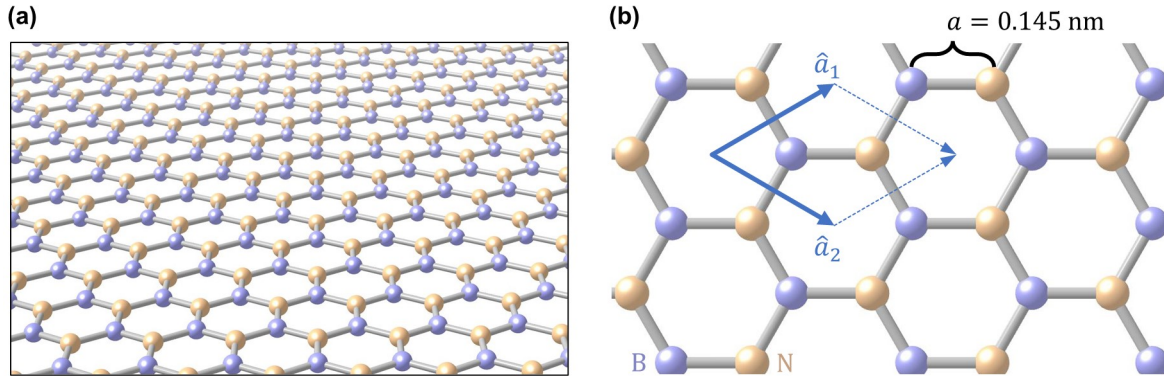


Figure 2.2: Basic crystal structure of monolayer hBN. (a) Three-dimensional view on the hexagonal hBN lattice isomorphic to the graphene structure. (b) Top view illustrating the lattice geometry and the hBN unit cell spanned by the vectors \hat{a}_1 and \hat{a}_2 . Qualitatively, the only difference between graphene and hBN is in the different atoms at the A- and B-sublattices labeled in Fig. 2.1.

versity of the phenomena that it can host. While early studies focused more on characterization and exploration of potential applications in monolayers, the discovery of a range of exotic phases in mono- and bilayer graphene revealed its increasing significance for fundamental research [30–36]. Soon after, it became clear that it can also be integrated with other two-dimensional crystals into vertically stacked heterostructures [37–43]. The combination of different materials into artificial vdW heterostacks provided researchers the freedom to deliberately design previously elusive structures in a process termed "van der Waals lego" [40], and started a new era in condensed matter physics while promoting the quest for new vdW materials as prospective building blocks [44].

Today, the family of 2D materials includes hundreds of compounds and extends over the whole range of modern solid-state physics including metals [45], semimetals [27], superconductors [46, 47], semiconductors [10, 48, 49], insulators [50], magnetic crystals [51, 52], and topological materials [53, 54]. It would be out of the scope of this work to give a comprehensive overview of all these compounds, and we refer the reader to some of the several excellent reviews in the literature [10, 43, 44, 49, 52, 55]. Here, we focus on the materials that became increasingly important for optoelectronics based on vdW materials and that constitute the basis for this work, namely the insulating hexagonal Boron Nitride (hBN) and the semiconducting Transition Metal Dichalcogenides (TMDs).

Continuing with the family analogy, hexagonal Boron Nitride [56] is certainly graphene's closest cousin that has been used industrially for decades in its bulk form [57] and is sometimes also called *white graphene*. The two materials share the same hexagonal honeycomb structure that can be understood as two staggered triangular sublattices A and B (see Fig. 2.1b). In

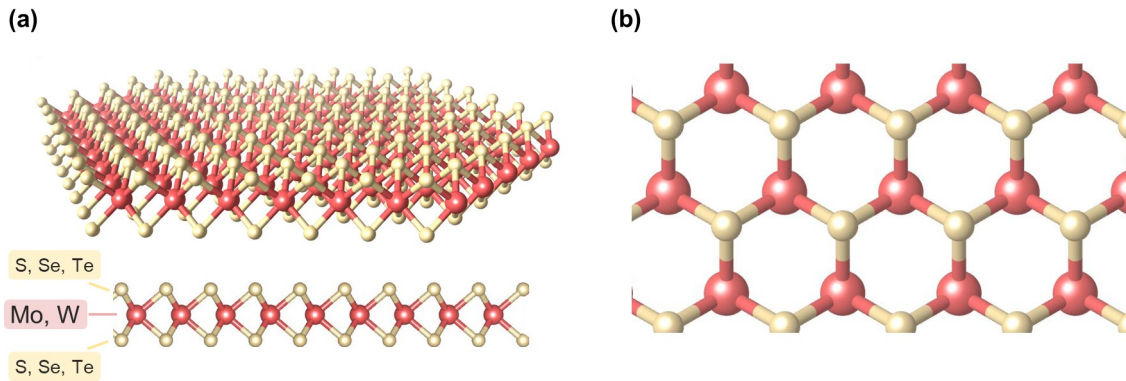


Figure 2.3: Basic crystal structure of monolayer TMDs. (a) Three-dimensional view on the hexagonal MX_2 lattice (top) and side view illustrating the bonding between the metal ($\text{M} = \text{Mo}$ or W , red) and chalcogen ($\text{X} = \text{S}$, Se or Te , beige) atoms. (b) Top view illustrating the lattice geometry reminiscent of the graphene and hBN lattices. Here, each unit cell contains three atoms (one metal and two chalcogenes).

graphene, both of these sublattices are occupied by carbon atoms, whereas in hBN they have a lower symmetry and consist of boron and nitrogen atoms as shown in Fig. 2.2. The difference in the orbital energies of these two sublattices introduces a band gap of around 6 eV that makes hBN insulating [55]. The magnitude of its band gap renders hBN interesting for both deep-UV photonic applications [58–60] as well as an inert dielectric for vdW heterostructures, where it is known to reduce extrinsic disorder [61] and drastically improve electronic [50] and optical properties [62, 63] of other 2D materials. In this work, we rely heavily on the latter property and use hBN as a dielectric in the field-effect heterostacks presented in Chapter 3.

Finally, Transition Metal Dichalcogenides present the next step in terms of complexity for elementary 2D crystals. They share the general formula MX_2 where M stands for a transition metal - most commonly molybdenum (Mo) or tungsten (W) - and X for a group VI chalcogen atom (most commonly S or Se , sometimes Te) [10, 48, 49, 64]. While they can occur in different structural phases with distinct crystal symmetries, the modern literature focuses mostly on the semiconducting trigonal prismatic 2H phase that is characterized by its hexagonal honeycomb lattice reminiscent of graphene and hBN. Just as in the case of hBN, the unit cell of TMDs can be split in two inequivalent sublattices with the first one covering the metal atoms and the second the chalcogens. Contrary to the atomically flat hBN layer, however, TMDs are structured in three atomic layers with the metal atoms sandwiched between two layers of chalcogens as shown in Fig. 2.3, implying that the second sublattice contains two atoms per unit cell itself.

Similar to graphene and hBN, bulk TMDs have been known and studied for decades [65]. In the 2D limit, first monolayer flakes of TMDs were exfoliated as early as graphene [66], yet their presence has long been obscured by the numerous studies on the latter. The first TMD

monolayer to emerge from oblivion was MoS₂ [67, 68] after the vain efforts to open a band gap in graphene [48]. Indeed, the commonly studied TMDs are characterized by a band gap in the visible spectral range that is indirect in multilayered structures but becomes direct in the monolayer limit [67]. For this reason, the first studies in the early 2010s mainly viewed TMDs as a form of 'gapped graphene' and focused on their (opto-) electronic applications [69–72]. Combined experimental and theoretical progress, however, revealed that TMDs also possess several distinctive properties such as large effective masses for both electrons and holes [64, 73–75], huge spin-orbit splittings [64, 75–77], or valley-selective chiral optical selection rules [64, 75, 76, 78–81]. Furthermore, electrostatic control of the charge carrier density inside TMDs [82] enabled studies of charged excitonic complexes and opened the way to investigations of electronic many-body states probed in optical spectroscopy.

The range of their unique characteristics, together with the flexibility in designing novel vdW heterostructures from individual 2D crystals, established TMDs as a very fertile ground in fundamental condensed matter research [11, 83–85]. Especially the geometric moiré effect [86], arising when stacking two monolayers with small lattice mismatch or rotational misalignment, plays a very important role in this development by introducing a periodic long-range moiré potential for charge carriers and providing a scaffold for ordered electronic states [11, 17, 87, 88]. The periodicity of the moiré potential depends sensitively on the rotation angle between the layers and allows to deliberately engineer the physical properties of van der Waals structures, enabling first-ever demonstrations of such fascinating phenomena as Wigner electron crystallization [89] or kinetic magnetism in frustrated spin-lattices [16].

2.2 | Basic band structure considerations: from graphene to layered semiconductors

All of TMDs, graphene, and hBN share the same hexagonal honeycomb lattice geometry that corresponds to a triangular Bravais lattice spanned by the vectors

$$\hat{a}_1 = \frac{3}{2}a \begin{pmatrix} 1 \\ 1/\sqrt{3} \end{pmatrix}, \quad \hat{a}_2 = \frac{3}{2}a \begin{pmatrix} 1 \\ -1/\sqrt{3} \end{pmatrix}. \quad (2.1)$$

These vectors define a triangular reciprocal lattice that is spanned by the vectors

$$\hat{g}_1 = \frac{2\pi}{3a} \begin{pmatrix} 1 \\ \sqrt{3} \end{pmatrix}, \quad \hat{g}_2 = \frac{2\pi}{3a} \begin{pmatrix} 1 \\ -\sqrt{3} \end{pmatrix}, \quad (2.2)$$

implying a hexagonal first Brillouin zone as illustrated in the left panel of Fig. 2.4.

To motivate the low-energy band structure of TMDs, we first proceed by familiarizing ourselves with this reciprocal space geometry and recall the basic tight-binding description in

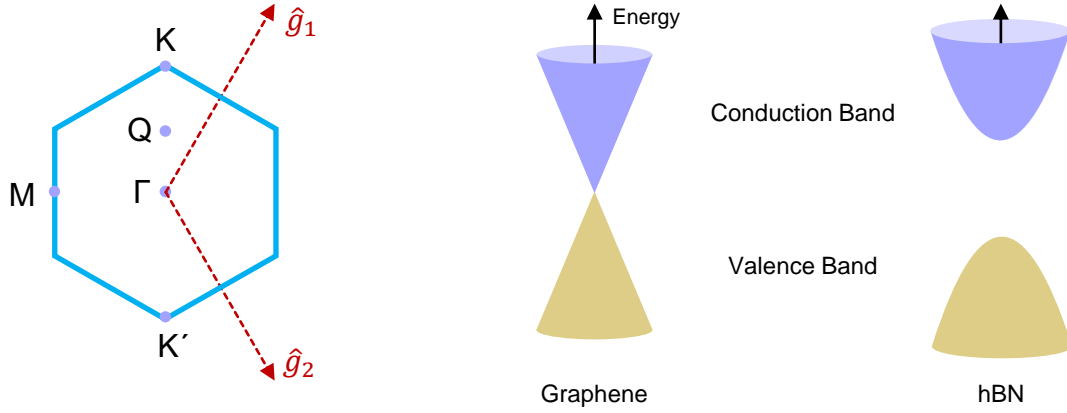


Figure 2.4: *Left panel*: first Brillouin zone of the two-dimensional triangular Bravais lattice with the high-symmetry points Γ , M , Q , K and $K' = -K$. *Center panel*: band dispersion of monolayer graphene at the high-symmetry momenta $\pm K$ reminiscent of relativistic massless fermions. *Right panel*: band dispersion of monolayer hBN at the high-symmetry momenta $\pm K$, corresponding to massive Dirac fermions.

monolayer graphene and hBN. We assume a free orbital per atom and nearest-neighbor hopping. In graphene, for example, this would correspond to an on-site orbital energy of that we set to zero, $\epsilon_0 = 0$, as well as of a hopping Hamiltonian of the form

$$H = -t \sum_R |R\rangle_B \langle R|_A + |R - \hat{a}_1\rangle_B \langle R|_A + |R - \hat{a}_2\rangle_B \langle R|_A + h.c., \quad (2.3)$$

where $|R\rangle_{A/B}$ corresponds to a free orbital at the A (B) carbon atom in the lattice site R (see Fig. 2.1) and t is the nearest-neighbor hopping amplitude. Introducing the Bloch functions,

$$|k\rangle_{A/B} = \frac{1}{\sqrt{N}} \sum_R e^{ikR} |R\rangle_{A/B}, \quad (2.4)$$

results in the familiar tight-binding Hamiltonian diagonal in k , but not yet in the A/B sublattice,

$$H_k = \begin{pmatrix} 0 & -t\gamma^* \\ -t\gamma & 0 \end{pmatrix}. \quad (2.5)$$

Here, the geometric phase factor $\gamma = 1 + \exp ik\hat{a}_1 + \exp ik\hat{a}_2$ encodes the lattice geometry and by this defines the basic properties of the electronic band structure. Most notably, it vanishes at the two inequivalent $\pm K = (0, \pm \frac{4\pi}{3\sqrt{3}a})^T$ valleys, i.e. $\gamma_{\pm K} = 0$. To study the low-energy physics at these high-symmetry points, one usually expands γ to first order in $q = k - K$, yielding the low-energy approximation known as the massless Dirac Hamiltonian:

$$H_{\pm K} = \begin{pmatrix} 0 & \frac{3at}{2}(\pm q_y - iq_x) \\ \frac{3at}{2}(\pm q_y + iq_x) & 0 \end{pmatrix}. \quad (2.6)$$

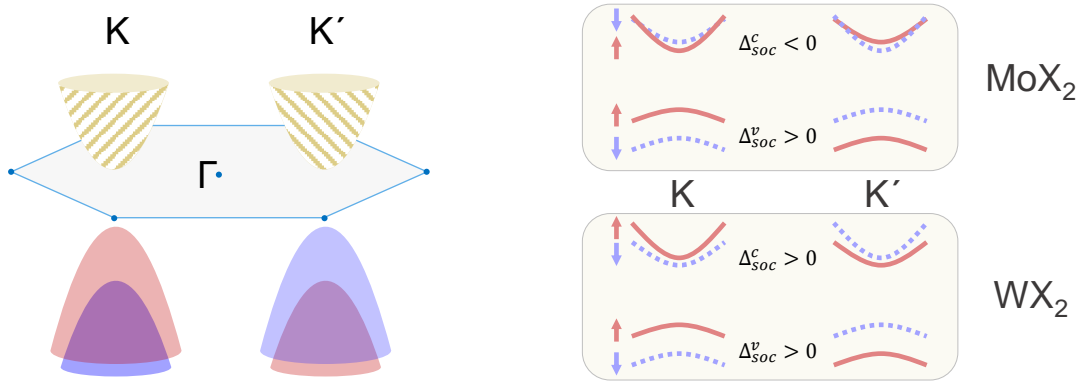


Figure 2.5: *Left panel*: parabolic band dispersion at the high-symmetry $\pm K$ valleys with the pronounced spin-orbit coupling (SOC) at the valence bands. *Right panel*: low-energy electron and hole dispersions for Mo and W based TMDs at the $\pm K$ valleys.

This Hamiltonian implies two touching bands with linear dispersion as illustrated by the Dirac cones in the central panel of Fig. 2.4, $\lambda_{\pm} = \pm 3at |q|/2$. In the case of hBN, one simply introduces an asymmetry between the orbital energies of boron and nitrogen atoms. By defining their energy difference as 2Δ and setting the Fermi energy exactly in the middle between the two, the low-energy Hamiltonian of hBN becomes [90]

$$H_{\pm K} = \begin{pmatrix} \Delta & \frac{3at}{2}(\pm q_y - iq_x) \\ \frac{3at}{2}(\pm q_y + iq_x) & -\Delta \end{pmatrix}. \quad (2.7)$$

As a result, the fundamental excitations obtain an effective mass and the two bands present the parabolic dispersion $\lambda_{\pm} = \pm \sqrt{9a^2t^2|q|^2/4 + \Delta^2}$ as illustrated in the right panel of Fig. 2.4.

In monolayer TMDs, the similarity to the lattice geometry of hBN implies the same qualitative low-energy dispersion at the $\pm K$ valleys, i.e. in first approximation one also deals with parabolic bands with a direct band gap. The increased crystallographic complexity (Fig. 2.3), however, as well as the large number of available orbitals in the heavy metal atoms, render naive tight-binding models unsuitable to describe the TMD's electronic structure. For this reason, early studies focused on *ab initio* methods [67, 73, 91–96] that allowed to reveal such distinctive properties as the very pronounced spin-orbit splitting due to the heavy metal atoms [91] or the locking of the spin and valley degrees of freedoms due to the broken inversion symmetry in the trilayer lattice structure [76].

The insights obtained from first-principle calculations imply that the low-energy bands at the $\pm K$ valleys of TMDs are dominated by the d_{z^2} , d_{xy} and $d_{x^2-y^2}$ orbitals of the metal atoms, whereas the chalcogen orbitals barely play a role [91, 97]. This enables *à posteriori* modeling of the band-edges through taylored tight-binding approaches [77, 97, 98] or $k \cdot p$ Hamiltonians [73]. In particular, in a first approximation $k \cdot p$ theory yields the easiest Hamiltonian that

can capture the low-energy physics in TMDs, and it turns out to be nothing more than the gapped Dirac Hamiltonian (2.7) extended by spin-orbit coupling (SOC) [73, 76, 97]:

$$H_{\pm K} = \begin{pmatrix} \Delta & \frac{3at}{2}(\pm q_y - iq_x) \\ \frac{3at}{2}(\pm q_y + iq_x) & -\Delta \end{pmatrix} \pm \begin{pmatrix} \Delta_{soc}^c & 0 \\ 0 & \Delta_{soc}^v \end{pmatrix} \otimes \hat{s}_z. \quad (2.8)$$

Notably, time-reversal symmetry implies opposite SOC for the two valleys [73], whereas the difference of the metal atoms results in opposite sign of Δ_{soc}^c between Mo and W based TMDs as indicated in Fig. 2.5. It is important to emphasize that the SOC in the valence bands is one order of magnitude stronger than in the conduction bands, reaching hundreds and tens of meV, respectively. Moreover, all bands exhibit relatively large effective masses on the order of $0.5 m_e$ [73]. Together with the pronounced quantum confinement inherent to 2D materials, these properties tend to dominate the light-matter interaction in TMD monolayers, and we will continue exploring their implications for optoelectronics in the next section.

2.3 | Optoelectronics in transition metal dichalcogenide monolayers

When a light photon is absorbed by a semiconducting material, it usually involves a direct electronic transition and results in an electron promoted to the conduction and a hole remaining in the valence band [99]. Both of these (quasi-) particles carry such elementary properties as an effective mass or charge and are generally subject to non-vanishing Coulomb interactions. The charges of the electron and the hole being opposite results in an attractive interaction and enables the formation of correlated electron-hole pairs known as *excitons* [100]. The goal of this section is to introduce the physics of excitons in monolayer TMDs and to establish them as important optical reporters of electronic states.

2.3.1 | Wannier-Mott excitons and the role of dielectric screening

Historically, the notion of the exciton is usually attributed to Frenkel [101] who introduced the type of tightly localized excitons known under his name. While much of related work remains buried in the Soviet literature, modern semiconductor research usually focuses on another type of excitons that were first investigated by Wannier and Mott [102, 103] and are characterized by a larger spatial extent of the correlated electron-hole pair. As a result, their behavior becomes qualitatively analogous to the one of hydrogen with corrected masses and dielectric screening, and most of excitonic complexes in TMDs are studied from the perspective of such *Wannier-Mott excitons*.

In TMDs, excitons typically present mean-square radii on the order of 1 nm [75, 96] and cover several elementary unit cells as illustrated in Fig. 2.6a. This makes the hydrogen model applicable to describe excitons in bulk TMDs, and because of the large effective masses the excitonic binding energies reach scales of 50 meV already in the bulk [65, 104]. In the two-dimensional limit, reduced dielectric screening renders both the 3D and 2D hydrogen models inaccurate [105]. The discontinuity in the dielectric environment, schematically depicted in Fig. 2.6c, implies a distinct effective interaction that is described by the Rytova-Keldysh potential [75, 106, 107]. As a result, the exciton binding energies in monolayer TMDs attain values on the order of hundreds of meV [75, 92, 94, 96, 107], leading to pronounced absorption peaks deep below the free-particle band edge even at ambient temperatures. At cryogenic temperatures, the reduction of thermal broadening and the resulting small line widths enable the observation of excited excitonic states for a range of principal quantum numbers $n = 1, \dots, 5$ as illustrated in Fig. 2.6d [107].

Finally, it is important to emphasize that in the absence of band mixing, the light-matter interaction of the excitons is affected by the typical conservation laws of energy ($E_{ph} = E_X$), momentum ($k_{ph}^{\parallel} = k_X^{\parallel}$) and spin ($\Delta s = 0$). For this reason, even if electrons and holes of different spins and momenta can be bound together, it is imperative to distinguish between so-called *optically bright* (satisfying the conservation laws) and *optically dark* (not satisfying the conservation laws) excitons as illustrated in Fig. 2.6b. Optically bright excitons are those that can couple to light without the involvement of further quasi-particles such as phonons and are characterized

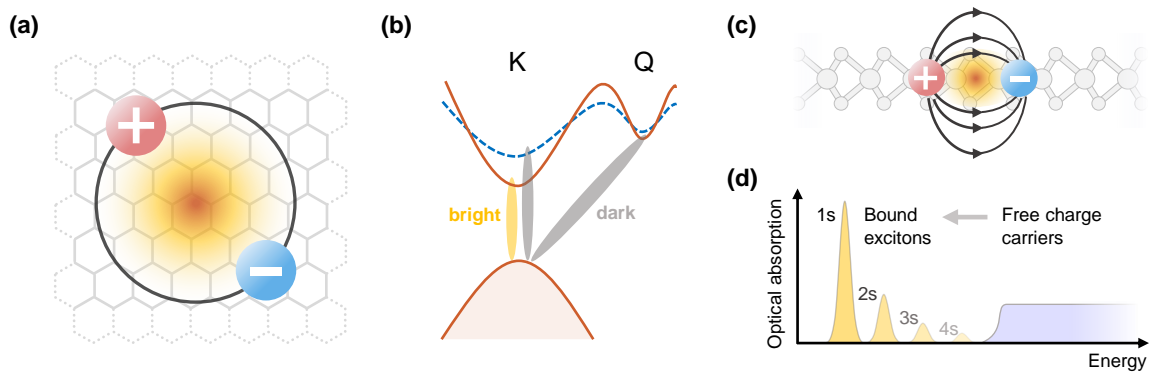


Figure 2.6: **Overview of excitons in TMDs.** (a) The spatial extent of the bound electron-hole pair covers several unit cells, justifying the Wannier-Mott picture. (b) An exciton can consist of electrons and holes in different valleys, while spin and momentum conservation laws imply that only direct transitions between bands of the same spin are optically bright. (c) Side view on an exciton in a monolayer TMD. The reduced dielectric screening outside of the monolayer implies sizable changes to the exciton binding energies that can reach hundreds of meV. (d) Schematics of the optical absorption spectra featuring a series of excitonic states below the free particle band edge. This Figure builds upon Ref. [75].

by short radiative lifetimes on the order of few ps [108]. Momentum conservation demands that bright excitons are necessarily intravalley complexes, and the large spin-orbit coupling in TMDs implies that there generally are two bright exciton species A and B involving the upper and lower valence bands in both $\pm K$ valleys, respectively [109].

2.3.2 | Charged excitonic complexes

When free charge carriers are present in a semiconductor – either controlled electrostatically or present due to (un-) intentional chemical doping – the excitons will generally form charged complexes that are characterized by specific resonance energies and distinct optical signatures [110]. In MoSe_2 , for example, a K -valley exciton can form a bound state with a K' -valley conduction electron that will manifest itself by a distinct peak in photoluminescence (PL) as illustrated in Fig. 2.7b. The behavior and the properties of these new resonances critically depend on both the charge carrier and the exciton densities [75]. High-exciton densities typically lead to a range of exciton-exciton interactions and result, for example, in the formation of biexcitons [75]. Low exciton densities, on the contrary, correspond to the case of isolated excitons when the exciton Bohr radius is significantly smaller than the inter-exciton distance. In the following discussion, we limit ourselves to the case of low exciton densities and consider the interaction of isolated excitons with a Fermi sea of electrons or holes.

In the regime of intermediate to high charge carrier densities, it is important to emphasize that the exciton represents a composite boson in the presence of a dense reservoir of fermions. For this reason, charged excitons have commonly been addressed in the framework of the so-called *Fermi-polaron* model [110–114]. In this approach, the exciton is considered as an impurity dressed by the mobile charge carriers as illustrated on the left of Fig. 2.7a. A full description of the Fermi-polaron in a many-body framework predicts the emergence of two distinct resonance branches, the so-called repulsive and attractive polarons. In particular, the repulsive polaron evolves continuously from the charge-neutral bare exciton, whereas the attractive polaron is characterized by a non-vanishing binding energy and manifests itself by a distinct absorption peak on the lower energy side of the bare exciton.

For low to intermediate charge carrier densities – generally either comparable or lower than the exciton density – the inter-particle distance becomes large enough such that scattering events only involve isolated excitons and charge carriers. In this regime, the many-body polaron states reduce to correlated three-particle states known as trions [82, 105, 115–118]. In this picture, the repulsive polaron corresponds to the neutral exciton in the presence of moderate Pauli blocking, whereas the attractive polaron can be understood as the exciton capturing a mobile electron (hole) to form a negative (positive) three-particle complex reminiscent of the Hydrogen ion, see Fig. 2.7a.

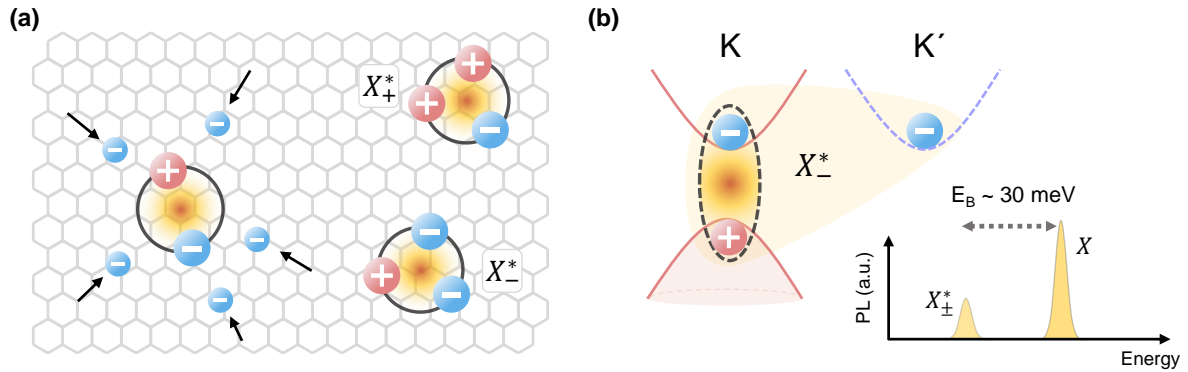


Figure 2.7: **Schematics of charged exciton complexes in MoSe₂.** (a) In the presence of free charge carriers, excitons can form charged correlated many-body states. For high carrier densities, Fermi polarons consisting of excitons dressed with the carriers can form (left), whereas for low densities, three-particle complexes like positive (X_+^*) or negative (X_-^*) trions (right) appear. (b) Similar to excitons, trions can involve charge carriers from different valleys and bands. In Mo-based TMDs, optical selection rules and exchange interactions imply that only K (K') excitons that are bound to a charge from the K' (K) valley are optically bright. In the case of MoSe₂, the resulting binding energy is around 30 meV and leads to a bright emission peak on the lower-energy side of the neutral exciton in photoluminescence (PL).

We emphasize that both approaches largely agree in their predictions on the binding energy or the oscillator strength of the charged exciton states [110], leading to a continuing debate on the validity of the two models. In this work, we will mainly be dealing with low or intermediate charge carrier densities, and therefore we will employ the trion picture and think of charged three-particle complexes in the spirit of tightly bound excitonic ions.

2.3.3 | Response to external fields: excitonic valley Zeeman and Stark effects

Finally, we point out that the excitonic resonances in TMDs are strongly influenced by the presence of magnetic and electric fields. The range of the different bright and dark excitonic species, as well as the details of the internal exciton structure, result in a plethora of intricate phenomena that can critically modify the optical signal of a TMD device [75, 119–123]. The most pronounced effects are undoubtedly related to the influence of *out-of-plane* fields, and in the following, we present the linear excitonic behavior in response to such externally applied magnetic and electric fields.

First, in order to understand the evolution of excitons in the presence of magnetic fields, we outline some of the symmetries that govern the light-matter interaction in TMDs. As in the

case of graphene and hBN, monolayer TMDs are subject to a range of crystallographic symmetry relations that determine the band structure and the optical selection rules. The three-fold rotation and time-reversal symmetries, for example, imply that the bands at the $\pm K$ valleys present the same energies but opposite spin-splitting as illustrated in Fig. 2.5. Moreover, additionally to the spin, also the angular momentum of the electronic states is opposite due to the time-reversal symmetry. The breaking of inversion symmetry, on the other side, introduces the valley-dependent off-diagonal terms in the Hamiltonian (2.8) that imply chiral optical selection rules with opposite helicity at the K and K' valleys [76, 124]. This results in pronounced valley dichroism that can be probed in circularly polarized reflection or photoluminescence spectroscopy [78, 79, 125–131].

The discussed contrast between the K and K' valleys leads to distinct evolution of the electronic states in the presence of an externally applied magnetic field B . In linear response theory, an electron or hole interacts with the magnetic field through its spin and angular momentum. An electron (hole) with momentum k changes its potential energy by a Zeeman shift $V_Z(k)$ proportional to B [132, 133],

$$V_Z(k) = \mu_B B [g_0 s + L(k)] , \quad (2.9)$$

where $\mu_B = 57.9 \mu\text{eV/T}$ is the Bohr magneton, $g_0 \simeq 2$ the free electron Landé factor, $s = \pm 1/2$ the (out-of-plane) spin of a given electronic state and $L(k)$ its angular momentum. The opposite sign of s and L in the two valleys (i.e. $L(K) = -L(-K)$ from time-reversal symmetry) implies that their Zeeman shift is also opposite as illustrated in Fig. 2.8a. As a result, the excitonic resonance probed in either σ^+ or σ^- polarized light will present an energy shift itself, with the

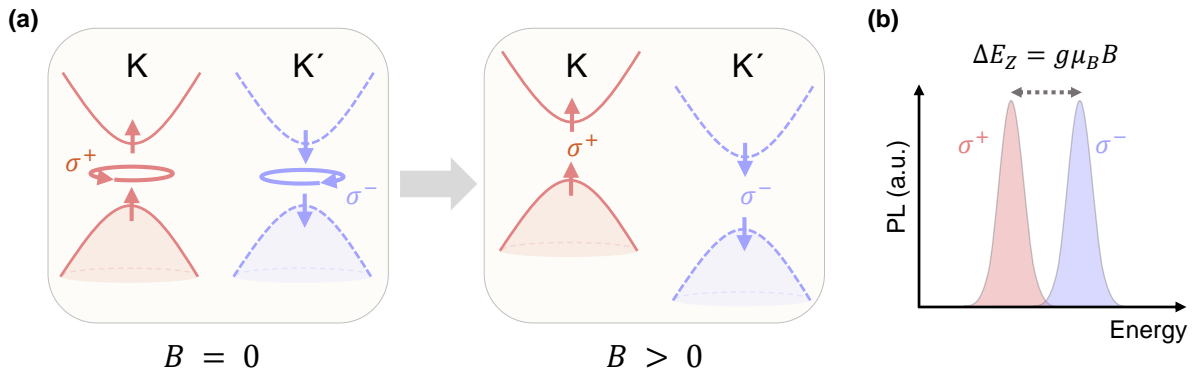


Figure 2.8: **Valley-Zeeman effect in MoSe₂**. (a) Due to their opposite spins and angular momenta, the electronic states in the $\pm K$ valleys present opposite energy shifts in the presence of an out-of-plane magnetic field B . (b) The chiral optical selection rules illustrated in (a) imply that the photoluminescence signal (PL) in σ^\pm detection is entirely dominated by the excitons in the $\pm K$ valley, leading to different measured resonance energies in the presence of a magnetic field.

valley Zeeman energy splitting given by

$$\Delta E_Z = E(\sigma^+) - E(\sigma^-) \equiv g\mu_B B. \quad (2.10)$$

In the last equation, we defined the *exciton Landé factor* $g = \Delta E_Z / (\mu_B B)$ as a dimensionless number characterizing the behavior of an exciton under out-of-plane magnetic fields. It measures the exciton dispersion as a function of B , and as such it can act both as a reporter on the electronic subbands involved in the exciton as well as on the local magnetization in the exciton's neighborhood.

The presence of electric fields is different in the way that contrary to a magnetic field, an electric field can always be associated with a scalar electric potential ϕ , i.e. $E = -\nabla\phi$. For out-of-plane fields, this means that the electric potential is constant throughout a monolayer plane, implying that intralayer excitons are not affected by such perpendicular electric fields in first order. The situation changes, however, when vertical vdW heterostructures consisting of several monolayers of TMDs are considered. In that case, the interlayer degree of freedom allows for so-called *interlayer excitons* consisting of an electron and a hole residing in different layers. Changing the out-of-plane potential difference effectively amounts to changing the relative energetic position of the electronic states in the different layers. Therefore, similar to the energy shift by the Zeeman effect discussed above, such electrostatic shifts of the electron and hole band energies result in linear Stark shifts of the interlayer excitons [134, 135].

2.4 | Summary

In summary, the family of van der Waals materials covers layered, two-dimensional planar crystals and includes a wide range of different phenomenologies, ranging from insulators [50] through semiconductors [10, 48, 49] to metals [45], magnets [51, 52], and superconductors [46, 47]. In this class, atomically thin transition metal dichalcogenides (TMDs) are direct band gap semiconductors and present a very fertile ground for both optoelectronic applications [49, 74] and fundamental quantum research [11, 83–85]. In particular, vertical integration of TMDs into moiré heterostructures enables deliberate design of new functionalities and allows to study strongly correlated states of matter in a controlled way [11].

Monolayer TMDs are characterized by very large effective charge carrier masses on the order of $0.5 m_e$ [73] and by reduced dielectric screening [105]. This leads to very pronounced light-matter coupling that is dominated by tightly bound electron-hole pairs known as excitons [75]. Excitons in TMDs present binding energies of hundreds of meV [75] and act as optical reporters for a range of degrees of freedom such as the charge carrier density or external electric and magnetic fields. So-called optically bright excitons consist of electrons and holes with

the same momentum and spin at either of the high-symmetry momentum points $\pm K$, but also optically dark excitons involving other charge carriers are possible. The crystallographic symmetries of the common TMD atomic structure enforce valley-selective chiral optical selection rules at both $\pm K$ valleys and lead to pronounced spin-valley locking, allowing optical addressing of the valley pseudo-spin degree of freedom.

Ultimately, due to their strong light-matter interaction, excitons in TMDs couple photonic and electronic degrees of freedom and enable non-invasive characterization studies of electronic states under variable charge carrier densities, temperatures, or out-of-plane magnetic and electric fields. It will be the goal of this thesis to establish state of the art understanding of optically bright excitons in the presence of the moiré effect and to use them in order to gain insights on the low-energy moiré physics in the TMD heterostructure $\text{MoSe}_2/\text{WS}_2$.

Experimental techniques

Ever since the industrial revolution and up to the present day, the public debate often pays heed to the rapid technological progress by employing the notion of exponential growth. The paramount success of modern semiconductor electronics exemplifies this idea through the long-term validity of the notorious *Moore's Law* [136] – the empirical observation that the transistor densities on integrated circuits double every 18 to 24 months [137]. This development has been made possible by the common research efforts in basic physics, materials science and electrical engineering [4], and it illustrates in a nice way the principle known as *Kroemer's Lemma of New Technology* [138]. In essence, this principle states that new technologies enable new applications that in their turn drive the demand for these technologies, emphasizing the fundamental importance of technological tools as precursors to progress and subsequently even better new tools.

The field of basic condensed matter research is, at least when viewed as part of the global, value-adding economy, no exception to this rule. In the last decades, rapid progress in material science has been driving the development of tools that became indispensable for the modern laboratory. This included, but was not limited to advances in cryogenics and vacuum technologies, nano-fabrication, laser sources, photodetectors, or electronic data acquisition and analysis devices. This development played a vital role in the boom on van der Waals materials, and it is the goal of this Chapter to introduce the most significant experimental tools that are necessary to study two-dimensional materials in general and TMDs in particular.

We note that parts of this Chapter have been published partly verbatim in Refs. [17, 18]. In section 3.1, we give a short overview of the modern abilities in the nano-fabrication of vdW heterostructures. We introduce the field-effect device architecture that is used throughout this thesis and that allows to control charge carrier densities and out-of-plane electric fields. Afterwards, in section 3.2 we touch on parameters such as temperature or position and discuss the cryogenic requirements posed by the low-energy physics in monolayer TMD structures. Section 3.3 presents the optical setup that is used to study the excitonic resonances discussed in this work. Finally, we close this Chapter by remarking some of the unavoidable challenges encountered in the operation of modern experiments and present ways to mitigate them.

3.1 | Sample fabrication

A common joke in the modern photonics community goes that whatever results are claimed to be new, radio engineers actually did it in the 1910s, with the only difference that now we have access to nano-fabrication [139]. While it is probably a little overstatement, we emphasize that the boom in research on vdW materials has indeed largely been enabled by the democratization of access to nano-fabrication capabilities. In this section, we introduce some of its core concepts related to 2D materials and define the field-effect device architecture that was used in the experimental part of this work.

3.1.1 | Essentials of nanofabrication

Before even considering possible design architectures for elaborate heterostructures, the most important points when dealing with two-dimensional crystals are related to the source and quality of materials and the methods to integrate them into vertical stacks. Similar to the evolution of culinary recipes over time, progress in the field of van der Waals materials has often been achieved through a try-and-error approach, with the introduction of hBN [50] being the best example of this development. Today, there is a whole ecosystem established around the supply of 2D crystals, with both industrial (e.g. *HQ graphene* for bulk graphite or TMD crystals) and academic players (e.g. *National Institute for Materials Science, Japan* for hBN) providing access to high-quality van der Waals materials.

As already introduced in section 2.1, the most important materials in the field of TMD optoelectronics are – among the TMD crystals themselves – few-layer graphene for electric gates and hBN as a passivating substrate layer and a dielectric. Both of these materials are commonly obtained through exfoliation from bulk crystals by the notorious scotch tape method [66], with example flakes shown in Fig. 3.1b, c.

As far as TMDs are concerned, on the other hand, there are currently two competing approaches that produce materials of similar quality. Exfoliated monolayers have been used in a variety of seminal works [13, 16, 89], but are usually subject to uncontrolled exfoliation conditions that limit the homogeneity of the flakes and produce irregular crystal shapes. Since the crystallographic orientation is important for the control of momentum space alignment as well as the moiré effect, there is also an ever increasing attention to monolayers that were directly grown by *Chemical Vapor Deposition* (CVD) [140–143] and that are characterized by regular triangular crystal shapes, see Fig. 3.1a.

For integration of several 2D crystals into vertical vdW structures, a dry-transfer method using stamps of sticky polymers emerged as the easiest way for picking up and releasing individual monolayers [144–146]. The fundamental idea of this approach is based on the observation that

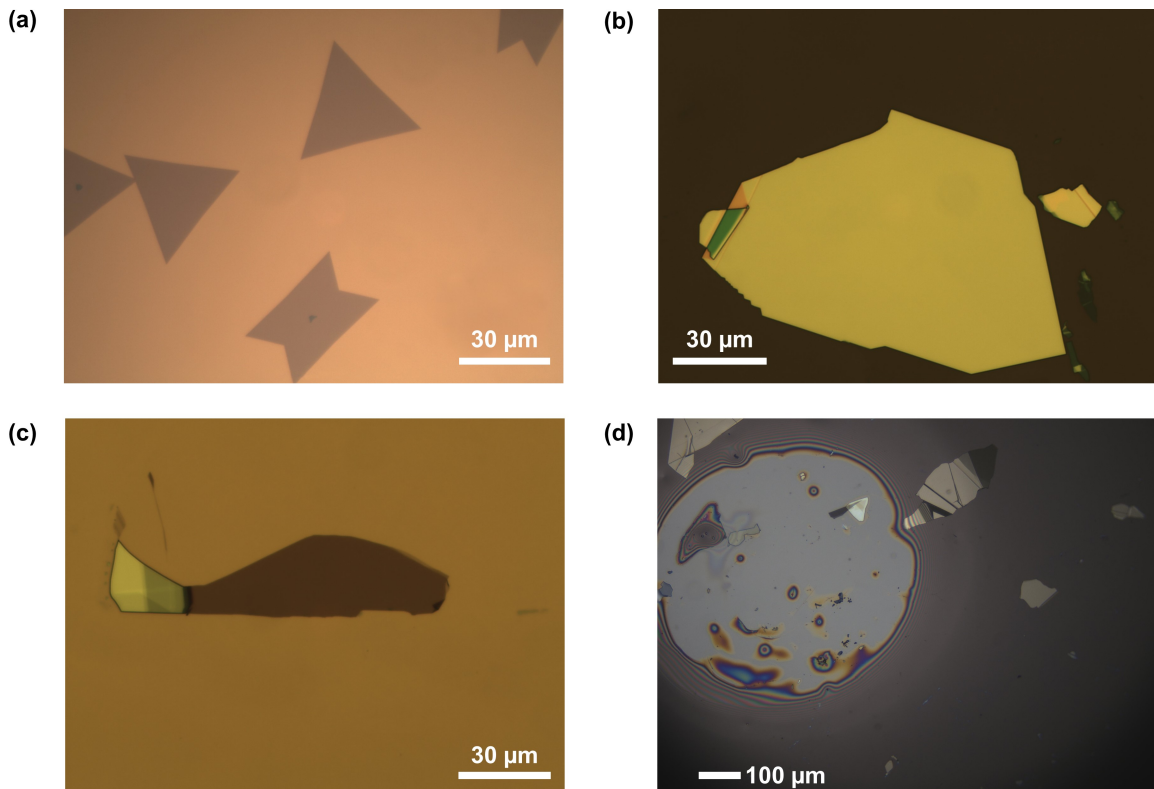


Figure 3.1: (a) Monolayer flakes of MoSe_2 grown by Chemical Vapor Deposition (CVD) on a SiO_2 substrate. (b) Large-area homogeneous flake of exfoliated hBN of approximately 55 nm thickness. (c) Extended homogeneous flake of exfoliated few-layer graphene, used as an electric gate in gated heterostructures. (d) View through the PDMS/PC droplet on a hBN/ MoSe_2 / WS_2 /G stack during the stamping process.

the adhesion forces of polymers strongly depend on the polymer temperature. By varying the temperature, one can therefore control the stickiness of a given polymer stamp to one's liking and pick-up individual monolayers or whole vdW stacks. In this work, we mainly employed thin films of polycarbonates (PC) such as polystyrene deposited on drops of polydimethylsiloxane (PDMS). Figure 3.1d shows the view on a vdW stack through such a PDMS/PC droplet during the process of stamping. The bright, circular area in the left part of the Figure corresponds to the contact area of the PC film to the substrate and is delimited by characteristic interference fringes at the edge to the darker out-of-contact area. By controlling the vertical position of the PC film with micro-positioners, it is possible to increase (or reduce) the contact area in order to cover the stack of interest and to pick it up or release it. Iterative application of this procedure – possibly combined with thermal annealing steps for enhanced homogeneity – allows one to fabricate involved heterostructures consisting of several distinct materials such as the dual gate device presented in the next subsection.

3.1.2 | Field-effect devices for electric field and charge density control

As already introduced in section 2.3, TMDs present an intricate phenomenology related to the presence of free charge carriers or externally applied electric fields. Experiments designed to study or to build upon this behavior naturally require a method to control the corresponding degrees of freedom, and the traditional field-effect device architecture is a straightforward way to simultaneously control both carrier densities and out-of-plane electric fields [147].

For this end, different (semi-) conducting or insulating layers are assembled in a way as to form a plate capacitor with the TMD structure functioning as one of its constituent plates. While early works initially employed global back gates based on the substrate material (e.g. Si/SiO₂ [82] or LaF₃ [148]), state of the art TMD devices nowadays employ few-layer graphene gates, mainly because of its good electric properties combined with transparency in the visible spectral range. Full control of both carrier density and electric fields requires two graphene electrodes as the top and bottom gates together with a separate contact gate coupling the TMD structure to a charge carrier reservoir, see Fig. 3.2b. Figure 3.2a shows a microscope picture of the corresponding, fully assembled and contacted MoSe₂/WS₂ device. Building such a sample requires several stamping steps starting with the top hBN layer and picking up subsequent layers one-by-one, until the whole stack is deposited onto a Si/SiO₂ substrate and covered by the top graphene gate in a last step.

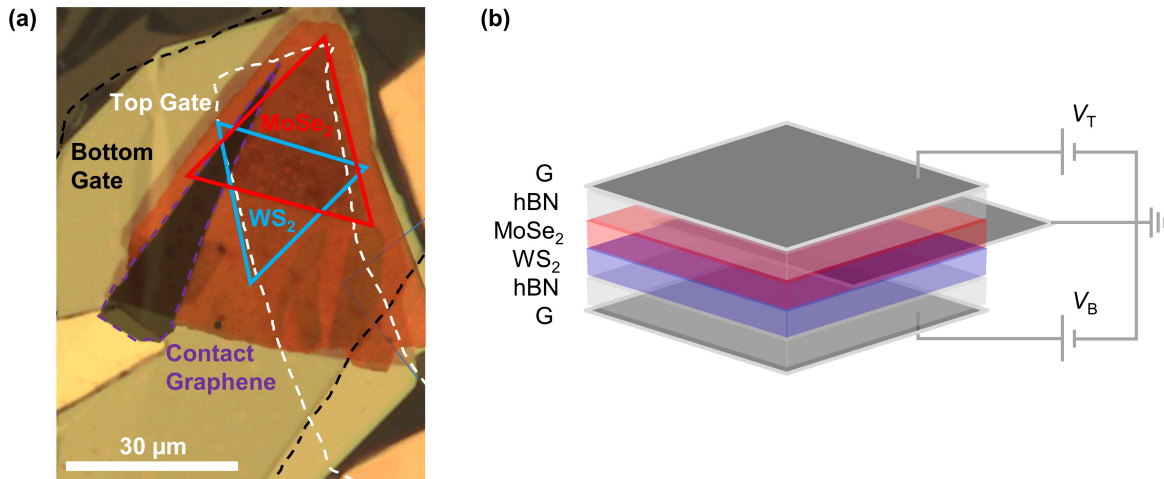


Figure 3.2: (a) Microscope image of a CVD-grown MoSe₂/WS₂ heterostack encapsulated by symmetric hBN spacers of 55 nm each and sandwiched between top and bottom few-layer graphene (G) electrodes. (b) Corresponding schematics of the field-effect device architecture with the denoted externally defined gate voltages at the top, contact, and bottom gates. This Figure was adapted from Ref. [17].

3.2 | Dilution refrigeration and low-temperature position control

Despite the fact that TMDs are characterized by large exciton binding energies of hundreds of meV (and are often studied at ambient conditions), there is a plethora of fundamental questions related to the understanding of the TMD's phenomenology that require cryogenic temperatures. The reason behind this lies in the smaller energy scales associated with the intricate charge and spin physics in TMD structures. The binding energies of trions, for example, range from 20 to 50 meV, the Zeeman and Stark shifts are usually of the order of few meV [75], and the spin exchange coupling in moiré induced charge lattices can be as low as 0.05 meV [13]. To study all these effects it is therefore imperative to have access to temperatures comparable or inferior to those energy scales. Recalling the relation $1 \text{ K} = 0.0862 \text{ meV}/k_B$ implies that regular ^4He cryostats with base temperatures of a few Kelvin are sufficient for most studies of excitonic physics. Studies of spin physics in moiré lattices, on the other hand, necessitate sub-Kelvin temperatures that require more advanced cooling methods such as adiabatic demagnetization or $^3\text{He}/^4\text{He}$ dilution refrigerators [149].

In this work, different studied TMD samples were loaded either into a closed-cycle cryostat (Attocube systems, attoDRY 1000) with a base temperature of 3.2 K or a dilution refrigerator (Leiden Cryogenics) operated between 0.1 and 26 K. Both cryogenic systems were equipped with a superconducting magnet providing magnetic fields of up to $\pm 9 \text{ T}$ in Faraday configuration. Figure 3.3a shows a photograph of the dilution refrigerator setup with the corresponding control electronics on the left. As illustrated by the schematic in Fig. 3.3b, a (dry) dilution refrigerator is characterized by two independent cooling circuits. The first one is just a regular ^4He closed-cycle circuit that provides a base temperature of approximately 3-4 K, while the second one is the actual *dilution* unit with a circulating $^3\text{He}/^4\text{He}$ mixture. The corresponding cooling principle is based on the finite solubility of ^3He in ^4He down to zero temperature [149, 150] and requires that the common evaporator used in other refrigeration cycles be split into a two chamber device consisting of the so-called *mixing chamber* and the *still*. In the mixing chamber, ^3He passes through a phase boundary from a concentrated, ^3He -rich phase to a dilute $^3\text{He}/^4\text{He}$ phase, while in the still the liquid dilute phase is actually evaporated (*distilled*) in order to pump the ^3He . Since the latter is lighter than ^4He , it evaporates much faster and can subsequently be reinserted back into the circuit. Notably, both the phase crossing and the evaporation provide cooling, albeit based on different physical principles. If the circuit contained but ^3He , the evaporative cooling would allow to reach temperatures down to 300 mK, but ultimately, at zero temperature the tendency of any gas to evaporate reduces to zero. In the case of a $^3\text{He}/^4\text{He}$ mixture, on the other hand, the ratio of Fermi liquid ^3He in superfluid ^4He can not fall below 6%.

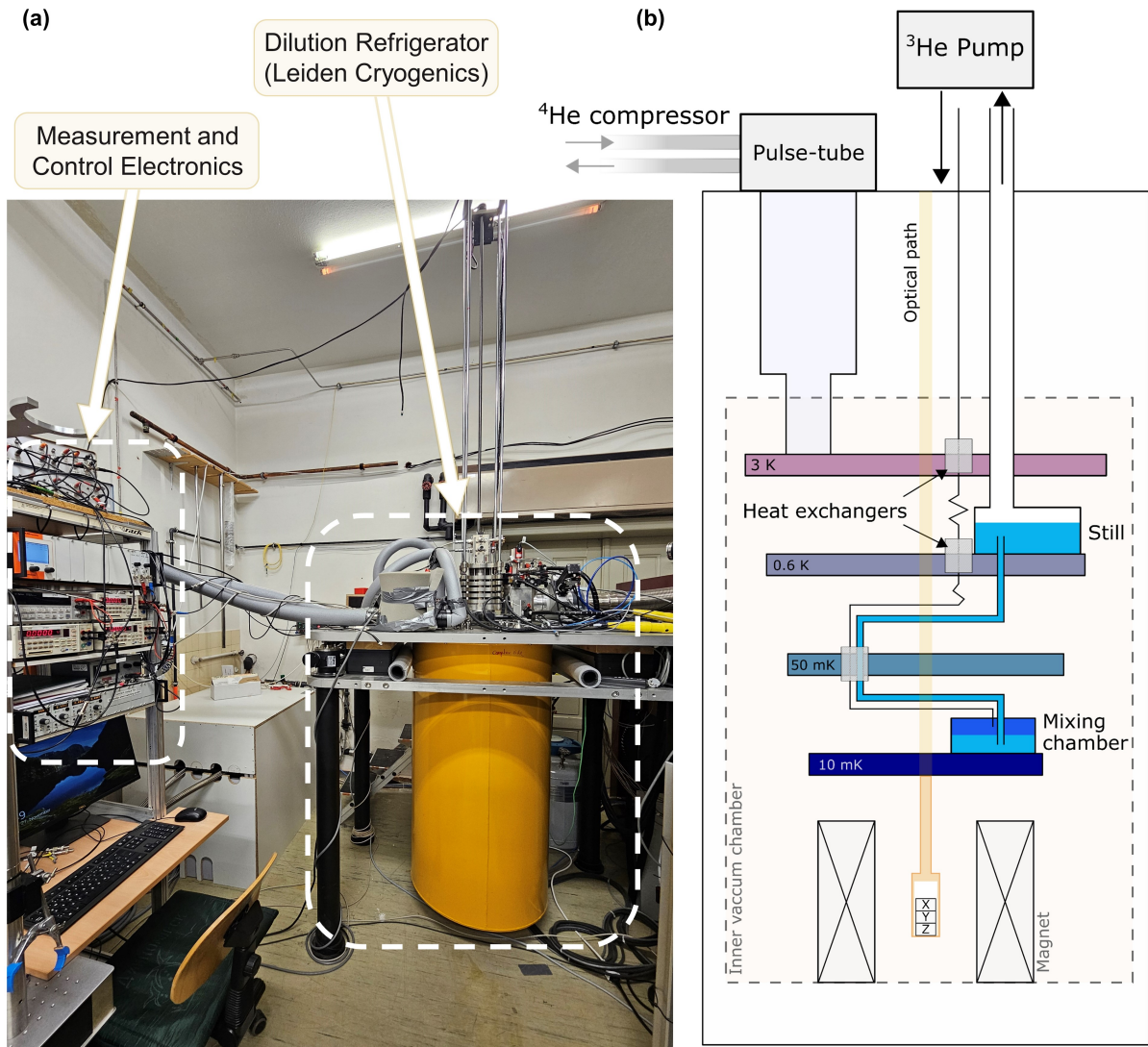


Figure 3.3: (a) Photograph of the dilution refrigerator setup including the cryostat as well as the control electronics on the left. (b) Schematics of the distinct parts inside the dilution refrigerator. The $^3\text{He}/^4\text{He}$ circuit passes through all of the thermal stages up to the mixing chamber at the 10 mK stage, with the dark blue liquid depicting the concentrated ^3He phase and the light blue liquid corresponding to the dilute $^3\text{He}/^4\text{He}$ phase. The main cooling effect happens as the ^3He passes through the phase boundary from the concentrated to the dilute phase in the mixing chamber, after which it is extracted from the still by a turbo pump and reinserted again into the circuit. An experiment cage that is accessible by an optical path is suspended from the 10 mK stage and penetrates into a superconducting magnet where low-temperature piezo positioners (X,Y,Z directions) are used to position the sample with respect to the optical beam spot.

For this reason, crossing of ^3He through the phase boundary has no thermodynamic limitations and can be used to cool down asymptotically to absolute zero.

A particularity of the employed dilution refrigerator lies in the customized optical access from the outside all the way down to the cold stage of the setup. At this stage, a home-built experiment cage unit made of phosphor bronze is thermally attached to the cold plate. It contains a low-temperature apochromatic objective (Attocube systems, LT-APO/VISIR/0.82) and a stack of piezo stepping and scanning positioners (ANP101 and ANS100) that are used to position the sample with respect to the optical beam spot, see Fig. 3.4. Since the positioners introduce a considerable heat load into the system, the actual sample is thermally isolated by an insulating teflon spacer. Instead, it is located on an oxygen-free copper sample holder that is connected to the cage by flexible copper braids. The choice of copper (or bronze as a copper alloy) is motivated by its exceptional thermal conductivity [151] and its very weak magnetic susceptibility [152], with the latter being required by the use of high magnetic fields.



Figure 3.4: Experiment cage made of non-magnetic phosphor bronze with a stack of piezo stepping and scanning positioners from Attocube systems (ANP101 and ANS100). The top plate on the stack is made of oxygen-free copper and it is thermally isolated from the positioners by a teflon spacer. The sample holder is then located on top of this plate and connected to the cold stage by flexible copper braids, allowing for simultaneous cooling and positioning.

3.3 | Confocal microscopy and spectroscopy

Since the discovery of the famous Fraunhofer lines in the spectrum of the Sun light around 210 years ago, spectroscopy became quite possibly the most important characterization tool in condensed matter research. Along its applications to TMDs range throughout large parts of the electromagnetic spectrum and encompass such diverse techniques as static absorption or emission spectroscopy [64], time-dependent pump-probe measurements [153, 154], angle-resolved momentum microscopy [155, 156] or interferometric scattering spectroscopy [157]. It can be performed in the linear or non-linear optics [158] regimes and include elastic or inelastic scattering [159] in both far and near-field optics [160], giving unrivaled insight into the energetic states of the studied samples.

Ultimately, the choice of the spectroscopic technique depends on the type of question that is being asked. In this work, we mainly investigated excitonic transitions in reflection and photoluminescence (PL) spectroscopy by using home-built confocal microscopes in back-scattering geometry. In the following subsections, we give a brief overview of these two techniques. Subsequently, we introduce a type of modulation reflectance spectroscopy that is used to improve the sensitivity to otherwise elusive optical transitions.

3.3.1 | Differential reflectance spectroscopy

The general optical setup used in this work is illustrated in Fig. 3.5. We used a home-built, fiber-based confocal microscope (see also Fig. 3.6) that consisted of an excitation and a detection arm optically connected with an apochromatic objective inside the cryostat. For all measurements, excitation light was inserted through the horizontal arm and reflected into the vertical beam path by a 90/10 beam-splitter, i.e. effectively only 10% of the excitation light were used. The reason for this choice lies in the optimization of detection efficiency: after the reflected or emitted light is collected by the objective, 90% of it can pass through the beam-splitter and couple to the detection fiber that is connected to a spectrometer or a photodiode.

The main characterization tool used in this work is the so-called white-light *Differential Reflectance* (DR), defined as $(R_0 - R)/R_0$ where R is the reflectance signal from the sample and R_0 is a reference background signal from the substrate. The idea of DR is to measure the oscillator strength of the allowed optical transitions which is directly related to the corresponding absorption. Reflectance measurements were typically performed using a stabilized Tungsten-Halogen lamp (Thorlabs, SLS201L) or supercontinuum lasers (NKT Photonics, SuperK Extreme and SuperK Varia) as broadband light sources. The reflection signal was spectrally dispersed by monochromators (Roper Scientific, Acton SP2500 or Acton SpectraPro 300i with a 300 grooves/mm grating) and detected by liquid nitrogen or Peltier cooled charge-coupled devices

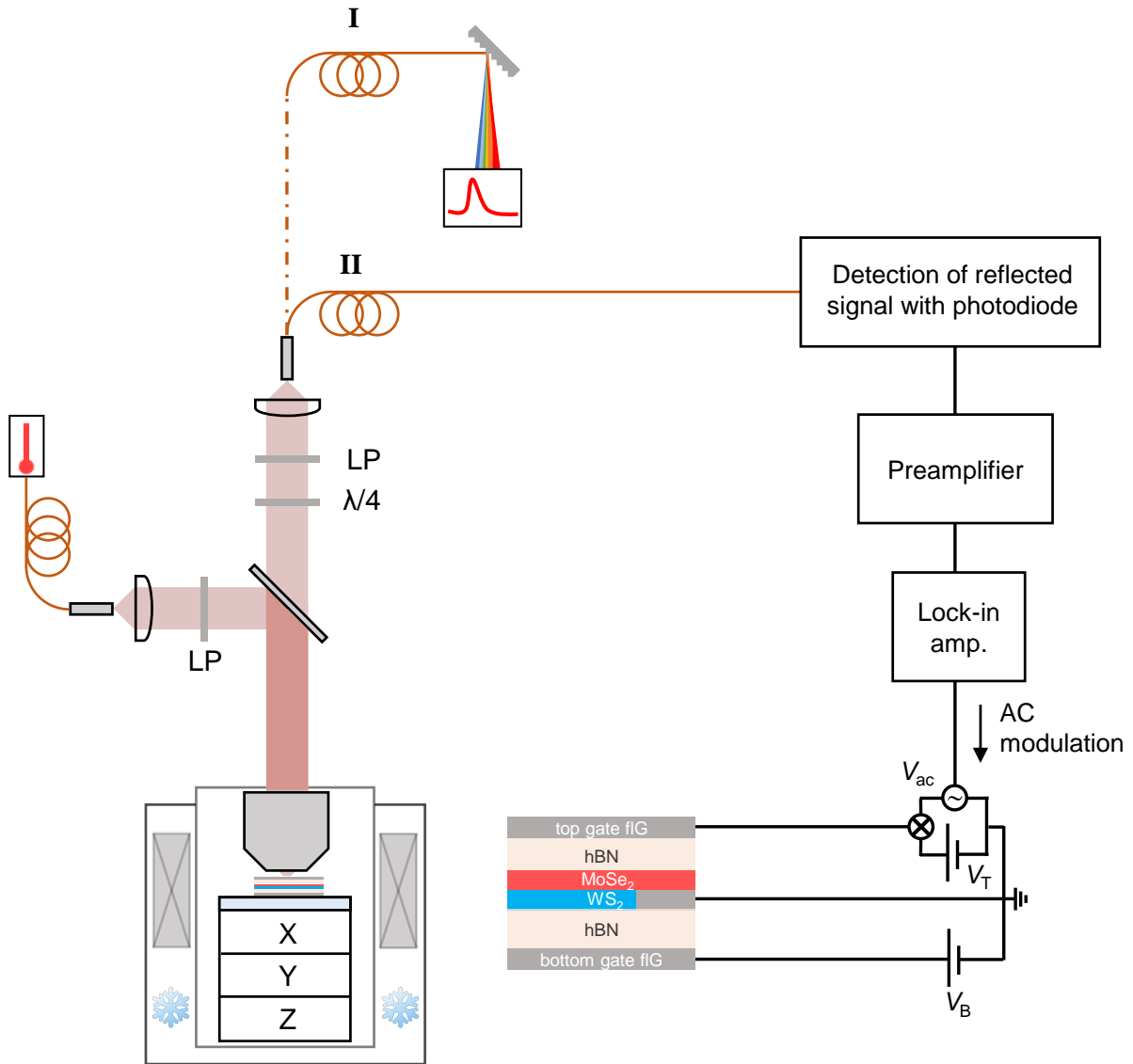


Figure 3.5: Experimental setup for PL and DR measurements (I) and for narrow band modulation spectroscopy (II). The sample is mounted on a stack of piezo positioners (X/Y/Z) inside a closed-cycle cryostat. A home built, fiber-based confocal microscope with an apochromatic objective is used to focus the excitation light (horizontal microscope arm) onto the sample, and the reflected/emitted light is then collected by the same objective and coupled into the detection fiber (vertical microscope arm). The light from the detection fiber is either dispersed by a monochromator for spectral information (I), or detected by a silicon photodiode for narrow-band modulation measurements (II). A set of linear polarizers (LP), waveplates ($\lambda/4$) and optionally also optical filters is used to control the incident light. This Figure was published in Ref. [17].



Figure 3.6: Photograph of the assembled microscope head that was used together with the dilution refrigerator setup.

(Roper Scientific, Spec-10:100BR or Andor, iDus 416). Figure 3.7a-c shows example data obtained on a monolayer flake of MoSe₂ encapsulated by hBN.

The asymmetric lineshape observed in Fig. 3.7c is reminiscent of the notorious Fano resonance [161, 162] and characteristic for integrated TMD devices. We note that without hBN encapsulation, the DR signal would simply be proportional to the imaginary part of the dielectric susceptibility χ'' [163] which in its turn is proportional to absorption. In vdW heterostructures, however, additional interfaces (e.g. introduced by the encapsulating hBN) influence the lineshape of the reflected signal by interference effects. As shown in Ref. [164], these effects can be taken into account by introducing a phenomenological phase factor for the electrical susceptibility,

$$\chi \rightarrow \psi = \chi e^{i\alpha}, \quad (3.1)$$

where α is an *a priori* wavelength-dependent phase factor and the DR signal is now proportional to the imaginary part of ψ , $DR \sim \text{Im}(\psi)$. Here, for simplicity, we assume α to be a constant in

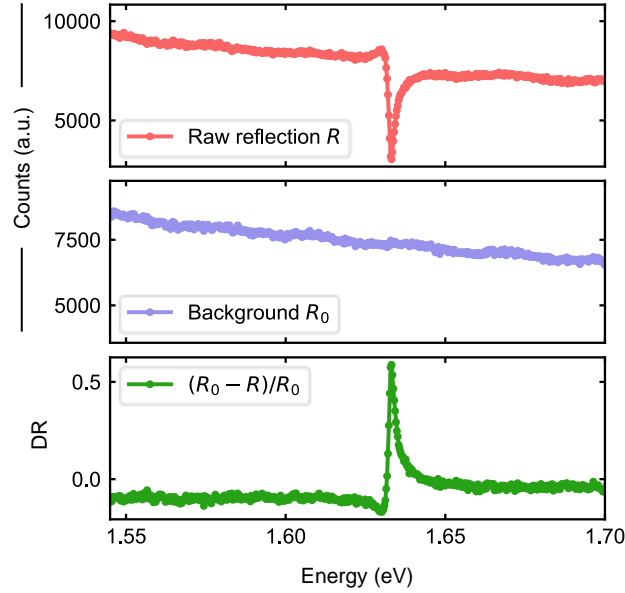


Figure 3.7: *Top panel*: raw reflection signal of a hBN/MoSe₂/hBN stack obtained with a Halogen lamp white light. *Center panel*: neutral background reflection signal obtained in a region of isolated hBN on top of Si/SiO₂. *Bottom panel*: the DR signal computed from the reflectance signal and the background by $DR = (R_0 - R)/R_0$.

the relevant spectral range. Then, using the Kramers-Kronig relations for the complex-valued function $\psi(\omega)$, we can compute χ'' from DR as

$$\begin{aligned}
 \chi''(\omega) &= \text{Im} \left(e^{-i\alpha} \psi(\omega) \right) = \cos(\alpha) \psi'' - \sin(\alpha) \psi' \\
 &= \cos(\alpha) \psi'' - \sin(\alpha) \int_{\mathbb{R}} \frac{\psi''(\omega')}{\omega - \omega'} d\omega' \\
 &= \cos(\alpha) DR(\omega) - \sin(\alpha) \int_{\mathbb{R}} \frac{DR(\omega')}{\omega - \omega'} d\omega'.
 \end{aligned} \tag{3.2}$$

To illustrate this method, we plot the raw DR signal of an encapsulated MoSe₂/WS₂ heterostructure ($\alpha = 0^\circ$) alongside phase-corrected data ($\alpha = 13^\circ$) for better lineshape in Fig. 3.8. A third example with an arbitrary phase for illustration of the principle ($\alpha = -45^\circ$) is also included for completeness. Finally, we emphasize that additional polynomial background correction as detailed in Ref. [165] can be used when visualization of the data requires a uniform signal dispersion.

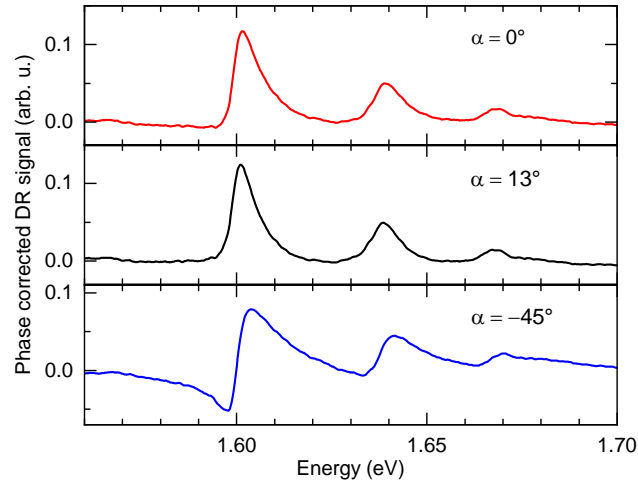


Figure 3.8: *Top panel*: Raw DR signal of an antiparallel, angle-aligned MoSe₂/WS₂ moiré heterostructure. *Center panel*: Phase corrected DR with the phase $\alpha = 13^\circ$ for better lineshape. *Bottom panel*: Phase corrected DR with $\alpha = -45^\circ$. One can see that the phase affects the lineshape of the resonances without changing their widths nor resonance energies. This Figure was published in Ref. [17].

3.3.2 | Photoluminescence spectroscopy

Alongside DR, photoluminescence spectroscopy (PL) is arguably the most basic optical characterization method for studies of semiconductors. It is based on the observation that charge carriers that get optically excited by the absorption of a photon eventually end up relaxing back to their ground state. If the energy difference between the lowest excited state and the ground state is non-zero (as is the case for gapped materials like insulators and semiconductors), and if the optical selection rules allow a transition between the two, the relaxation can be of radiative character and involve the re-emission of a photon.

The advantage of PL lies in the fact that in first order, one can use any excitation wavelength that has a higher photon energy than the studied transition. Contrary to absorption or reflection spectroscopy, however, PL signals are not necessarily proportional to the oscillator strength of a given transition. Instead, PL measures the quasiparticle population of a given excited state. Excited carriers are generally subject to a range of different physical processes with several distinct time scales, including phononic relaxation and radiative or non-radiative recombination processes. In TMDs, phonon-mediated intraband relaxation happens on a sub-ps time scale and is typically an order of magnitude faster than radiative recombination [166], implying that PL from higher energy states is strongly quenched [17]. On the lower energy side, however, it is often possible to observe pronounced phonon replica side bands. This is especially the case in W-based TMDs in which the lowest energy transition is spin-forbidden and recombination

therefore requires the involvement of phonons [167, 168].

In this work, we studied MoSe₂/WS₂ heterostructures in which the fundamental transitions appear at an energy around 1.65 eV or a wavelength of 750 nm. To study them in PL, we therefore mostly used a red semiconductor diode laser with a wavelength of 690 nm or an energy of 1.8 eV. Typically, a short pass filter (Semrock FF01-720SP) was mounted in the excitation arm and a long pass filter (Semrock FF01-715LP) in the detection arm to disentangle excitation from emission.

3.3.3 | Modulation spectroscopy

Conventional DR is intrinsically limited to optically bright transitions. To improve the sensitivity to darkish states, it is possible to use the modulation-spectroscopy technique – an approach that uses a narrow-band tunable laser to measure differential reflectance DR' [169–171]. For the measurement, we typically employed a wavelength-tunable Ti:sapphire laser (M squared) of 50 μ eV linewidth to excite the sample while modulating the top gate with an ac-voltage $V_{ac} = 500$ mV at 147 Hz. The reflected optical signal was detected by a silicon photodiode and its output was preamplified by the Ithaco Model 1211. The amplified dc-part of the photosignal (R_{dc}) was measured, and the ac-part was demodulated and further amplified by a lock-in amplifier (EG&G 7260) supplied with the same reference frequency as that of the modulation voltage to obtain R_{ac} . Finally, the narrow-band differential reflectance is given by the ratio of the demodulated ac part to the dc photosignal, $DR' = R_{ac}/R_{dc}$. We used an integration time constant of 1 s per data point acquisition to obtain sensitivity to otherwise elusive transitions such as interlayer excitons presented in Chapter 5. In simple limits of the modulation conditions, the signal is proportional to the derivative of DR [169], whereas in general, it requires a microscopic analysis including optical pumping of charge carrier reservoirs.

3.4 | Experimental challenges and solutions

In a perfect world we might all live in communism, wars and crises would be vague notions from the past, and all scientific instruments and measurements would work as expected. Unfortunately, this is still far from being true, and maybe it will never be. Regardless of all technological progress there are unalienable natural laws – entropy continues increasing, decoherence separates the quantum world from the classical one, and doctoral students have to fight the unknown. Notably, operating a modern laboratory is often inextricably linked with facing instrumentation bottlenecks and developing measurement protocols. In this section, we exemplify this problem by presenting three representative issues encountered in the experimental part of this work and discuss possible ways to mitigate them.

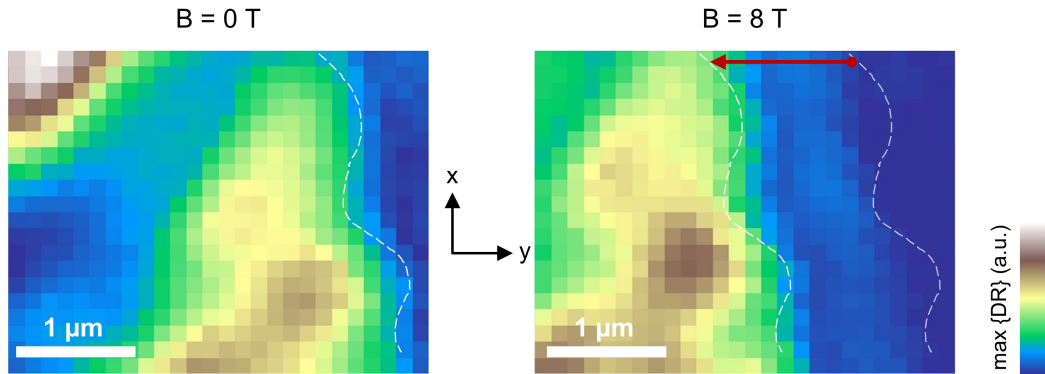


Figure 3.9: Positional drift of the device with varying magnetic field, visualized by hyperspectral position maps of an exfoliated $\text{MoSe}_2/\text{WS}_2$ sample where each pixel is colored according to the maximum value of DR at that position acquired in σ^- polarization. The left panel shows the map at zero magnetic field, and the right panel shows a map acquired under identical conditions, but for an out-of-plane magnetic field of $B = 8$ T, with the latter resulting in a lateral shift of the device on the order of $1 \mu\text{m}$.

3.4.1 | Landé-factors and position drift with changing magnetic field

We already mentioned above that the dispersion of an exciton in an out-of-plane magnetic field – quantified by the magnetic Landé g -factor – can provide valuable insight on both the nature of the involved electronic bands as well as the local magnetization. To measure a g -factor, it is necessary to determine the exciton transition energies in σ^+ and σ^- polarizations for several values of the magnetic field and subsequently perform a linear fit to obtain the proportionality constant between them, see Eq. (2.10). Unfortunately, typical examples of van der Waals devices present considerable degrees of disorder, leading to variations of the exciton energies up to tens of meV across any given sample. For meaningful results, it is therefore imperative to ensure that different measurements are performed at the same spatial position. In reality, however, it turns out that a changing magnetic field often leads to uncontrolled spatial drifts of the studied samples. In Fig. 3.9, we show two hyperspectral position maps obtained by displacing the sample by the piezo positioners with respect to the objective. In this experiment, changing the magnetic field from $B = 0$ T to $B = 8$ T lead to a drift of approximately $1 \mu\text{m}$, which is larger than the diffraction-limited optical spot size and can strongly affect the acquired data. Luckily, in that particular case the diagnosis directly yields the solution to the problem: to ensure the comparability of different data points, measurements that were performed at large magnetic fields always included a spatial scan in order to manually fix the spot of interest to a given position on the sample.

3.4.2 | Charge doping blockades

In many measurements we also faced sizable charge doping blockades that we illustrate by data on monolayer MoSe₂ in Fig. 3.10. Here, the positive gate voltage $V_G = V_T = V_B$ induces free electrons inside the TMD layer, with the onset of doping visualized by the vanishing of the neutral A-exciton at 1.64 eV and the appearance of a negative attractive polaron resonance around 1.615 eV. With low-power incident light, doping would not set in until a sudden and uncontrolled breakthrough, whereas for medium-power incident light, it occurred much earlier. This behavior is indicative of sizable Schottky-barriers that are passivated by photo-generated charge carriers, so higher illumination power naturally produced the best results. At lowest temperatures, however, strong incident light might influence the local temperature and thus corrupt the obtained data [16]. In our experiments, this could be observed in the data on the magnetic susceptibility of the moiré spin-charge lattice in angle-aligned MoSe₂/WS₂, see Chapter 5. For this reason, to guarantee comparability in the charge filling and unperturbed spin-correlations, we employed a method that we call *laser-assisted charge doping*. For the latter, we performed actual measurements with a low illumination power of 300 pW, but added a 200 μ W laser light (690 nm diode laser co-inserted with the white-light by a fiber beam-splitter) during each change in the applied gate-voltage, resulting in the algorithm:

Algorithm 1: Laser-assisted charge doping

Input: gate voltages V_1, \dots, V_N ;
 $i \leftarrow 1$;
while $i \leq N$ **do**
 ◇ Turn 200 μ W laser on;
 ◇ Set $V_G \leftarrow V_i$;
 ◇ Turn 200 μ W laser off;
 ◇ Wait until the sample temperature equilibrates;
 ◇ Measure DR in low-power illumination;
 ◇ $i \leftarrow i + 1$;
end

3.4.3 | Data complexity and software-driven automatization for data acquisition and analysis

We close this Chapter by emphasizing the complexity of modern research questions that is partially introduced by the need of multidimensional data sets. Today, most scientific questions require efficient pipelines for both data acquisition and analysis, with state of the art facilities like the CERN treating terabytes of data daily.

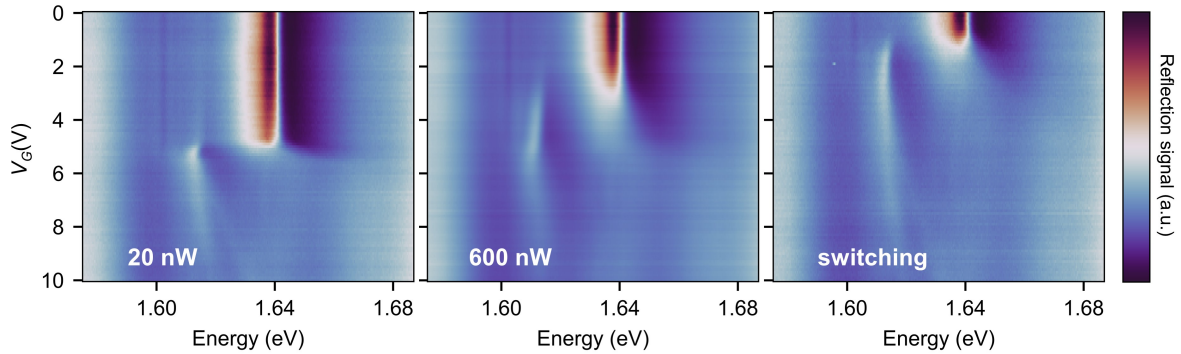


Figure 3.10: Comparison of optical reflectance data in monolayer MoSe₂. The left panel shows the evolution of the signal as obtained with a white-light illumination of 20 nW incident power. Under these conditions, the neutral exciton visible at 1.64 eV did not respond to the gate voltage until a sudden breakthrough at around 5 V, and fast, non-linear evolution of the emerging trion afterwards. The central panel shows the corresponding measurement at a higher incident power of 600 nW, which presents a doping onset around 3 V and a smoother evolution of the emerging trion. Finally, the right panel was obtained by the laser-switching technique described above, i.e. by measuring reflectance in low power (here 20 nW) and changing the gate voltage while simultaneously illuminating the sample by a strong 690 nm diode laser of approximately 200 μ W power.

Related to this work, the increasing amount of data can be seen in the requirements posed by the measurements of exciton g -factors. Obtaining the value of one g -factor requires only the variation of the magnetic field and produces reasonable results with about ten data points. If one wants to study the behavior of the g -factor of charged excitons, it is necessary to introduce the parameter of the charge density, so studying the magnetic dispersion of trions at ten representative carrier densities already requires about $10^2 = 100$ data points. Finally, studies of correlated many-body states with signatures of correlated magnetism introduce the parameter of temperature that can strongly influence the magnetic susceptibility. As a result, a modest set of ten distinct temperatures leads to $10^3 = 1000$ data points, illustrating the exponential growth of data needed to ask advanced scientific questions.

It would obviously be a vain attempt to try to collect all the necessary data manually. For this reason, it is important to develop robust and efficient tools that can automatize both data acquisition and analysis and allow for fast-paced iteration of measurements and evaluation. For the present work, this included development of software control in *Python* – a language known for its extended scientific ecosystem and its wide compatibility with other technologies. In the appendix, we show some selected *Python* scripts that have proved extremely beneficial for the evolution of this work.

Theoretical models

Among the substantial advances in experimental techniques presented in the previous Chapter, the explosion of digital computing capabilities that unfolded in the last 30 years led to rapid progress in numerical simulations and theoretical techniques relevant for condensed matter physics. New algorithms such as tensor-network approaches for quantum many-body problems [172, 173] or open-source software packages for first-principle calculations [174] triggered a new era in theoretical research, allowing to study previously elusive physical problems numerically as well as to use the simulation insights to develop new analytic approaches.

In this Chapter, we present some important theoretical models that are essential to study excitons and charges in periodic moiré lattices. We start by introducing the moiré geometry in section 4.1 where we familiarize ourselves with the relevant length scales. In section 4.2, we present the limitations of the simple geometric approach to moiré patterns and mention the notorious effect of periodic lattice reconstruction. Subsequently, in section 4.3 we build upon the fact that reconstruction is inhibited in incommensurate bilayers such as $\text{MoSe}_2/\text{WS}_2$ and develop an effective continuum model that describes intra- and interlayer excitons in the presence of a triangular moiré lattice. Section 4.4 describes an electrostatic model that we use to study charge density doping in the presence of a peaked density of states. Finally, we close this Chapter by invoking the behavior of excitons in the presence of periodic charge lattices. We note that similar to Chapters 3 and 5, parts of this Chapter have been published partly verbatim in Refs. [17, 18], with section 4.3 falling under the copyright of the American Physical Society.

4.1 | Moiré geometry in bilayer van der Waals structures

To understand how the moiré pattern depends on the relative twist or lattice mismatch between two layers, we need to reconsider the basic geometry of two-dimensional lattices in general and of the honeycomb lattice in particular.

For a minimal theory of moiré superlattices [86], we assume that $\hat{a}_{1/2}$ are the basis vectors

of a 2D Bravais lattice. It is instructive to write them in a matrix notation,

$$A := \left(\hat{a}_1 | \hat{a}_2 \right), \quad (4.1)$$

such that the reciprocal vectors can be written in the form

$$\left(\hat{g}_1^A | \hat{g}_2^A \right) = 2\pi(A^{-1})^T =: G_A. \quad (4.2)$$

When two different lattices A and B with basis vectors $\hat{a}_{1/2}$ and $\hat{b}_{1/2}$ are stacked on top of each other, we can expand any B -periodic function $f_B(\vec{x})$ both in the A and B reciprocal space, i.e.

$$f_B(\vec{x}) = \sum_{\vec{n}} c_{\vec{n}} e^{i(n_1 \hat{g}_1^B + n_2 \hat{g}_2^B) \vec{x}} = \sum_{\vec{n}} e^{i(n_1 \hat{g}_1^A + n_2 \hat{g}_2^A) \vec{x}} \underbrace{\left[c_{\vec{n}} e^{i(n_1 (\hat{g}_1^B - \hat{g}_1^A) + n_2 (\hat{g}_2^B - \hat{g}_2^A)) \vec{x}} \right]}_{\text{Periodic modulation on top of the A lattice}}. \quad (4.3)$$

Since f_B is not A -periodic, its expansion coefficients with respect to the reciprocal vectors $\hat{g}_{1/2}^A$ are not constant in \vec{x} themselves, but rather present periodic modulations with a periodicity defined by the reciprocal vectors $G_m = G_B - G_A$. This periodicity arises from the long-range moiré superlattice illustrated in Fig. 4.1b, allowing us to obtain the moiré lattice vectors from G_m through matrix inversion by simply reading off the column vectors of $(G_m^T)^{-1} / (2\pi)$.

In the following, we illustrate this procedure for the case when both lattices A and B share the honeycomb geometry. For the first lattice, we assume the same basis vectors as in Eq. (2.1), but write them as a function of the lattice constant $a_0 = \sqrt{3}a$ as defined in Fig. 4.1a. With this choice, we can conveniently write them as

$$\hat{a}_1 = a_0 \begin{pmatrix} \sin \pi/3 \\ \cos \pi/3 \end{pmatrix}, \quad \hat{a}_2 = a_0 \begin{pmatrix} \sin \pi/3 \\ -\cos \pi/3 \end{pmatrix}. \quad (4.4)$$

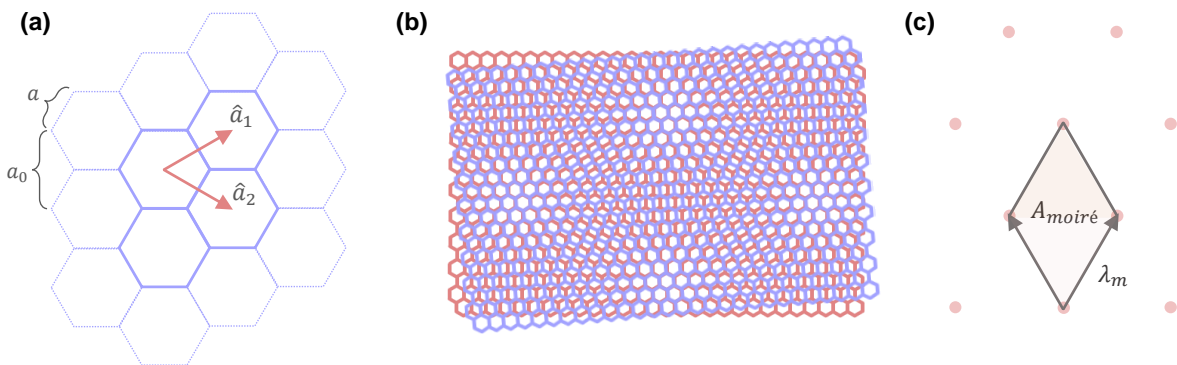


Figure 4.1: (a) Geometry of the honeycomb lattice. Here, in order to facilitate the computations we work with the lattice constant $a_0 = \sqrt{3}a$ instead of the atomic bond distance a (cp. Fig. 2.1). (b) Schematics of the moiré pattern in two stacked hexagonal lattices with a twist of 5° . (c) The moiré pattern in (b) presents a triangular geometry with a lattice constant λ_m . The corresponding moiré density reads $n_0 = 1/A_{\text{moiré}}$ with $A_{\text{moiré}} = \lambda_m^2 \sqrt{3}/2$.

For the second lattice B , we assume a relative twist angle of θ and a different lattice constant b_0 . By introducing the rotation matrix

$$R = \begin{pmatrix} \cos \theta & -\sin \theta \\ \sin \theta & \cos \theta \end{pmatrix}, \quad (4.5)$$

we can write its basis vectors as $B := (\hat{b}_1 | \hat{b}_2) = \frac{b_0}{a_0} RA$. This corresponds to the explicit form of

$$\hat{b}_1 = b_0 \begin{pmatrix} \sin(\pi/3 - \theta) \\ \cos(\pi/3 - \theta) \end{pmatrix}, \quad \hat{b}_2 = b_0 \begin{pmatrix} \sin(\pi/3 + \theta) \\ -\cos(\pi/3 + \theta) \end{pmatrix}, \quad (4.6)$$

but it is more convenient to work in matrix notation. In particular, recalling that a rotation matrix is orthogonal (i.e. $R^T = R^{-1}$), the reciprocal basis vectors of the lattice B can be directly written as $G_B = 2\pi \frac{a_0}{b_0} (A^{-1}R^{-1})^T = \frac{a_0}{b_0} RG_A$. This allows us to write down the moiré reciprocal vectors in the case of scaled and twisted triangular lattices,

$$G_m = G_B - G_A = \left(\frac{a_0}{b_0}R - \mathbb{1}\right)G_A. \quad (4.7)$$

With this, we finally obtain the moiré unit vectors to be given by

$$(\hat{\lambda}_1^m | \hat{\lambda}_2^m) = M := \frac{1}{2\pi} (G_m^T)^{-1} = \left(\frac{a_0}{b_0}R^T - \mathbb{1}\right)^{-1} A = \left(\frac{a_0}{b_0} - R\right)^{-1} RA = \left(\mathbb{1} - \frac{b_0}{a_0}R\right)^{-1} B. \quad (4.8)$$

By defining the lattice mismatch parameter $\delta = (a_0 - b_0)/b_0$, a straightforward exercise in matrix inversion yields an analytic expression for M :

$$M = \frac{1 + \delta}{2(1 + \delta)(1 - \cos \theta) + \delta^2} \begin{pmatrix} 1 + \delta - \cos \theta & -\sin \theta \\ \sin \theta & 1 + \delta - \cos \theta \end{pmatrix} B. \quad (4.9)$$

Despite the intimidating impression, Eq. (4.9) has a straightforward interpretation. The whole prefactor that is multiplied with B is nothing but an orthogonal rotation matrix with an additional scaling factor, so the moiré lattice itself can be understood as a rotated and stretched lattice B . By carefully keeping track of all factors, one deduces that the moiré lattice constant is given by

$$\lambda_m = \frac{b_0(1 + \delta)}{\sqrt{2(1 + \delta)(1 - \cos \theta) + \delta^2}}, \quad (4.10)$$

which for small twist angles θ and lattice mismatches δ reduces to the familiar relation [11]

$$\lambda_m \approx \frac{a_0}{\sqrt{\theta^2 + \delta^2}}. \quad (4.11)$$

The area of a moiré unit cell is then given by $A_{\text{moiré}} = \lambda_m^2 \sqrt{3}/2$ as illustrated in Fig. 4.1c, which leads to a moiré density of $n_0 = 1/A_{\text{moiré}}$. In this work, the materials studied have the lattice constants of $a_0 = 0.3289$ nm for MoSe₂ and $b_0 = 0.3154$ nm for WS₂ [73]. This defines a lattice mismatch of $\delta \approx 0.04$, which for small θ results in superlattice constants around 7 – 8 nm and moiré densities of around 2.0×10^{12} /cm², see Table 4.1.

θ	0°	1°	2°
λ_m	7.7 nm	7.1 nm	5.9 nm
n_0	$1.95 \frac{10^{12}}{\text{cm}^2}$	$2.3 \frac{10^{12}}{\text{cm}^2}$	$3.3 \frac{10^{12}}{\text{cm}^2}$

Table 4.1: Moiré lattice constant and density in MoSe₂/WS₂ as a function of θ .

4.2 | Lattice reconstruction as an obstacle to moiré physics in commensurate bilayers

The mathematical treatment of the moiré lattice presented above is sometimes deemed 'naive' because of the idealized assumptions of robust monolayers. Mathematically, the three-fold rotational symmetry inherent to TMD monolayers implies that there are two distinct, long-range moiré patterns that can be obtained in either parallel (R-type, $\theta = 0^\circ$) or antiparallel (H-type, $\theta = 60^\circ$) alignment as shown in Fig. 4.2. A microscopic study of these limiting cases reveals that in both configurations there are periodically repeated high-symmetry points such as MM, MX, XM and XX [11], where M stands for metal and X for chalcogen atoms.

In real TMD heterostructures, all of these different atomic registries possess distinct inter-layer adhesion energies that compete with intralayer elastic strain and distort the homogeneity of the flat monolayers. The result of this competition is commonly referred to as atomic and mesoscopic reconstruction [12, 175–179] and it can substantially influence the emergent moiré superlattice. In particular in lattice-commensurate bilayers that share the same lattice constant, mesoscopic reconstruction leads to uncontrolled propagation of lattice defects which can effectively change the local dimensionality of the structure [12]. In TMDs, the lattice constant is mainly determined by the chalcogen atoms, with studies on selenide-based heterostructures such as MoSe₂/WSe₂ revealing a range of 0D (quantum dot), 1D (quantum wire) and extended 2D (quantum well) structures all within the same microscopic samples.

Heterostructures with different chalcogens, on the other side, typically feature a relatively large lattice mismatch of 4% which impedes lattice reconstruction and stabilizes the canonical triangular moiré geometry shown in Fig. 4.2. In this limit, the moiré pattern varies spatially through the points of high-symmetry registries. For these reasons, many seminal works on moiré physics in TMD structures have been performed in the type II WS₂/WSe₂ heterostacks, with recent examples of many-body Hubbard model physics [180] including demonstrations of correlation-induced magnetism [13], Mott insulating states [181–185], two-dimensional Wigner crystals of electrons [89, 181] at fractional and integer fillings as well as stripes at half-filling factors [186].

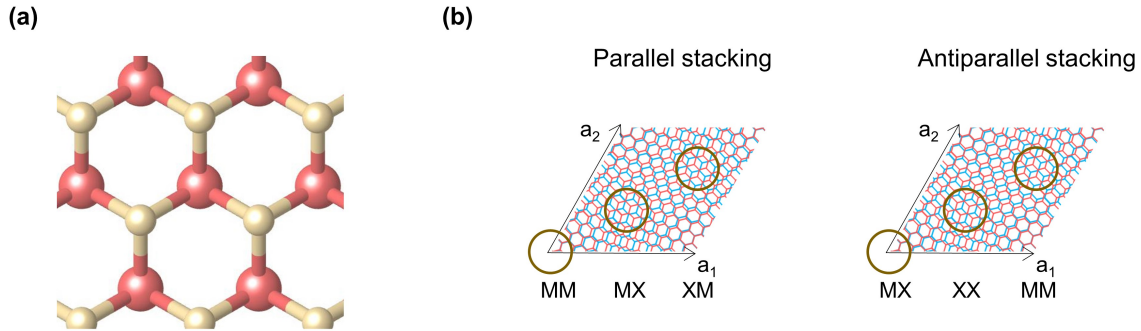


Figure 4.2: (a) Three-fold rotational symmetry of a TMD monolayer. (b) Because of the 120° symmetry in TMD monolayers, the moiré pattern differs between parallel (R-type, 0°) and antiparallel (H-type, 60°) alignment. In both limits, the moiré pattern varies spatially through points of high-symmetry registries such as MM, MX, XM and XX [11] where M stands for metal and X for chalcogen atoms.

The periodically modulated moiré potentials for electrons, holes and excitons [180, 187–189] give rise to distinct, energetically favored spatial positions of these quasiparticles and thus provide a scaffold for correlated electronic states [11, 87, 88]. Among the extensively studied WS_2/WSe_2 heterostructure, $MoSe_2/WS_2$ is the next most natural candidate for the implementation of a stabilized moiré lattice and correlated many-body states. In contrast to WS_2/WSe_2 or $MoSe_2/WSe_2$, which have conduction (CB) and valence band (VB) offsets of a few hundreds of meV, *ab initio* studies have shown that the CBs of $MoSe_2$ and WS_2 are much closer [14]. At the same time, the low accuracy inherent to DFT calculations and the complications arising from the CB resonance repeatedly obscured the precise energetic ordering of the lowest conduction bands. The nature of the lowest energy moiré excitons in $MoSe_2/WS_2$ therefore remains matter of continuing debate, with reported CB offset values ranging between -20 meV [190] and $+100$ meV [15].

4.3 | Continuum models for excitons in incommensurate bilayers

We emphasize that the moiré potential generally gives rise to pronounced exciton mixing by umklapp-scattering off the long-range superlattice, resulting in robust moiré excitons [15, 17, 190–192] as observed in Fig. 3.8. The interpretation of optical data, however, is often limited by the lack of microscopic understanding of such moiré excitons and their interactions with charge carriers. A moiré supercell usually contains thousands of atoms, making full first-principle cal-

culations of moiré exciton bands remain particularly hard [193]. Common approaches to model moiré excitons therefore mainly focus on two different continuum models. On the one hand, studies on WS_2/WSe_2 or $MoSe_2/WSe_2$ with large band offsets [14] repeatedly relied on introducing a phenomenological moiré potential for intra- (X) or interlayer (IX) excitons [165, 180, 187, 188, 194]. For nearly aligned bands, on the other hand, resonant interlayer tunneling was argued to play the dominant role, and therefore a model describing full interlayer hybridization of resonant bands has been developed [195, 196]. In the former approach, it is possible to account for the emergence of distinct moiré exciton bands while missing on hybridization between intra- and interlayer excitons, whereas in the latter, intralayer states differing by moiré reciprocal vectors can not mix but through a second order process. It turns out that in $MoSe_2/WSe_2$, both effects have to be taken into account, and we proceed by introducing a continuum model that combines a phenomenological potential with interlayer hybridization and allows us to describe the complexity of both intra- and interlayer excitons in $MoSe_2/WSe_2$ simultaneously. We note that during the course of this thesis, similar results have been published in Refs. [197–199].

4.3.1 | Two-dimensional moiré band folding

The effect of a moiré pattern can be vaguely split into a geometric and an energetic contribution. The former is motivated by the simple fact that the longer periodicity of the superlattice as illustrated in Fig. 4.1b gives rise to a new mini Brillouin zone (mBZ) in the reciprocal space. The geometry of the reciprocal space enables new umklapp-scattering off the moiré superlattice, leading to the folding of the quasiparticle bands (i.e. electrons, holes or excitons) inside the

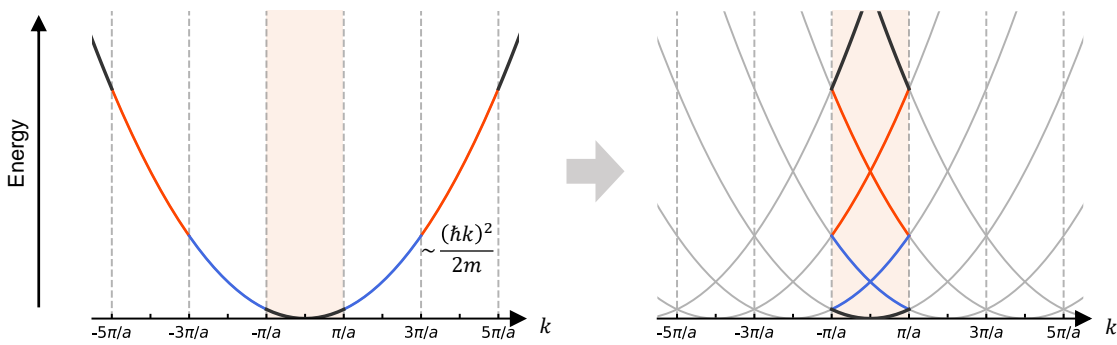


Figure 4.3: **One-dimensional band folding.** The energy dispersion of a simple free electron in a one-dimensional periodic potential of periodicity a takes the form of a parabola and can be presented in the so-called extended (left) and reduced (right) zone schemes. In the latter, every wave vectors k in the reciprocal space is associated with a crystal-momentum inside the first Brillouin zone (shaded in pink).

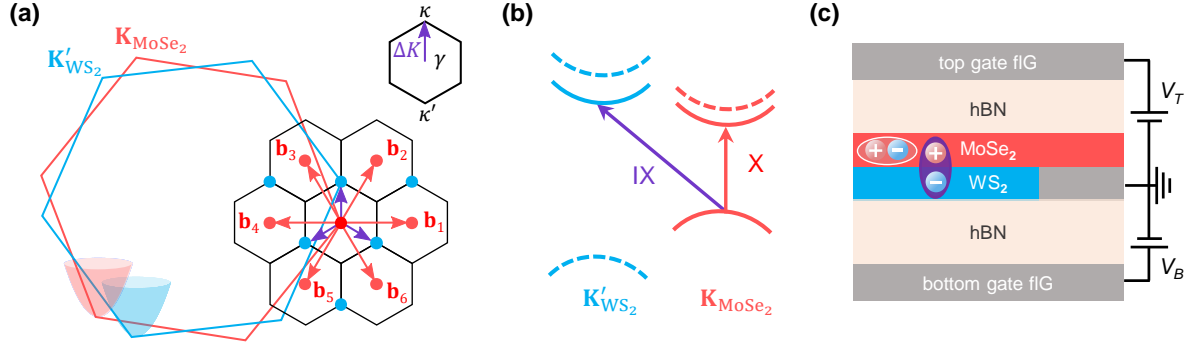


Figure 4.4: **Reciprocal space geometry for the continuum exciton model.** (a) Mini Brillouin zones with moiré reciprocal vectors \mathbf{b}_j (red arrows) and interlayer coupling (violet arrows). The red and blue points represent intra- and interlayer states considered in the model [17]. (b) Band structure of antiparallel MoSe₂/WS₂ with spin-polarized subbands indicated by solid and dashed lines, as well as intra- and interlayer excitons. (c) Schematics of the MoSe₂/WS₂ heterostructure with depicted intra- and interlayer excitons in a field-effect device, with top and bottom gate voltages V_T and V_B .

mBZ to form so-called moiré bands. The energetic contribution, on the other side, builds upon the actual moiré potential that introduces an interaction between the different folded moiré bands and can lead to the emergence of the notorious correlated flat bands [87].

The geometric idea of band folding can be motivated by the textbook discussion on the visualization of the reciprocal space. To illustrate the procedure, we show the folding of a parabolic band in a one-dimensional space in Fig. 4.3. For this, we note that low-energy electrons in a semiconductor can generally be studied in the effective mass approximation, i.e. with a Taylor-expanded parabolic dispersion $E(k) = (\hbar k)^2/2m$ that is reminiscent of free electrons with a renormalized mass. The full parabola can be visualized in the so-called extended zone scheme as shown on the left of Fig. 4.3. In the same time, the discrete periodicity of a regular lattice (e.g. here with a lattice constant a) means that all momenta in the reciprocal space can also be associated with a crystal-momentum inside the first Brillouin zone, resulting in the more familiar reduced zone scheme shown on the right of Fig. 4.3. The effect of the latter visualization is equivalent to subsequent folding of the original parabola into the Brillouin zone and introduces distinct energy bands that can be quantified according to the number of folding steps required.

In the two-dimensional case, the basic idea of band folding remains the same while the geometry of the moiré lattice, and hence also of the mini Brillouin zone, is generally more complex. Here, we restrict the discussion to the case of a triangular moiré pattern in a MoSe₂/WS₂ heterostructure emerging from two honeycomb lattices as introduced in section 4.1. We assume an antiparallel alignment between a MoSe₂ and a WS₂ layer with a small twist angle θ

and lattice constant mismatch δ that result in a small valley mismatch which we denote by $\Delta\mathbf{K} = \mathbf{K}'_{\text{WS}_2} - \mathbf{K}_{\text{MoSe}_2}$. The long-range periodicity of the moiré lattice is reflected by the formation of a mini Brillouin zone [86] with the moiré reciprocal lattice vectors $\mathbf{g}(n, m) = n\mathbf{b}_1 + m\mathbf{b}_2$ shown in Fig. 4.4a. Here, n and m are integers, $\mathbf{b}_j = (C_6^{j-3} - C_6^{j+1})\Delta\mathbf{K}$ are the first-shell reciprocal lattice vectors, $j = 1, 2, \dots, 6$, and C_6^μ represents rotation by $2\pi\mu/6$ (Fig. 4.4a). We define the angle-dependent mBZ with the center γ matching the K -valley of MoSe₂ ($\mathbf{K}_{\text{MoSe}_2}$), and the point κ at the K' -valley of WS₂ ($\mathbf{K}'_{\text{WS}_2}$).

We choose to work directly in the exciton space and restrict ourselves to the low-energy physics of moiré excitons, assuming parabolic dispersions $E(\mathbf{k}) = E_X + \hbar^2|\mathbf{k}|^2/(2M_X)$ and $\mathcal{E}(\mathbf{k}') = E_{\text{IX}} + \hbar^2|\mathbf{k}'|^2/(2M_{\text{IX}})$ of the intralayer (X) and interlayer (IX) excitons, respectively. This implies that we can use plane waves as basis vectors, e.g. $|\mathbf{k}\rangle \sim \exp(i\mathbf{k}\mathbf{x})$, where \mathbf{k} and \mathbf{k}' are the center-of-mass wave vectors of X and IX excitons measured from γ and κ , respectively, M_X and M_{IX} are their effective masses, and E_X and E_{IX} are (optical) band gaps averaged over the moiré supercell. This results in the folded moiré exciton bands numbered by the reciprocal vectors \mathbf{g} and presenting the energy dispersions $E(\mathbf{k} + \mathbf{g})$ and $\mathcal{E}(\mathbf{k}' + \mathbf{g})$, respectively.

4.3.2 | Exciton mixing through phenomenological moiré potentials and interlayer coupling

To introduce interactions and define the general moiré Hamiltonian, we introduce two moiré potentials [180, 187, 188] for X and IX excitons:

$$\begin{aligned} V(\mathbf{r}) &= \sum_{j=1}^6 V_j \exp(i\mathbf{b}_j\mathbf{r}), \\ W(\mathbf{r}) &= \sum_{j=1}^6 W_j \exp(i\mathbf{b}_j\mathbf{r}). \end{aligned} \quad (4.12)$$

These are the lowest-order harmonic expansions of the moiré potential which, due to the 120° rotational symmetry, present the usual symmetry relations $V_1 = V_3 = V_5 \equiv V$ and $V_2 = V_4 = V_6 \equiv V^*$ (and analogously for W) [180, 187, 188]. In total, they result in the scattering amplitudes:

$$\begin{aligned} \langle \mathbf{k} + \mathbf{g}' | H_X | \mathbf{k} + \mathbf{g} \rangle_X &= \delta_{\mathbf{g}, \mathbf{g}'} E(\mathbf{k} + \mathbf{g}) + \sum_{j=1}^6 V_j \delta_{\mathbf{g} - \mathbf{g}', \mathbf{b}_j}, \\ \langle \mathbf{k}' + \mathbf{g}' | H_{\text{IX}} | \mathbf{k}' + \mathbf{g} \rangle_{\text{IX}} &= \delta_{\mathbf{g}, \mathbf{g}'} \mathcal{E}(\mathbf{k}' + \mathbf{g}) + \sum_{j=1}^6 W_j \delta_{\mathbf{g} - \mathbf{g}', \mathbf{b}_j}. \end{aligned} \quad (4.13)$$

Notably, V and W do not include resonant interaction terms between X and IX excitons yet, which we introduce explicitly [196] by defining the Hamiltonian as:

$$H = \begin{pmatrix} H_X & T \\ T^* & H_{IX} \end{pmatrix}, \quad (4.14)$$

where the tunneling is described by interlayer hopping elements

$$\langle IX, \mathbf{k}' + \mathbf{g}' | T | X, \mathbf{k} + \mathbf{g} \rangle = \sum_{\eta=0}^2 t \delta_{\mathbf{k}+\mathbf{g}-\mathbf{k}'-\mathbf{g}', C_3^\eta \Delta \mathbf{K}'} \quad (4.15)$$

with the hopping parameter t . We follow the approximation introduced in Refs. [195, 196] and assume the same term t in all mBZs, mediating the hybridization of MoSe₂ excitons X with the closest three IX states in the reciprocal space denoted by the violet arrows in Fig. 4.4a.

Finally, we restrict the number of vectors \mathbf{g} considered in the Hamiltonian and keep only the lowest seven X-bands and six IX-bands arising from band folding of mBZs as specified by the red and blue dots in Fig. 4.4a, respectively. Furthermore, we assume that the non-resonant part of the interlayer potential is zero, $W_{1..6} = 0$, resulting in the 13-band Hamiltonian:

$$H(\mathbf{k}) = \begin{pmatrix} E_0 & V & V^* & V & V^* & V & V^* & t & t & t & 0 & 0 & 0 \\ V^* & E_1 & V & 0 & 0 & 0 & V & 0 & 0 & t & 0 & t & 0 \\ V & V^* & E_2 & V^* & 0 & 0 & 0 & t & 0 & 0 & 0 & t & 0 \\ V^* & 0 & V & E_3 & V & 0 & 0 & t & 0 & 0 & 0 & 0 & t \\ V & 0 & 0 & V^* & E_4 & V^* & 0 & 0 & t & 0 & 0 & 0 & t \\ V^* & 0 & 0 & 0 & V & E_5 & V & 0 & t & 0 & t & 0 & 0 \\ V & V^* & 0 & 0 & 0 & V^* & E_6 & 0 & 0 & t & t & 0 & 0 \\ t^* & 0 & t^* & t^* & 0 & 0 & 0 & \mathcal{E}_0 & 0 & 0 & 0 & 0 & 0 \\ t^* & 0 & 0 & 0 & t^* & t^* & 0 & 0 & \mathcal{E}_1 & 0 & 0 & 0 & 0 \\ t^* & t^* & 0 & 0 & 0 & 0 & t^* & 0 & 0 & \mathcal{E}_2 & 0 & 0 & 0 \\ 0 & 0 & 0 & 0 & 0 & t^* & t^* & 0 & 0 & 0 & \mathcal{E}_3 & 0 & 0 \\ 0 & t^* & t^* & 0 & 0 & 0 & 0 & 0 & 0 & 0 & 0 & \mathcal{E}_4 & 0 \\ 0 & 0 & 0 & t^* & t^* & 0 & 0 & 0 & 0 & 0 & 0 & 0 & \mathcal{E}_5 \end{pmatrix}. \quad (4.16)$$

The first seven diagonal terms correspond to the X bands marked by the red dots in Fig. 4.4a, with

$$E_0(\mathbf{k}) = E(\mathbf{k}), \quad E_j(\mathbf{k}) = E(\mathbf{k} - \mathbf{b}_j),$$

for $j = 1, 2, \dots, 6$; the last six diagonal terms relate to IXs marked by the blue dots in Fig. 4.4a:

$$\mathcal{E}_\eta(\mathbf{k}) = \mathcal{E}(\mathbf{k} - C_3^\eta \Delta \mathbf{K}), \quad \mathcal{E}_\zeta(\mathbf{k}) = \mathcal{E}(\mathbf{k} + 2C_3^{\zeta-3} \Delta \mathbf{K}), \quad (4.17)$$

where $\eta = 0, 1, 2$ and $\zeta = 3, 4, 5$. This Hamiltonian combines the non-resonant intralayer continuum model described by the potential V [180, 187, 188] with the interlayer hybridization described by the hopping parameter t [195, 196], and it can be used to compute the band dispersion within the full mBZ. Here, since we are mainly interested in the optical response of the system, we consider the center of the mBZ at the γ -point. After diagonalization of the Hamiltonian in Eq. (4.16), we obtain the absorption χ'' (cp. Eq. (3.2)) by projecting the eigenstates onto the fundamental A-exciton state as:

$$\chi''(\omega) \approx \chi_0'' \sum_{m=1}^{13} |\langle m|A\rangle|^2 \frac{\gamma_0^2}{\hbar^2(\omega - \omega_m)^2 + \gamma_0^2}, \quad (4.18)$$

where $|A\rangle$ is the MoSe₂ intralayer exciton state corresponding to the first row and column in Eq. (4.16), χ_0'' is its dielectric susceptibility [180], $|m\rangle$ and $\hbar\omega_m$ are the eigenstates and eigenvalues of the m -th exciton band obtained from the diagonalized Hamiltonian in Eq. (4.16), and γ_0 is a peak broadening parameter. Notably, this implies that the oscillator strength of the $|A\rangle$ exciton is redistributed among the set of the moiré excitons $|m\rangle$.

Finally, to describe the behavior of interlayer excitons IX as a function of an out-of-plane electric field, we assume symmetric dielectric hBN layers and define the field as $F = \Delta V_{\text{TB}}/l = (V_B - V_T)/l$, with l being the total distance between the electric gates. Then, we compute the evolution of $\chi''(\omega)$ as a function of ΔV_{TB} by shifting the IX resonance energies in (4.17) as

$$\mathcal{E}(\Delta V_{\text{TB}}) = \mathcal{E} - \frac{ed\Delta V_{\text{TB}}}{\epsilon l}, \quad (4.19)$$

where e is the electron charge, $d = 0.6$ nm the distance between the two TMD layers and $\epsilon \approx 4$ [134] is an effective fit parameter accounting for the interlayer dipole of the IX resonance.

4.3.3 | Limiting cases of the effective model

To illustrate the quantitative impact of the most important fitting parameters, we show the evolution of some computed absorption spectra with the varying parameters θ , $|V|$, $\arg(V)$ and t in Fig. 4.5. Notably, the phenomenological model developed above presents a combination of intralayer exciton mixing mediated by the potential V and interlayer hybridization mediated by the hopping parameter t . Conversely, setting $V = 0$ meV recovers the pure interlayer hybridization model, and setting $t = 0$ meV results in a pure intralayer exciton mixing description.

In Chapter 5, we will present full modeling of the moiré excitons in antiparallel MoSe₂/WS₂ heterostructures. Here, we wish to assess the two limiting cases of the description which we illustrate by considering the two cases of parallel and antiparallel alignment with a different order of the spin-polarized subbands. In Fig. 4.6a, we show the experimental DR signals of two samples with opposite alignment (H and R-type) together with theoretical fits in both limiting

cases of the model. The good agreement between theory and experiment shows that both the $V = 0$ meV and $t = 0$ meV subspaces provide enough descriptive power to model the neutral spectra of both H- and R-type devices. Therefore, full field-dependent experimental data is needed in order to determine the correct contributions to the intra- and interlayer moiré potentials.

We emphasize that in the $V = 0$ meV description, any exciton mixing is mediated through second-order hopping processes and is associated with substantial out-of-plane electric dipoles as shown in Fig. 4.6b. To describe the vanishing electric-field dispersion of the bright excitons as observed in experiment, it is therefore necessary to include the potential V to enable first-order intralayer coupling. The strong avoided crossing of M_3 in the H-type data, on the contrary, requires finite interlayer hybridization. Therefore, to correctly describe all three bright excitons, it is necessary to combine both intralayer coupling and interlayer hybridization, and we will

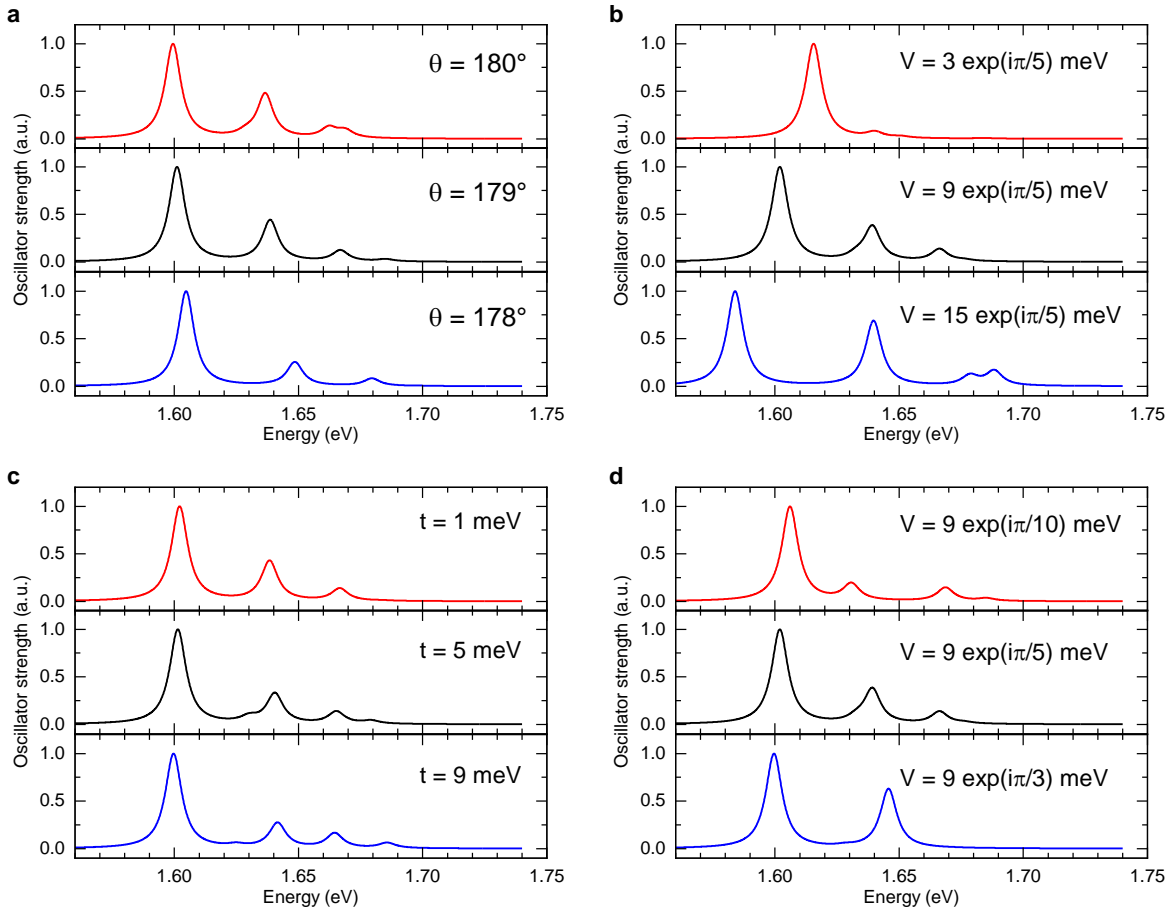


Figure 4.5: Evolution of the computed spectra when all parameters but one are kept constant, with varying θ in (a), $|V|$ in (b), t in (c) and $\arg(V)$ in (d) [17].

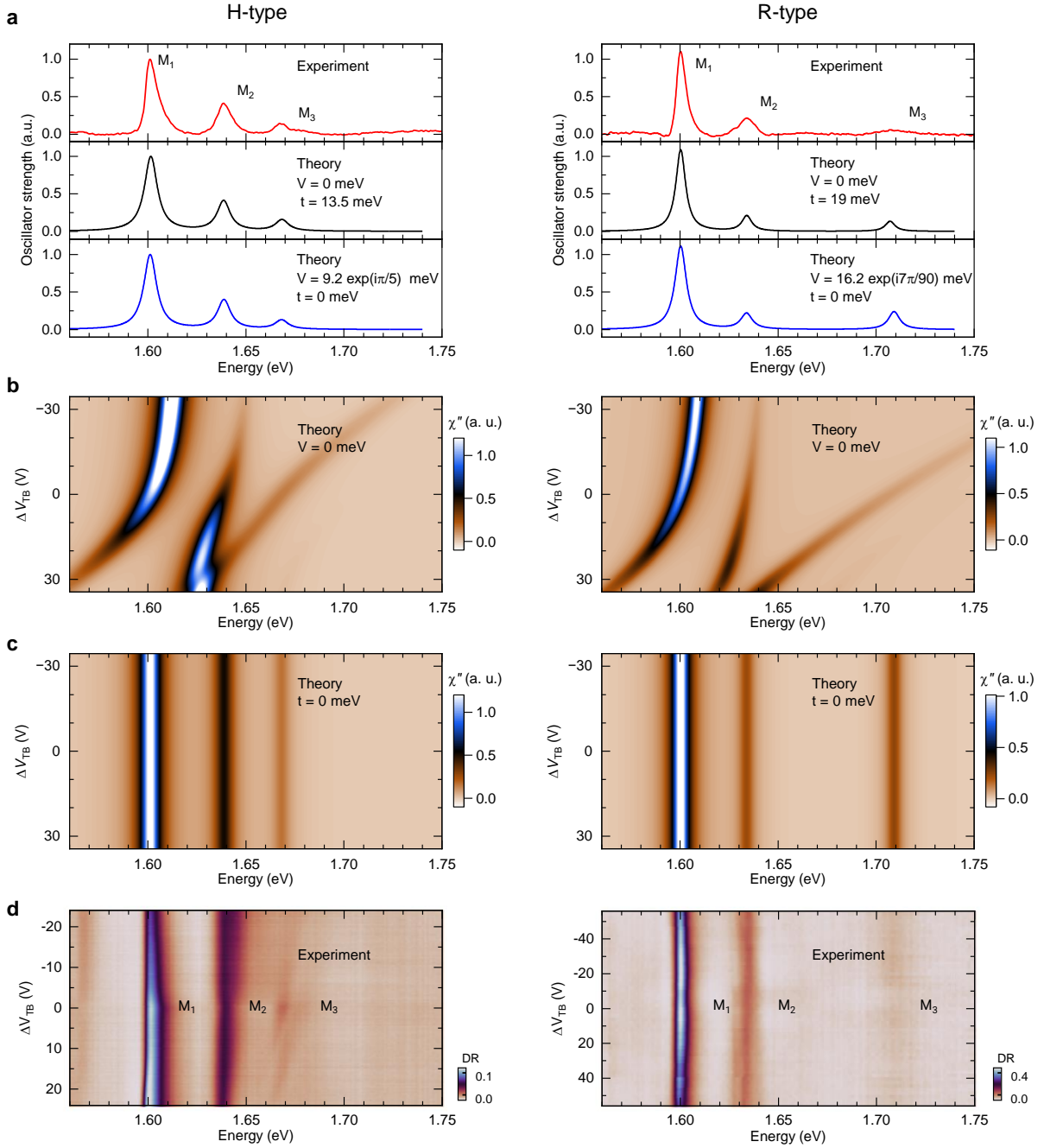


Figure 4.6: Limiting cases of the model with $V = 0$ meV and $t = 0$ meV with a comparison of H-type (left) and R-type data (right). (a) DR spectra with three bright moiré excitons complemented with theoretical fits within the interlayer hybridization ($V = 0$ meV) or the intralayer mixing model ($t = 0$ meV) only. (b) & (c) Calculated dispersions under perpendicularly applied electric fields for $V = 0$ meV and $t = 0$ meV, respectively. (d) Experimental dispersions of the three bright moiré excitons. In both stacking configurations, M_1 and M_2 have no sizable energetic shifts (contrary to the hybridization model), whereas M_3 presents an avoided crossing with a sizable Stark shift in the H-type data (contrary to the $t = 0$ meV calculation) [17].

proceed with the respective discussion in Chapter 5.

4.4 | Charge doping in periodic moiré lattices

For studies of charge doping dependent phenomena in TMD heterostructures, it is important to know the exact charge carrier density for any applied top and bottom gate voltages V_T and V_B . Unfortunately, despite its paramount significance, the state of the educational and scientific literature on the topic remains potentially confusing [200]. The reason for this can be traced back to partially contrasting definitions of what solid-state physicists call the *Fermi energy*. While some classic texts define it as the (zero-temperature) *chemical potential* of a condensed material [201], some of the semiconductor-oriented works often use it to refer to the *electrochemical potential* that combines both the chemical and the electrostatic ones [147]. In metals, where the density of states (DOS) can often be assumed to be quasi-infinite, controlling the charge carrier density can be typically achieved by considering the latter only. In semiconductors and low-dimensional structures, on the other hand, the electrostatic and chemical energy costs can be of the same order of magnitude and require a careful analysis of any problem that involves free charge carriers.

The conflict between the two definitions is nicely illustrated by the idea of band bending in classical semiconductor device engineering [147]. Take for example a pn-junction: while the chemical potential in the p- and the n-doped regions is obviously not the same, the diffusion of minority carriers typically builds up an electric field that leads to a competition between the chemical and electrostatic potentials. In equilibrium, a depletion region emerges in which the drop in electrostatic energy $e\phi$ is exactly balanced by a gain in chemical energy μ , meaning that the electrochemical potential $\eta = \mu - e\phi$ is constant across the junction. The latter fact is often described by the statement of 'constant Fermi energy' that obviously only makes sense if one identifies E_F with η . It is, however, important to keep in mind that neither the chemical (which is measured with respect to a reference point such as the vacuum potential), nor the electrostatic potential are constant. In particular, this last point implies that in general it is wrong to identify the voltage with the electrostatic potential: when measuring the voltage drop between the two sides of a pn-junction, any voltmeter would naturally show a value proportional to the drop in electrochemical potential which is zero.

In the following discussion, we avoid confusion by abandoning the notion of Fermi energy altogether and by sticking to the terms of chemical energy $E = \mu$ and electric fields F . We also emphasize that while the chemical potential is defined as the potential for electrons, an electrostatic potential (and hence a voltage V) is defined as the energy for positive test charges. In terms of the electrochemical potential introduced above, it implies the association $\Delta V =$

$-\Delta\eta$. Here, however, we seek for a comprehensive discussion and we will explicitly state any chemical or electrostatic energy contributions for the charges in our field-effect devices.

The basis for any discussion of capacitor structures is given by the Gauss's law of electrostatics, which in its general form invokes the notion of the displacement field. In the presence of a static dielectric susceptibility, an externally applied electric field \vec{F}_{appl} typically induces a polarization of the medium \vec{P} that implies a total electric field $\vec{F} = \vec{F}_{\text{appl}} - \vec{P}/\epsilon_0$. In linear media, the polarization itself is proportional to the electric field, i.e. $\vec{P} = \epsilon_0\chi\vec{F}$. By noting the relation $\epsilon = 1 + \chi$, the displacement field is then defined as

$$\vec{D} = \epsilon_0\vec{F} + \vec{P} = \epsilon_0\epsilon\vec{F}, \quad (4.20)$$

and obeys the Gauss's law

$$\nabla \cdot \vec{D} = \rho_f \quad \Leftrightarrow \quad \int_{\partial V} \vec{D} \cdot d\vec{A} = Q_{\text{free}}^{\text{in}}. \quad (4.21)$$

Here, ρ_f is the density of free charge carriers (i.e. those that make a material non-neutral), and $Q_{\text{free}}^{\text{in}}$ is the integral over this density contained in the volume V and delimited by the area ∂V .

A classical application of Gauss's law shows that in a conductor, free charges can only be present at the surface, but never inside the bulk. Otherwise, a non-zero electric field \vec{F} would force charges to flow until an equilibrium is reached, and any static equilibrium is necessarily characterized by vanishing fields inside the conductor and hence vanishing bulk charge carriers. Figure 4.7a shows the application of this principle to the case of capacitance structures: when a voltage is applied, the charge in a capacitor is redistributed among its different electrodes, but regardless of the geometry the capacitor as a whole remains always charge-neutral.

In the case of a two-plate device shown in Fig. 4.7b, this implies that the electron density n of one plate is always compensated by an opposite (hole) density $-n$ on the other plate. Here, we assume a metallic top electrode at an externally applied voltage V and a 2D material as the bottom electrode at the ground potential. A positive voltage typically induces positive charge carriers in the top plate and negative charge carriers in the bottom one, so the field $\vec{F} = -F\hat{e}_z$ shows from top to bottom. Applying Gauss's law to a infinitesimally thin area at the surface of the top plate relates the field strength to the carrier density, where a careful consideration of the signs leads to the equation $en = \epsilon_0\epsilon F$.

To relate the field F to the voltage V , we proceed by carefully analyzing the energy costs of moving one electron from the top electrode to the bottom one. The total energy cost is given by the externally applied voltage potential and simply amounts to eV . This total energy itself, however, consists of an electrostatic and a chemical contribution. The former corresponds to the energy cost of moving an electron over a distance d in the presence of the electric field \vec{F} and is given by Fed . The latter, on the other side, is generally given by the difference of the

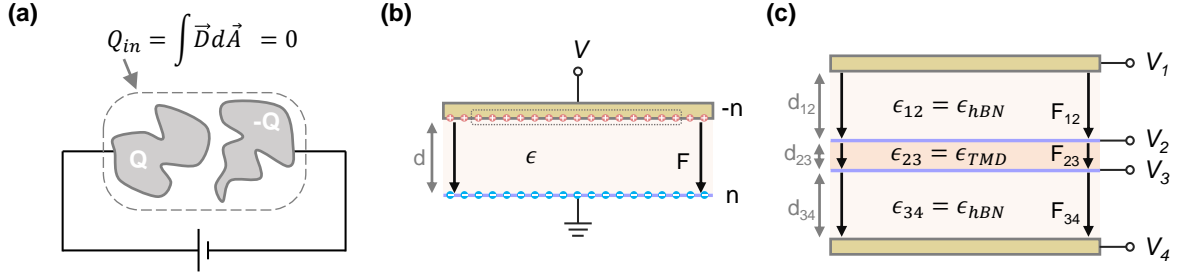


Figure 4.7: **Electrostatics in capacitors.** (a) By virtue of the Gauss theorem, upon charging any capacitance there is no net charge added or removed, but only redistributed between different capacitor surfaces. (b) Illustration of a single-gate device consisting of a metallic plate as the top gate and a 2D material with a finite density of states as the bottom plate. Application of Gauss's law typically includes integration over an infinitesimal volume at the plate surface as depicted by the dashed line. (c) Schematics of a general multi-layer device with several plates at specific voltages and with finite densities of states.

chemical potentials inside the two electrodes and reads as $E(n) - E_T(-n)$. Here, $E(n)$ is the chemical potential of the bottom plate at the electron density n , and similarly for E_T and the top plate. By using a metallic plate as the top gate, however, we can assume a quasi-infinite density of states that implies a constant chemical potential $E_T =: E_0$. Together, this results in the equations

$$en = \epsilon_0 \epsilon F \quad (4.22)$$

$$eV = Fed + E(n) - E_0, \quad (4.23)$$

and defines a general procedure of characterizing parallel plate capacitors with arbitrary chemical potentials $E(n)$.

Now, we illustrate the principle for a more complex, four-plate structure depicted in Fig. 4.7c. At each of the plates, numbered by $i = 1, 2, 3, 4$ from top to bottom, we assume a chemical potential E_i and an externally applied voltage V_i . Furthermore, we assume that all fields point again from top to bottom, so by virtue of Gauss's law we can directly relate the electron density in the second plate to the electric fields by $en_2 = \epsilon_0(\epsilon_{12}F_{12} - \epsilon_{23}F_{23})$. The energy equations, on the other hand, assume the form

$$e(V_1 - V_2) = F_{12}ed_{12} + (E_2 - E_1) \quad (4.24)$$

$$e(V_2 - V_3) = F_{23}ed_{23} + (E_3 - E_2), \quad (4.25)$$

which results in the equation for the electron density

$$en_2 = C_{12} \left(V_1 + \frac{E_1}{e} \right) - (C_{12} + C_{23}) \left(V_2 + \frac{E_2}{e} \right) + C_{23} \left(V_3 + \frac{E_3}{e} \right), \quad (4.26)$$

with the geometric capacitances $C_{ij} = \epsilon_0 \epsilon_{ij} / d_{ij}$ [134, 202–204].

The above relationship (4.26) can be used for any multi-layer device, and in particular for the dual gate field-effect device shown in Fig. 3.2. For the use with a TMD heterostructure, we assume that both TMD layers are at the ground potential (i.e. $V_2 = V_3 = 0$) and encapsulate the TMD dielectric $\epsilon_{\text{TMD}} = \epsilon_{23}$ (with $d_{\text{TMD}} = d_{23}$), whereas the top and bottom dielectrics are both given by hBN ($\epsilon_{12} = \epsilon_{34} = \epsilon_{\text{hBN}}$ with $d_T = d_{12}$ and $d_B = d_{34}$). We denote the top and bottom gate voltages as $V_1 = V_T$ and $V_4 = V_B$ and assume that both top and bottom gates share the same infinite density of states, which allows us to set their chemical potential as the energetic zero and restrict the chemical potentials involved to those of the top and bottom TMD layers, i.e. $E_2 =: E_T$ and $E_3 =: E_B$. Finally, since we are mainly interested in the electronic densities in the TMD layers, we also restrict ourselves to the study of $n_T = n_2$ and $n_B = n_3$. As a result, the total electrostatic equations for the two TMD layers read

$$e \begin{pmatrix} n_T \\ n_B \end{pmatrix} = \begin{pmatrix} C_T & -(C_T + C_{\text{TMD}}) & C_{\text{TMD}} & 0 \\ 0 & C_{\text{TMD}} & -(C_B + C_{\text{TMD}}) & C_B \end{pmatrix} \begin{pmatrix} V_T \\ E_T/e \\ E_B/e \\ V_B \end{pmatrix}, \quad (4.27)$$

with $C_{T(B)} = \epsilon_0 \epsilon_{\text{hBN}} / d_{T(B)}$ being the geometric gate and $C_{\text{TMD}} = \epsilon_0 \epsilon_{\text{TMD}} / d_{\text{TMD}}$ the TMD heterostructure capacitances.

It is important to note that we work with the charge densities being functions of the chemical potential, $n_i(E_i) = \int_0^{E_i} \text{DOS}_i(E') dE'$, with $i = T, B$, rather than $E_i = E_i(n_i)$. This is important, since for regions with $\text{DOS}_i(E) = 0$, n_i will be still a well-defined and continuous function whereas $E_i(n_i)$ will become discontinuous. Moreover, we emphasize that at this level of description, the DOS is explicitly not related to a single particle band structure, since electrons might also exhibit energy costs from mutual Coulomb repulsion and result in peaks of the DOS. We generally assume that charging occurs in steps of the moiré density n_0 , with each step corresponding to a peak in DOS_i . For a given DOS_i , we solve the equations numerically with the `scipy.optimize.root` method for (E_T, E_B) and subsequently evaluate $n_{T(B)}$ at the computed energies.

In Fig. 4.8, we show the computed electron densities ν in a $\text{MoSe}_2/\text{WS}_2$ dual gate device for some particular choices of the densities of states. Here, we assume symmetric hBN dielectrics with $d_T = d_B = 55$ nm such that the total charge density in the HBL is determined by the doping potential $V_\mu = (V_T + V_B)/2$, whereas the electric field is given by $F = (V_B - V_T)/l$, with $l = 110$ nm being the total thickness of hBN layers. We recall that a parabolic energy dispersion in two dimensions gives rise to a constant DOS and results in linear charging behavior of both layers, whereas a non-constant DOS, on the other hand, can result in a non-linear charging behavior of the individual layers. In the same time, we emphasize that the total electron density

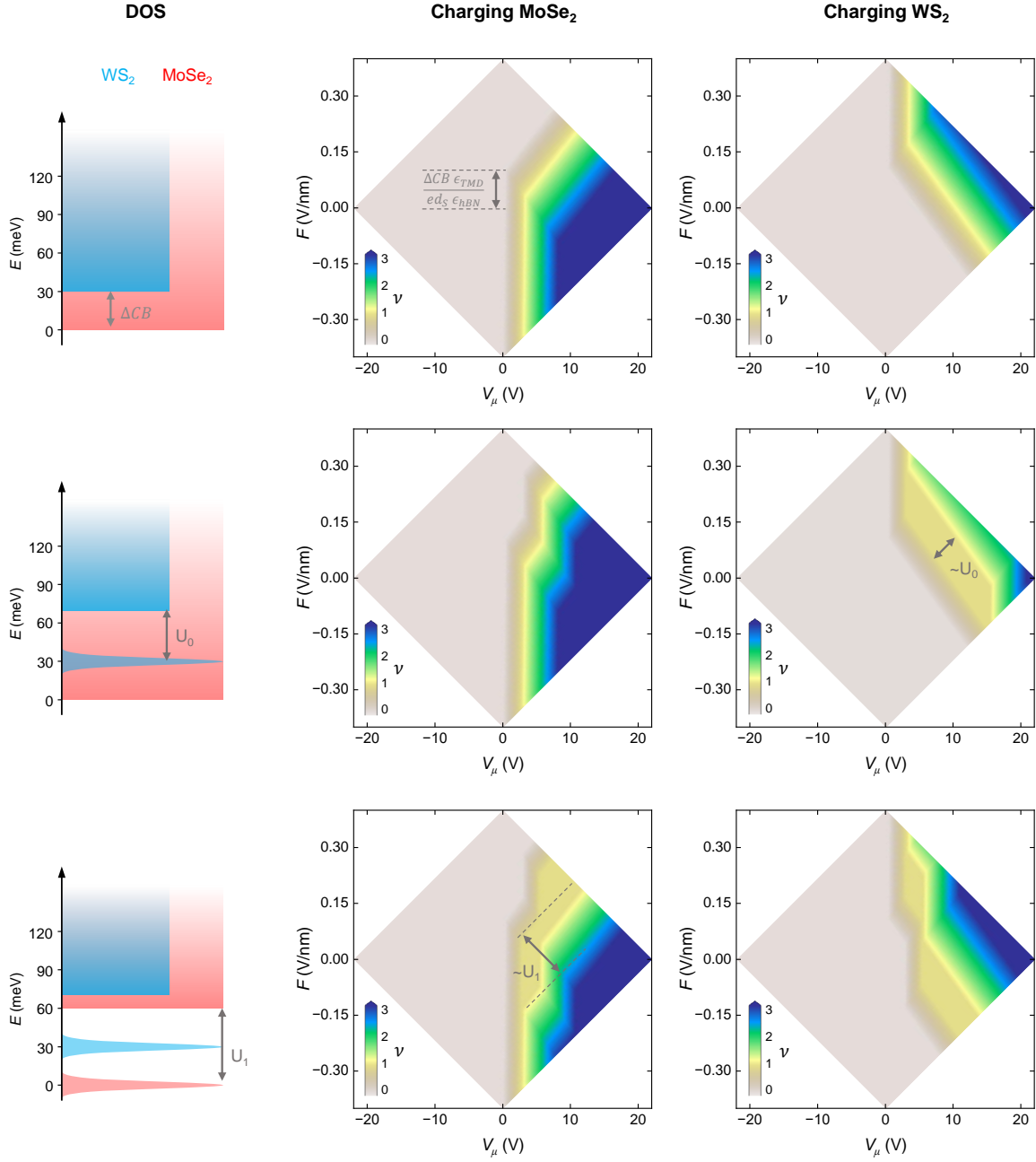


Figure 4.8: **Electrostatic simulations with discretized density of states.** The computed charge distribution among the two layers ($MoSe_2$ and WS_2 in the central and right columns, respectively) shows distinct responses to different parameters in the simulations. The top panel highlights the effect of the conduction band offset ΔCB for otherwise constant DOS (the higher DOS for $MoSe_2$ reflects its higher electron effective mass as compared to WS_2). The middle panel shows the effect of the energy gap in the DOS of WS_2 , entailing step-like charging in WS_2 and kinks in the charge-onset line in $MoSe_2$. The bottom panel emphasizes the effect of gapped subbands in $MoSe_2$, resulting in step-like charging of the $MoSe_2$ layer.

$n = n_T + n_B$ in the heterostructure always follows the equation

$$en = C_T \left(V_T - \frac{E_T}{e} \right) + C_B \left(V_B - \frac{E_B}{e} \right) \approx C_T V_T + C_B V_B, \quad (4.28)$$

and is approximately given by the simple geometric capacitance equation in first order. The reason for this lies in the typical size of the 2D DOS that is sometimes referred to in the context of the so-called *quantum capacitance*. Typically, the applied top and bottom voltages are on the order of a few to tens of V and lead to a change of the chemical potential on the order of a few tens to a few hundreds of meV. This contrast in the electrostatic and chemical energy scales is sometimes characterized by stating that the quantum capacitance is much bigger than the geometric capacitance, i.e. an additional electron leads to a much bigger change in electrostatic potential than in chemical potential. Therefore, the charging behavior shown in Fig. 4.8 is above all characterized by the *distribution* of the total charge among the two layers, whereas the total charge itself does not strongly depend on the microscopic DOS in the two layers.

4.5 | Interaction of excitons and periodic charge lattices

Finally, we note that in a moiré lattice, a peaked DOS typically corresponds to a situation where electrons are tightly localized in the minima of the moiré potential, leading to a periodic array of charges that can implement a correlated spin-charge lattice. Here, we introduce a framework to address the binding energy of localized excitons inside such a periodical array of localized charge carriers (electrons or holes).

Importantly, we consider electrons ordered on two vertically displaced and staggered lattices, and we assume that the exciton is confined in one moiré cell and interacts with the surrounding ordered electrons as illustrated in Fig. 4.9.

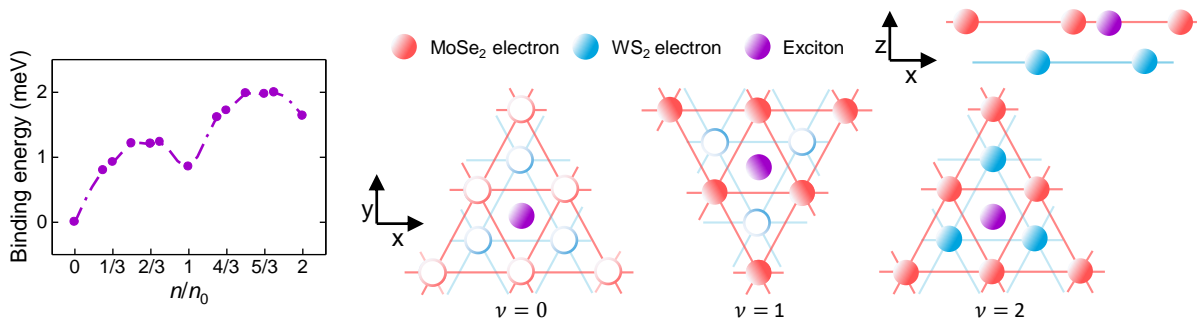


Figure 4.9: Theoretical binding energy of a localized moiré exciton in the presence of an ordered bilayer electron lattice in the process of filling, evaluated as the red-shift from the energy of its neutral counterpart. The right panel shows a schematic of the moiré exciton position and sublattice charge ordering at integer filling factors.

We further assume that the main contribution to the binding energy stems from charge-induced modification of the electron-hole relative motion $\rho \equiv (\rho, \theta) = \mathbf{r}_e - \mathbf{r}_h$, where $\mathbf{r}_{e(h)}$ are the coordinates of the electron and hole forming the exciton. The corresponding Schrödinger equation takes the form

$$-\frac{\hbar^2}{2\mu}\Delta\varphi(\rho) + [V_{\text{RK}}(\rho) + V(\rho)]\varphi(\rho) = E\varphi(\rho), \quad (4.29)$$

where E is the exciton energy, $\mu = m_e m_h / (m_e + m_h)$ is the reduced exciton mass, m_e and m_h are the electron and hole effective masses, and the Rytova–Keldysh potential [75, 106, 107, 205] of the electron-hole attraction is given by:

$$V_{\text{RK}}(\rho) = -\frac{\pi e^2}{2\varepsilon\rho_0} \left[H_0\left(\frac{\rho}{\rho_0}\right) - Y_0\left(\frac{\rho}{\rho_0}\right) \right]. \quad (4.30)$$

Here, e is the electron charge, ρ_0 is the screening length, ε is the effective dielectric constant, and $H_0(x)$ and $Y_0(x)$ are the Struve and Neumann functions.

The interaction of the exciton with the charge lattice is described by the Coulomb sum:

$$V(\rho) = \pm \frac{e^2}{\varepsilon} \sum_{\mathbf{n}} \left[\frac{1}{|\beta_e \rho + \mathbf{n}|} - \frac{1}{|\beta_h \rho - \mathbf{n}|} \right], \quad (4.31)$$

where the plus and minus signs correspond to positive and negative elementary charges, $\beta_e = m_e / (m_e + m_h)$, $\beta_h = m_h / (m_e + m_h)$, and \mathbf{n} are the coordinates of electrons (holes) on the lattice. The two terms in the brackets determine the interaction of the charge lattice with the hole and the electron that constitute the exciton.

To determine the binding energy of the state, we calculate the free exciton energy E_X to obtain

$$E_b = E_X - E. \quad (4.32)$$

To calculate E_X , we set $V(\rho) = 0$, and use in the calculations of both E_X and E the set of 2D hydrogen-like wave functions with the Bohr radius as variational parameter [107, 206, 207] and the basis of six functions [208] with quantum numbers $(n, l) = (1, 0), (2, 0), (2, \pm 1), (4, \pm 3)$ to take into account polarization effects on the exciton relative motion. Due to the lower rotational symmetry of the potential $V(\rho)$, we also include hydrogen-like wave functions with angular momenta $l = \pm 1, \pm 3$. The explicit expression for the trial function is

$$\varphi(\rho, \theta) = e^{-\alpha\rho} + \zeta\rho e^{-\beta\rho} + \eta\rho e^{-\gamma\rho} \cos\theta + \xi\rho^3 e^{-\delta\rho} \cos 3\theta. \quad (4.33)$$

We solve the minimization problem numerically for seven parameters $(\alpha, \beta, \gamma, \delta, \zeta, \eta, \xi)$ using MATLAB R2017B and experimental material parameters of MoSe₂ monolayers [131]: $m_e = 0.84m_0$, $m_h = 0.6m_0$, $\varepsilon = 4.4$, $\rho_0 = 0.89$ nm. The only fitting parameter for comparison between the experimental data and the theoretical model is the moiré superlattice constant, which in Fig. 4.9 is taken to be 7.7 nm.

Moiré physics in MoSe₂/WS₂ heterostructures

In this Chapter, we present our experimental and theoretical results on the moiré physics in angle-aligned MoSe₂/WS₂ heterostructures. Contrary to WS₂/WSe₂ or MoSe₂/WSe₂ heterobilayers, the MoSe₂/WS₂ system did only recently begin to receive interest in the framework of correlated states in moiré flat bands, and instead it raised some controversy regarding its band alignment [14, 15, 190–192, 209, 210]. Notably, *ab initio* calculations predicted a type-II band alignment, with the valence band maximum located at the *K* valley of MoSe₂ and the conduction band minimum in the *K* valley of WS₂ below the CB edge of MoSe₂ [211, 212]. This prediction, however, was revised in recent work in charge-tunable MoSe₂/WS₂ heterostacks [15, 192], suggesting type-I band alignment with the band gap given by that of MoSe₂. Our study confirms this band alignment for twisted heterostacks near both high-symmetry configurations of antiparallel (H) and parallel (R) layer orientation with twist angles close to 180° and 0°, respectively. With experimental access to sub-Kelvin temperatures, ambipolar doping in field-effect devices and out-of-plane electric and magnetic fields, we provide a comprehensive understanding of the bright moiré excitons and the moiré induced ordered electronic states in the studied platform. Our work introduces both new methodology as well as previously unavailable theoretical insight into the low-energy moiré physics in MoSe₂/WS₂ heterostructures. Notably, our experimental access to temperatures on the order of mK allows us to reveal intricate signatures of frustrated magnetism hosted in the flat moiré bands and paves the way for future studies of correlated many-body physics in triangular spin-charge lattices.

In section 5.1, we introduce the samples that present the backbone of this work and show some basic insights from their initial spectroscopic characterization. Section 5.2 deals with the dispersion of the bright moiré excitons in perpendicular electric fields that allows us to model the observed optical transitions in the continuum model framework presented in sec. 4.2. Subsequently, in section 5.3 we focus on the evolution of the bright moiré excitons with charge carrier doping and establish evidence for flat electronic bands that can host a bilayer spin-charge lattice of electrons. Finally, the emergence of stabilized electron order enables detailed stud-

ies of the corresponding magnetic spin-susceptibility that we present in section 5.4. We perform measurements of doping-dependent spin susceptibility that indicate antiferromagnetic exchange interactions and suggest the presence of Ruderman-Kittel-Kasuya-Yosida (RKKY) magnetism above doping levels of one electron per moiré cell. We note that the results of this Chapter have been published partly verbatim in Refs. [17, 18].

5.1 | Sample overview and initial characterization

Over the last four years, we investigated in total five MoSe₂/WS₂ samples with two devices based on CVD-grown TMD monolayers in H-type stacking configuration, one device with CVD-grown monolayers in R-type configuration, and two devices assembled from exfoliated flakes and identified as H-type by their spectroscopic signal. The main conclusions, however, were based on data in three samples that we show in Fig. 5.1 and that are denoted as S1 (CVD H-type), S2 (exfoliated H-type) and S-R (CVD R-type).

Figure 5.2 shows the optical absorption data of the sample S1 in both the MoSe₂ monolayer and the MoSe₂/WS₂ heterobilayer (HBL) regions. In the top panel, the data in the monolayer region shows a very strong absorption peak around the energy of the MoSe₂ A-exciton

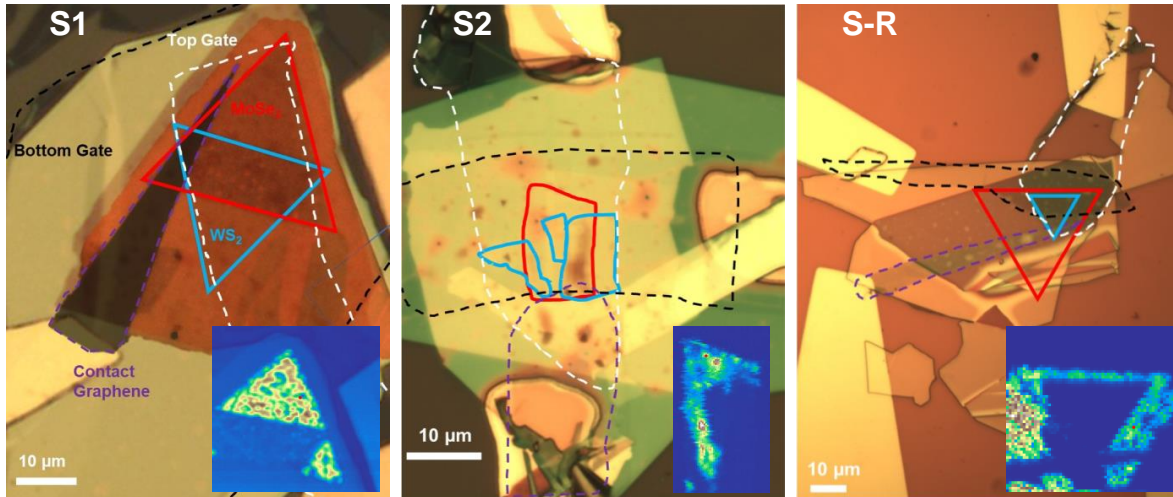


Figure 5.1: Optical images of three studied MoSe₂/WS₂ devices. The left panel shows the CVD-based sample S1 [17], the central panel shows the sample S2 assembled from exfoliated flakes, and the right panel shows the CVD-based R-type sample S-R. The insets show confocal maps of the devices acquired in reflection and visualized around the spectral region of the MoSe₂ monolayer A-exciton.

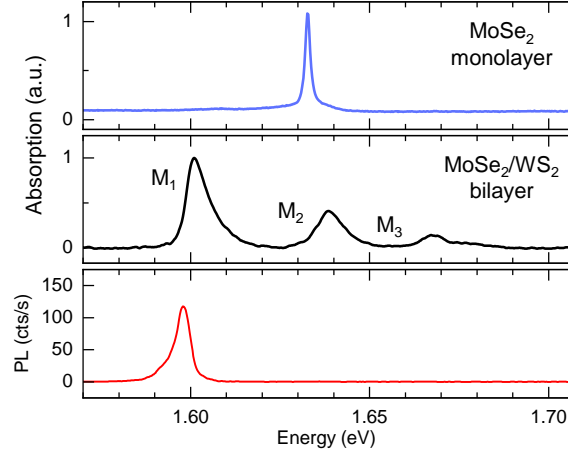


Figure 5.2: From top to bottom: optical absorption of the monolayer MoSe₂ A-exciton in sample S1, optical absorption of the three moiré excitons M_1 , M_2 and M_3 in the bilayer region of the same sample, and photoluminescence at the same spot in the bilayer region. The absorption data were obtained from raw DR signals by applying the shape correction (3.2) [17].

at 1.633 eV and exhibits a linewidth of around 1.6 meV which is comparable to the best samples from exfoliated native crystals. In the central panel, we show the absorption spectrum at charge neutrality with three moiré exciton peaks M_1 , M_2 and M_3 . The peak M_1 at 1.60 eV is approximately 30 meV below the monolayer MoSe₂ A-exciton at 1.63 eV and has the largest oscillator strength. The peaks M_2 and M_3 have decreasing oscillator strengths and lie 38 and 65 meV above M_1 , respectively. Finally, the very bright emission from M_1 in photoluminescence measurements (bottom panel) indicates that it is the excitonic ground state of the system, and the strong quenching of PL from the higher peaks shows fast population relaxation towards the ground state.

Throughout our study, we faced the trend that the optical resonances of the WS₂ layer were strongly suppressed in the MoSe₂/WS₂ heterobilayers. In Fig. 5.3, we illustrate this for the sample S2. The left panel shows an optical photograph of the sample during the stamping process with monolayer flakes delimited by dashed lines. The central panel shows confocal maps of the device acquired around the resonance energies of the MoSe₂ (top) or WS₂ (bottom) bright intralayer excitons. Finally, the right panel shows representative DR spectra obtained from spots both in the MoSe₂ and WS₂ monolayer as well as from the MoSe₂/WS₂ heterobilayer regions. In particular, the bilayer region always exhibits a pronounced signal from the moiré excitons M_1 and M_2 , whereas no resonance in the vicinity of the WS₂ intralayer exciton is observed. This behavior was consistent in all studied samples, implying that insight on the moiré physics in MoSe₂/WS₂ is mainly based on the bright moiré excitons M_1 , M_2 and M_3 .

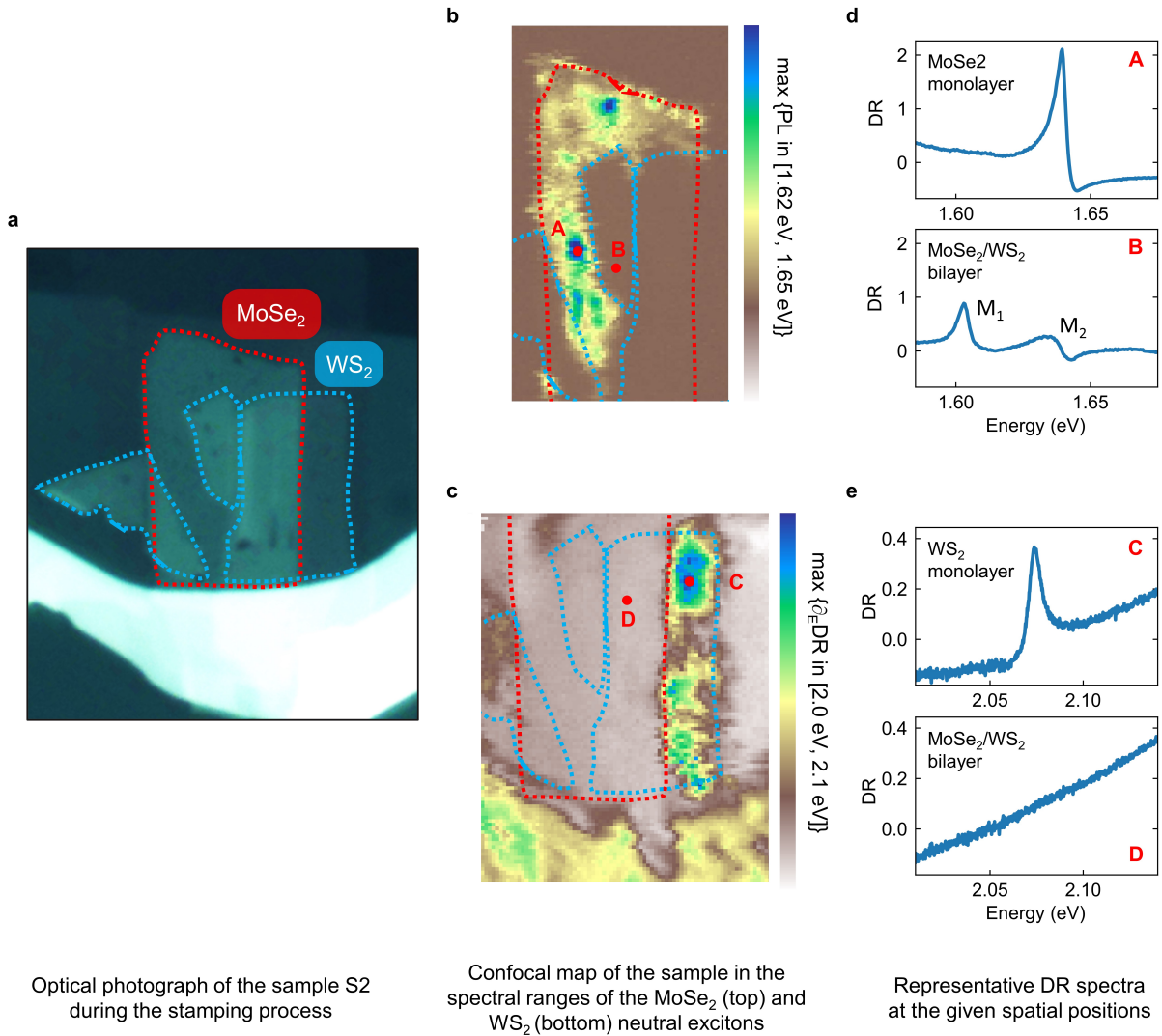


Figure 5.3: (a) Optical photograph of the sample S2 where the red and blue dashed lines delimit the MoSe₂ and WS₂ monolayers, respectively. (b) Hyperspectral map of the sample acquired by projecting the maximum of the PL signal in the spectral range [1.62 eV, 1.65 eV], with the bright areas reproducing the shape of the MoSe₂ monolayer. (c) Hyperspectral map of the sample acquired by projecting the maximum of the derivative of the DR signal in the spectral range [2.0 eV, 2.1 eV], with the bright areas reproducing the shape of the WS₂ monolayer. (d) Representative DR spectra of the MoSe₂ monolayer and MoSe₂/WS₂ heterobilayer in the spectral range of the MoSe₂ intralayer exciton at the positions A and B shown in (b). (e) Representative DR spectra of the WS₂ monolayer and MoSe₂/WS₂ heterobilayer in the spectral range of the WS₂ intralayer exciton. Notably, no WS₂ transition is visible in the heterobilayer region.

In Fig. 5.4a, we show the evolution of DR in monolayer MoSe₂ in sample S1 as a function of the gate voltage $V_G = V_T = V_B$. Notably, the spectra show a transition from the p-doped (holes) through the intrinsic to the n-doped (electrons) regime, with characteristic signatures of the intralayer A-exciton X_A and its attractive (AP) and repulsive polarons (RP). Additionally, the good quality of the sample is reflected by the relatively strong absorption by the intralayer B-exciton X_B at around 1.85 eV. Consistent with the state of the literature, the charged attractive polarons of X_B present a pronounced red-shift with increasing charge carrier density, whereas the attractive polarons of the fundamental X_A exciton exhibit blue-shifts [134].

Figure 5.4b and the top left panel of Fig. 5.5 show the evolution of the differential reflectance (DR) of sample S1 as a function of symmetric gate voltage, $V_G = V_T = V_B$. In the neutral regime from 0.6 to -7.0 V, three bright moiré excitons are observed close to the energy of the MoSe₂ A-exciton. At the boundaries of the neutral region, optical signatures indicate transitions to both the electron (0.6 V) and the hole (-7.0 V) doped regimes. On the p-doped side, the lowest energy exciton M_1 at 1.60 eV exhibits a series of step-like red and blue-shifts before losing its oscillator strength and giving rise to a faint positive trion M_1^+ with 25 meV red-shift, whereas the higher-energy peaks M_2 and M_3 at 1.60 and 1.67 eV, respectively, disappear as soon as charge doping into the valence band sets on. On the n-doped side this behavior is reversed: in a first charging step, M_1 converts abruptly into a negative trion M_1^- with a binding energy of 33 meV, whereas M_2 evolves gradually into a slightly red-shifted peak \tilde{M}_2^- before jumping abruptly to M_2^- in a second charging step. In particular, this second transition at 6.5 V coincides with the emergence of a resonance between M_2 and M_3 which we identify as the charged exciton M_3^- , and with a similarly abrupt quench of the ground state trion M_1^- . Finally, in a third charging step around 13.0 V, both M_2^- and M_3^- red-shift and lose their oscillator strength.

We note that in the samples underlying this work, electric field control worked much better in CVD-grown samples, whereas both of the exfoliated samples presented uncontrolled stray fields that inhibited detailed electrostatic modeling. This is likely caused by the fact that in exfoliated samples, a monolayer flake is often near a bulk region of the TMD. In S2, this is the case for WS₂ as detailed in the Fig. 5.3 above. In CVD-grown flakes, on the contrary, one deals per construction with isolated flakes of a very controlled geometry, such that the overall heterostructure is more controllable in electrostatic terms. Despite the difference in field-control among the studied samples, however, charge carrier doping was much more controllable and produced consistent results throughout different samples. In particular, the distinct signatures in the doping-dependent absorption data can be used to differentiate H-type from R-type samples. From our data on the CVD grown devices shown in Fig. 5.5, it is visible that in the H-type stacking the peak \tilde{M}_2^- is stabilized in an extended voltage range, whereas in R-type stacking it presents a single maximum and a pronounced blue-shift away from this maximum at lower and

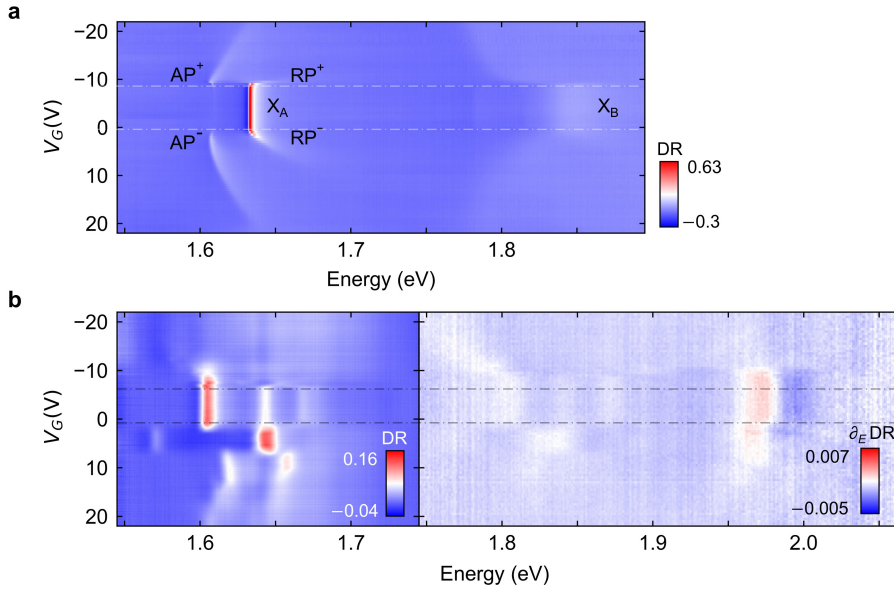


Figure 5.4: Charge doping dependent DR showing ambipolar doping in sample S1. (a) In the monolayer region, changing the gate voltage $V_G = V_T = V_B$ from -22 V to 22 V results in a transition from the hole through the intrinsic to the electron doped regime with characteristic positive and negative attractive (AP) and repulsive polaron (RP) branches. The energy splitting between the negative polaron branches (RP^- and AP^-) of the A-exciton at the onset of electron doping is approximately 28 meV. Additionally, at around 1.85 eV, a faint peak that is interpreted as the B-exciton can be observed. (b) In the spectral region close to the intralayer exciton X_A , the three bright moiré excitons M_1 , M_2 and M_3 show distinct signatures as function of V_G . At approximately 1.80 eV, faint features that are only visible in the derivative of DR and that copy the behavior of M_1 , M_2 and M_3 are interpreted as the B-exciton states of the three moiré excitons. At 1.97 eV, an unidentified faint peak that is likely reminiscent of the MoSe₂ intralayer B2s-exciton disappears at the same onset of hole doping and shows weak red-shift with electron doping. We note that due to bad contacts, the onset of hole doping is strongly dependent on the individual measurement run and coincides in the A and B moiré excitons in data where both signals were acquired within one measurement.

higher gate voltages. Furthermore, complemented by the data from Ref. [16], our data suggests that the peak M_3^- is bright in H-type and dark in R-type stacking. Both features can therefore be used to assign the stacking in the exfoliated devices.

Finally, we gain further insight into the nature of the neutral and charged excitons by probing their response to out-of-plane magnetic fields. In Fig. 5.6, we show the doping-dependent absorption spectra in the heterobilayer regions of samples S1 and S-R for H- and R-configuration, respectively. At a perpendicular magnetic field of -8 T, the neutral excitons M_1 and M_2 in both stackings (with the contrast of M_3 being too low in this set of data) show similar DR signals in

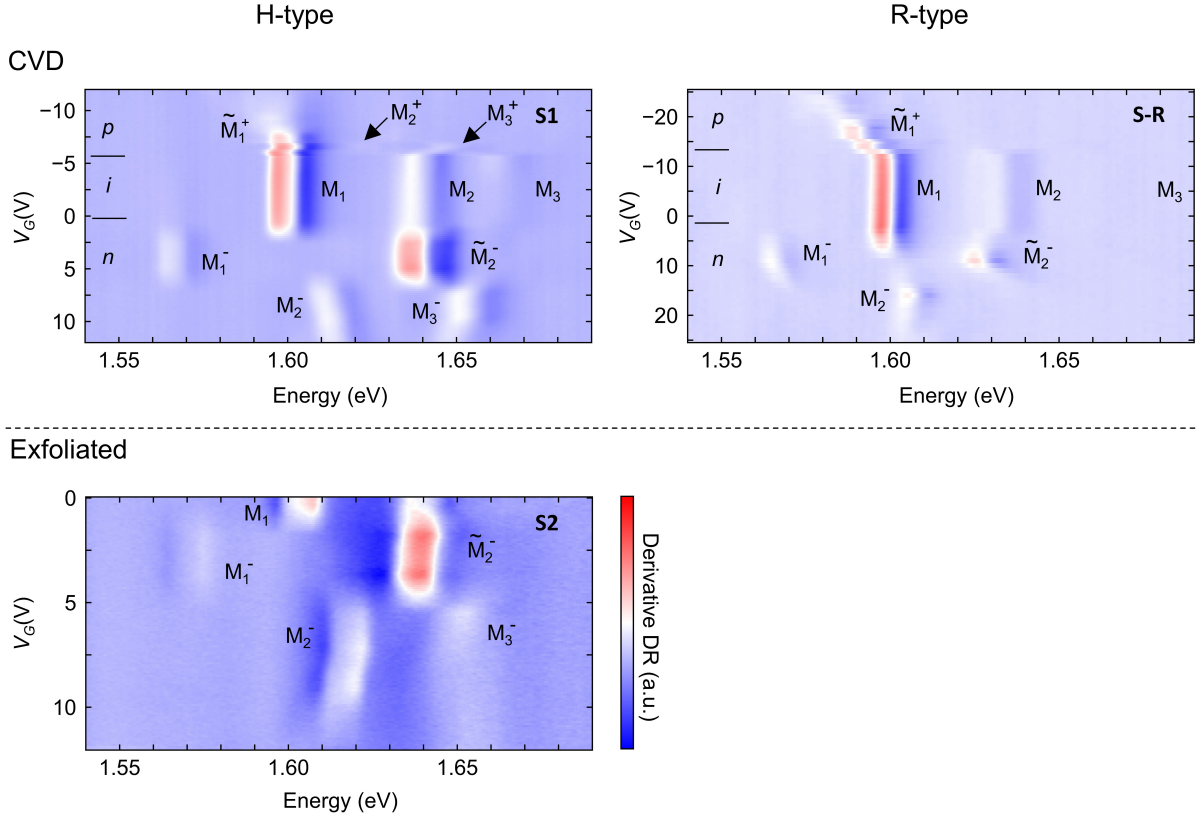


Figure 5.5: Top: charge-doping dependent data in the CVD-based MoSe₂/WS₂ heterobilayers shown in Fig. 5.1. In the H-type stacking (left), the peak \tilde{M}_2^- is stabilized in an extended range of voltages, whereas in R-type stacking (right), it presents a single maximum and pronounced blue-shift away from this maximum at lower and higher gate voltages. Bottom: comparing the doping dependent data of sample S2 with the two CVD-grown samples identifies its stacking regime as H-type.

both σ^+ and σ^- polarizations. Their exciton g-factors, shown in Fig. 5.6c, exhibit values close to the g-factor of the MoSe₂ X_A exciton around $g \approx -4$ and suggest that these moiré excitons arise from mixing of the X_A peak. The peak M_1^- , on the other side, features almost complete valley polarization, just like Fermi polarons in monolayer MoSe₂ [213]. Finally, the peak \tilde{M}_2^- (and similarly \tilde{M}_1^+) is unpolarized and shows a pronounced, doping-dependent Zeeman splitting with nonlinear dependence on the magnetic field.

To illustrate the dispersion of ΔE_Z as function of B , we show representative data on the p-doped, the intrinsic and the n-doped regimes in Fig. 5.7. The top panel shows the evolution of the Zeeman energy splitting of the p-doped peak \tilde{M}_1^+ which acts as a sensor exciton for the emerging hole lattice and shows a strongly renormalized, non-linear g-factor of +30. The central panel shows the corresponding evolution of ΔE_Z for the neutral moiré peak M_1 with the

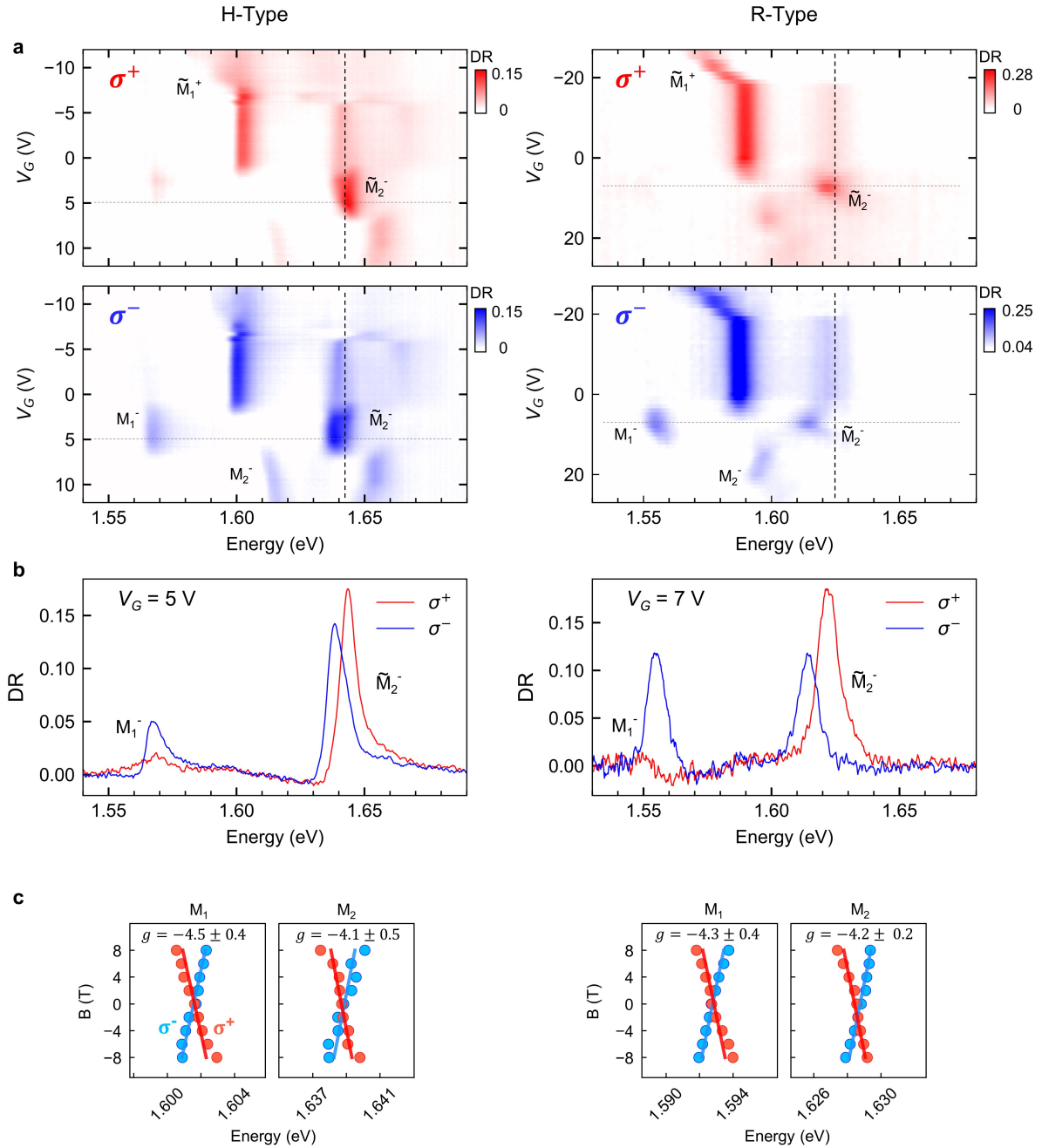


Figure 5.6: Basic magnetic characterization of the MoSe₂/WS₂ heterobilayer in H- and R-type configuration in the samples S1 and S-R, respectively. (a) Doping-dependent DR spectra in σ^+ (top) and σ^- (bottom) polarization at an out-of-plane magnetic field of $B = -8$ T. (b) Line cut of the DR-signal at $V_G = 5$ V (H-type) and $V_G = 7$ V (R-type) showing a polarized negatively charged trion M_1^- and a pronounced Zeeman shift of \tilde{M}_2^- . (c) Evolution of the moiré exciton energies in σ^\pm polarization as a function of the magnetic field. For both brightest peaks M_1 and M_2 , the Landé g-factors show values around the g-factor of the MoSe₂ intralayer A-exciton of around -4.

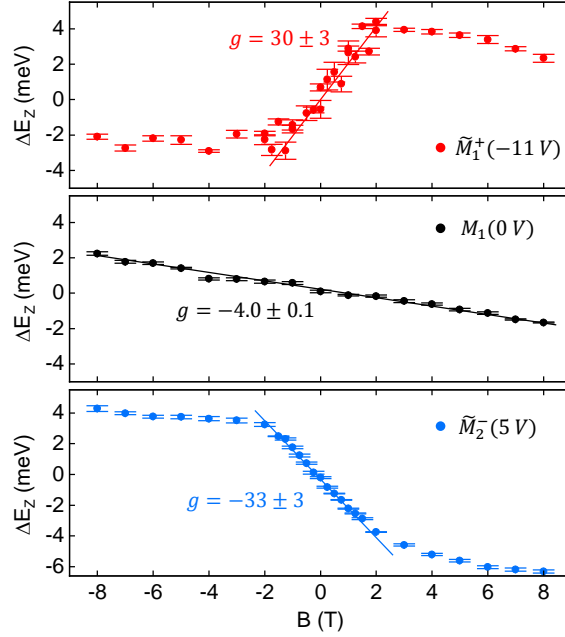


Figure 5.7: Evolution of the valley Zeeman splitting ΔE_Z of the hole-doped peak \tilde{M}_1^+ (top) at $V_G = -11$ V, the neutral moiré peak M_1 (center) and the electron-doped peak \tilde{M}_2^- (bottom) at $V_G = 5$ V in sample S1 at $T = 3.8$ K. The splittings of \tilde{M}_1^+ and \tilde{M}_2^- depend non-linearly on the magnetic field, with a maximum g -factor of 30 ± 3 (\tilde{M}_1^+) and -33 ± 3 (\tilde{M}_2^-), respectively (determined from linear fits for $B \lesssim 2$ T). The non-linear evolution of the Zeeman splittings is indicative of correlation-induced magnetism probed by the respective sensing exciton.

expected linear dispersion and a g -factor of -4 . Finally, the bottom panel shows the Zeeman splittings of the n -doped peak \tilde{M}_2^- which acts as a sensor exciton for the emerging electron lattice and also shows a strongly renormalized, non-linear g -factor of -33 . We note that the magnetic response of \tilde{M}_1^+ and \tilde{M}_2^- are in striking contrast: whereas in the latter case the g -factor is increased into the negative, for the former peak the g -factor changes its sign to positive values, consistent with other studies on hole-mediated spin lattices [13, 214]. This shows that both the hole and the electron doped regimes of MoSe₂/WS₂ present rich physics, and the fact that one heterostructure provides simultaneous access to both electron and hole-doped correlated states makes it standing out in the field.

5.2 | Field-induced hybridization of moiré excitons and the role of band alignment

The dual gate architecture of the studied field-effect devices enables us to control both the out-of-plane electric field as well as the charge carrier density simultaneously. The former allows to shift the electrostatic potential of the MoSe₂ and the WS₂ layer with respect to each other, whereas the latter results in subsequent charge filling of the energetically lowest electronic bands. In this section, we proceed by studying the dispersion of the moiré excitons in the presence of an electric field, before focusing on their behavior under electron doping in the next section. This section falls under the copyright of the American Physical Society (Ref. [17]).

5.2.1 | Modeling of moiré excitons

We already pointed out in section 4.3.3 that different limiting cases of the developed continuum model can yield very similar results in terms of moiré exciton multiplicity and brightness. For this reason, it is important to consider full electric field-dependent data in order to distinguish the intralayer exciton mixing from the interlayer coupling contributions. In Fig. 5.8a, we show the evolution of DR with an out-of-plane electric field proportional to $\Delta V_{\text{TB}} = V_B - V_T$ in the H-type sample S1. As already pointed out in previous studies [15, 192] and shown in Fig. 4.6, the peaks M_1 and M_2 behave as intralayer states with vanishingly small linear slopes of the first-order Stark effect. For these peaks, this implies that they can be captured in terms of the non-resonant moiré potential V , whereas interlayer tunneling plays a negligible role. The peak M_3 , on the contrary, exhibits two branches with finite dispersion indicative of an anticrossing of X and IX states with weak coupling, which necessitates a non-vanishing hopping parameter t in

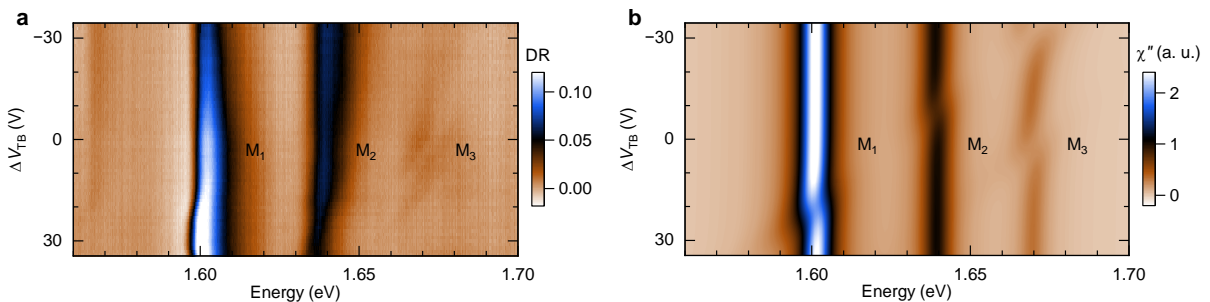


Figure 5.8: (a) Experimental DR signal of MoSe₂/WS₂ in sample S1 as a function of the out-of-plane electric field. (b) Corresponding simulation of $\chi''(\omega)$ capturing the strong intralayer character of the three lowest-energy moiré exciton peaks as well as their relative strengths. Inhomogeneous broadening was included by smoothing $\chi''(\omega)$ over a 5 meV broad Gaussian kernel in the fit parameter E_{IX} [17].

the model. Also, M_1 and M_2 show minor narrowing with a small red-shift at high $\Delta V_{\text{TB}} \geq 18\text{V}$, indicating the presence of dark IX resonances.

By fitting the model to the electric field dependent data, we reproduce the multiplicity and relative oscillator strengths of the three moiré excitons with very good agreement. In Fig. 5.8b, we show the theoretical χ'' obtained for the material parameters $a_{\text{MoSe}_2} = 0.3288\text{ nm}$, $a_{\text{WS}_2} = 0.3154\text{ nm}$, $M_X = 1.44m_0$, and $M_{\text{IX}} = 0.86m_0$ [73, 131] with electron mass m_0 , and with free fitting parameters $E_X = 1617\text{ meV}$, $E_{\text{IX}} = 1614\text{ meV}$, $\theta = 178.8^\circ$, $|V| = 9.3\text{ meV}$, $\arg(V) = \pi/5$, $t = 3\text{ meV}$ and $\gamma_0 = 4\text{ meV}$. We emphasize that although $E_{\text{IX}} < E_X$, the fitting implies a type I heterostructure due to the relation $E_{\text{IX}} > \min[E_X + V(\mathbf{r})] \approx 1566\text{ meV}$, with a CB offset in the order of 50 meV. The remaining fit parameters for a given twist angle ($|V|$, $\arg(V)$, and t) determine the layer character of moiré excitons as well as their energy separations and oscillator strengths. The resulting susceptibility captures the main features of the experimental data such as the relative strengths of the peaks, the strong intralayer character of M_1 and M_2 , the anticrossing of the M_3 doublet and the IX perturbation of M_1 at high positive fields. At the same time, it predicts a weak coupling of M_2 with an IX state at $\Delta V_{\text{TB}} \approx -10\text{ V}$ which can not be observed in white-light DR.

5.2.2 | Interlayer excitons in modulation spectroscopy

To improve the sensitivity to interlayer states we repeated the field-dependent measurement with the modulation-spectroscopy technique introduced in section 3.3.3. In Fig. 5.9a we show $\text{DR}' = R_{\text{ac}}/R_{\text{dc}}$ with signatures of both intra- and interlayer states: the interlayer character of the M_3 doublet becomes much more prominent compared to the white-light DR data, the red-shifts of M_1 and M_2 at high ΔV_{TB} confirm the admixing of IX excitons, and the contrast change of M_2 at $\Delta V_{\text{TB}} \approx -20\text{ V}$ suggests the coupling to a dark IX state made visible with this

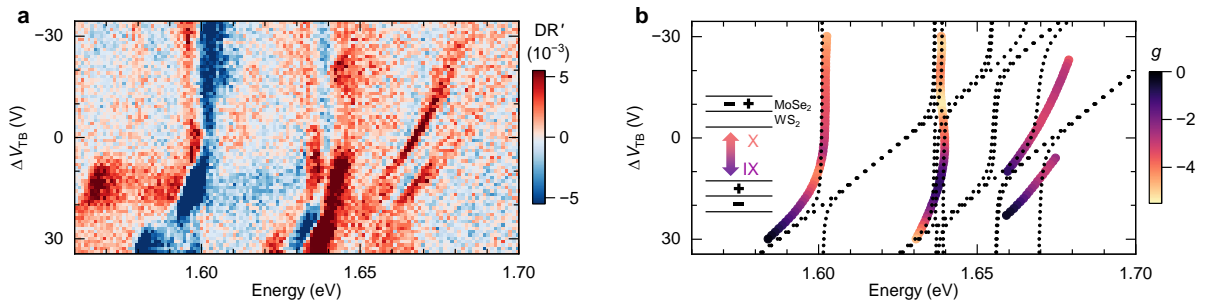


Figure 5.9: (a) Narrow-band modulation spectroscopy signal of MoSe₂/WS₂ in sample S1 as a function of the applied out-of-plane electric field. (b) Dispersion of the eigenvalues of the Hamiltonian in Eq. (4.16) as a function of the electric field and experimental exciton g -factors of the respective resonances color-coded from -5.5 (yellow) to 0 (black) [17].

technique.

In Fig. 5.9b we show the dispersion of the peaks extracted from Fig. 5.9a alongside the evolution of the eigenvalues of the Hamiltonian in Eq. (4.16) as a function of ΔV_{TB} . In contrast to Fig. 5.8b, where the oscillator strengths of the three bright excitons are visible, here the dotted lines indicate the eigenvalues corresponding to all 13 moiré exciton bands irrespective of their oscillator strength. The experimental dispersion of both M_1 and M_2 in Fig. 5.9a is well reproduced, and the strong anticrossing of the M_3 doublet is qualitatively captured within our theoretical model. We note that although the magnitude of the X-IX coupling changes between the M_2 and M_3 resonances, they are both controlled by the same parameter t , and introducing different hopping parameters for different mBZs [192] would allow to improve on the quantitative agreement with the data. Finally, we find that in the neutral regime the first IX state – which is momentum-dark and can not be observed in Fig. 5.8 – lies 30 meV above the ground state M_1 , indicating type I character for the studied MoSe₂/WS₂ heterostack.

Additionally to the electric field dependence we studied the Zeeman effect of moiré excitons by repeating the modulation-spectroscopy measurements for out-of-plane magnetic fields in the range of $B = \pm 6T$. The colors of the data in Fig. 5.9b show the g -factors of the respective peaks for different electric fields, ranging from $g = -5.5$ (yellow) through -2 (purple) to 0 (black). We observe that for electric fields where M_1 and M_2 follow vertical lines of zero Stark effect due to nearly-pure MoSe₂ character, the corresponding g -factors are close to the fundamental MoSe₂ A-exciton with $g_A \approx -4$. Near the IX-X anticrossings, on the contrary, all three states exhibit sizable changes in the g -factors reaching values up to 0. The effect is most pronounced for the dispersive branch of M_1 at high positive electric fields as well as the M_3 doublet, which we attribute to field-induced hybridization with interlayer states. The values of the exciton g -factors depend on both the degree of layer hybridization and the exciton momentum [215, 216], making a full quantitative description of this behavior out of scope for this work. The overall trend, however, is consistent with the intralayer character of the peaks M_1 and M_2 at negative electric fields, and with interlayer admixing near anticrossings captured by our theoretical model.

5.2.3 | Real space distribution of moiré exciton states

Finally, for zero electric and magnetic fields, we illustrate the difference of the three bright moiré excitons by plotting the spatial distributions of their wavefunctions in Fig. 5.10. To compute the real-space distribution of the emerging moiré excitons, we denote the original basis of the Hamiltonian (4.16) by $|j\rangle$ with $j = 0, \dots, 12$, such that it holds, for example, $\langle j|H|j\rangle = E_j$ for $j = 0, \dots, 6$ and $\langle j|H|j\rangle = \mathcal{E}_{j-7}$ for $j = 7, \dots, 12$. Similarly, the Hamiltonian's eigenbasis corresponding to the moiré excitons is denoted by $|m\rangle$.

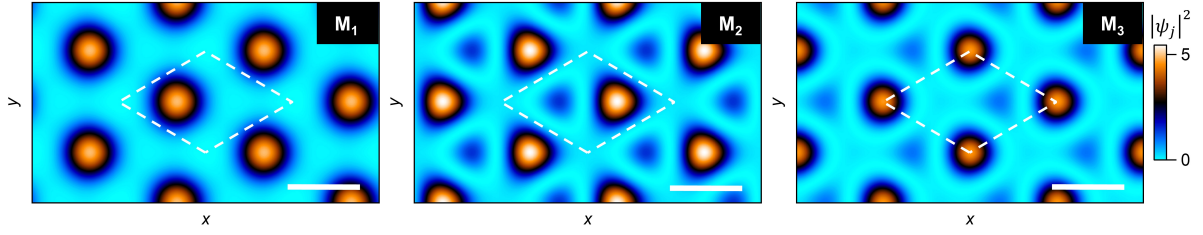


Figure 5.10: Spatial distribution of the exciton wavefunction for the three lowest-energy bright states M_1 , M_2 and M_3 (all scale-bars are 5 nm). All three states are located in different positions of the moiré supercell delimited by the dashed lines [17].

We define $\mathbf{b}_0 = \mathbf{0}$ such that the intralayer states $|j\rangle$, $j = 0, \dots, 6$ correspond to the plane waves $\exp(i\mathbf{b}_j \cdot \mathbf{r})$. Then, the intralayer distribution of the moiré excitons $|m\rangle$ is simply computed by the plane-wave projections of these first seven states, i.e. $\psi_m(\mathbf{r}) = \sum_{j=0}^6 \langle j|m\rangle e^{i\mathbf{b}_j \cdot \mathbf{r}}$. Using this formula for the bright moiré excitons results in the plots in Fig. 5.10.

Remarkably, all three states are located at different points of the moiré supercell and exhibit different spatial distributions: the ground state exciton M_1 is tightly localized, whereas both M_2 and M_3 have non-negligible spatial extents. We note that a detailed modeling of such behavior requires the explicit knowledge of both the electron and the hole potential [193], whereas in our model, the spatial characteristics of moiré excitons are captured entirely through the exciton potential V .

Similarly, we can obtain the interlayer distribution from projections on the six interlayer states, $\tilde{\psi}_m(\mathbf{r}) = \sum_{j=7}^{12} \langle j|m\rangle e^{i\mathbf{b}_j \cdot \mathbf{r}}$, where we define \mathbf{b}_j as the vectors pointing to the blue states defined in Fig. 4.4. Interestingly, comparing the intra- and interlayer distributions helps to provide an intuition on the coupling strengths between intra- and interlayer excitons which we specify for the peaks $M_2(-10\text{V})$ and M_3 in Fig. 5.11. If we plot the overlap of the respective wave functions for each branch as shown in the bottom panel, one easily sees that the overlap for the M_3 doublet is much larger than for the M_2 peak, resulting in the strongest anticrossing as observed in Fig. 5.9.

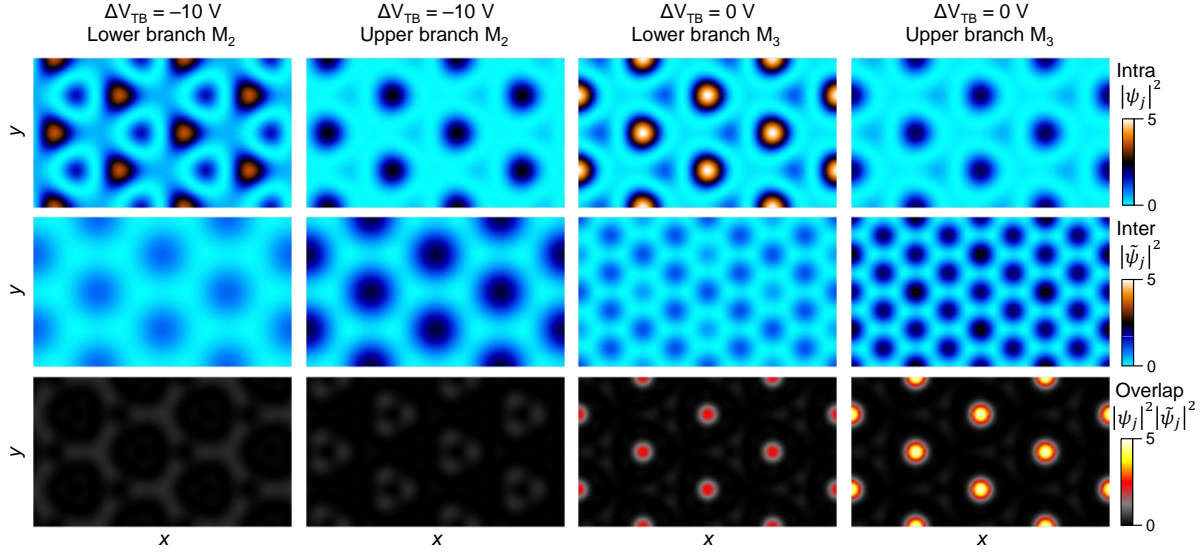


Figure 5.11: The upper and middle panels show spatial distributions of intra- and inter-layer exciton wave functions of the peaks $M_2(-10V)$ and M_3 , respectively. The bottom panel shows their wave functions overlap with the strongest overlap for the M_3 doublet.

5.3 | Charge doping and the role of the moiré potential

In this section, we now turn to the doping diagonal and study the behavior of the bright moiré excitons in the presence of finite charge carrier densities in the H-type samples S1 and S2. Notably, given the challenges associated with good p-type contacts to atomically flat TMD layers [217], we mainly focus our discussion on the electron doped regime with signatures of strongly correlated electronic flat bands. By establishing experimental control of the electron density in these bands, we implement electrostatically stabilized periodic spin-charge lattices across both the MoSe₂ and the WS₂ layers that can be used to study the Fermi-Hubbard model in its strongly coupled $t - J$ limit.

5.3.1 | Exciton localization in the moiré cell and intralayer sensing

In section 5.2, we established different spatial localizations of the three bright moiré excitons inside the moiré unit cell. Looking at the doping dependent DR signals, the contrasting responses of M_1 and M_2 to positive and negative charge doping as illustrated in Figs. 5.4b, 5.6 and 5.12 can be attributed to these distinct spatial positions of the two excitons. The n-doped side is particularly instructive: just as in the case of parallel alignment [16], the charged trion M_1^- indicates that doping-induced electrons are co-localized with M_1 at the moiré potential minima of XX sites [16, 17]. The second exciton M_2 , on the contrary, is located at the MM site,

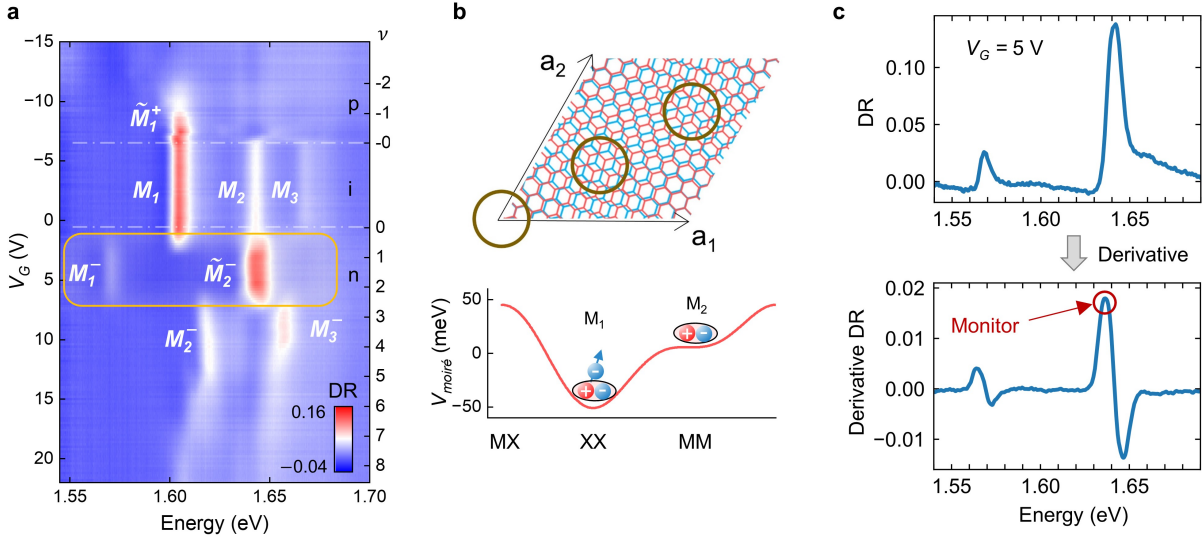


Figure 5.12: (a) Evolution of the DR spectra as a function of symmetrically applied gate voltages for the hole (p), intrinsic (i) and electron (n) doping regimes in sample S1. Neutral excitons M_1 , M_2 and M_3 show different responses to doping, consistent with different spatial localization in the moiré cell. (b) Geometry of the moiré cell (top) with its high-symmetry atomic registries in the case of H-type alignment, and the respective moiré potential $V_{\text{moiré}}$ computed from the continuum model with different localizations of the bright excitons M_1 and M_2 (bottom). (c) DR signal (top) and its derivative (bottom) at the gate voltage $V_G = 5$ V, showing the presence of the charged peaks M_1^- and \tilde{M}_2^- .

which in the limiting case of perfect rotational alignment corresponds to a lateral displacement of ~ 4 nm. This behavior is consistent with previous studies [165, 193] and indicates that, prior to the second doping transition, the exciton \tilde{M}_2^- acts as a remote sensor [185] with binding energy and oscillator strength acting as probes of the surrounding electron lattice.

In the following analysis, we employ \tilde{M}_2^- to obtain insight into doping characteristics at varying electric fields and establish evidence of stabilized spin-charge order in the MoSe₂ layer. To this end, we first study the DR signal in sample S1 as a function of both top and bottom gate voltages V_T and V_B . The charge density in the heterobilayer is determined by the doping potential $V_\mu = (V_T + V_B)/2$, whereas the electric field is given by $F = (V_B - V_T)/l$, with $l = 110$ nm being the total thickness of hBN layers (55 nm each). For aggregated visualization of the hyper-spectral data, we monitor the negative maximum of the derivative $d(\text{DR})/dE$ between 1.603 and 1.800 eV as shown in Fig. 5.12c and plot it in Figs. 5.13 and 5.14a. Notably, extended regions of constant color indicate constant optical response, whereas straight lines and kinks between these regions represent transitions mediated by charging. In particular, the three consecutive electron-doping regions denoted by I, II and III represent the three charging steps of MoSe₂ discussed above as can be seen by their spectral signatures shown in Fig. 5.13.

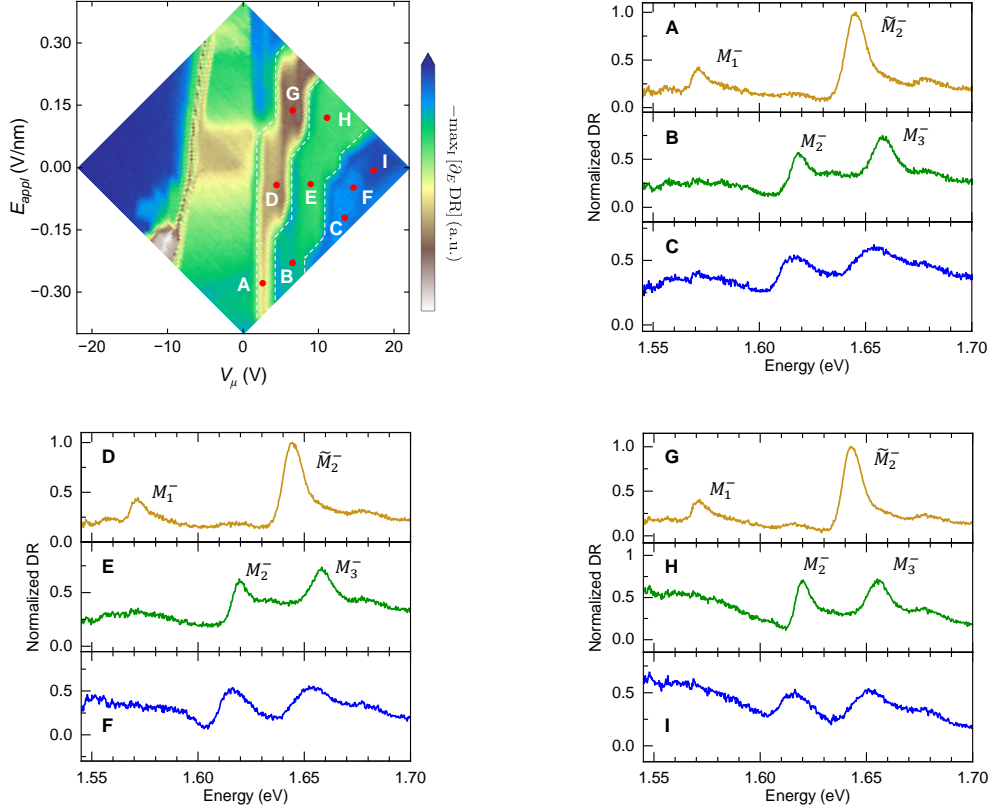


Figure 5.13: Evolution of DR in sample S1 with F and V_μ . We show the DR spectra at nine different points of the charging diagram (A-I) across regions of constant doping as indicated by the color. As obvious from direct comparison, the optical signatures of M_1^- , \tilde{M}_2^- , M_2^- , and M_3^- remain at constant energies for voltages of same doping regimes.

The extent of these three charge-stability regions varies strongly with the applied electric field. In Fig. 5.14b, we show the evolution of M_1 and M_2 with V_μ for three distinct electric fields indicated by the three lines in Fig. 5.14a. For $F = 0.24$ V/nm (right panel), the region I is shifted to higher voltages, with neutral excitons vanishing at ~ 4 V which is half-way through the first charging step at zero-field (central panel). The onset of this shift happens at a field of $F_0 = 0.1$ V/nm, which is consistent with a conduction band (CB) offset of 30 meV between MoSe₂ and WS₂ [17]. Thus, the behavior at fields higher than F_0 is readily explained: in this regime, the CB edge of WS₂ has been tuned below that of MoSe₂ through a crossover from type I to type II band alignment, forcing electrons into the WS₂ layer first. The red-shift of M_1 , observed at ~ 1.0 V in the right panel of Fig. 5.14b, confirms the presence of electrons, and

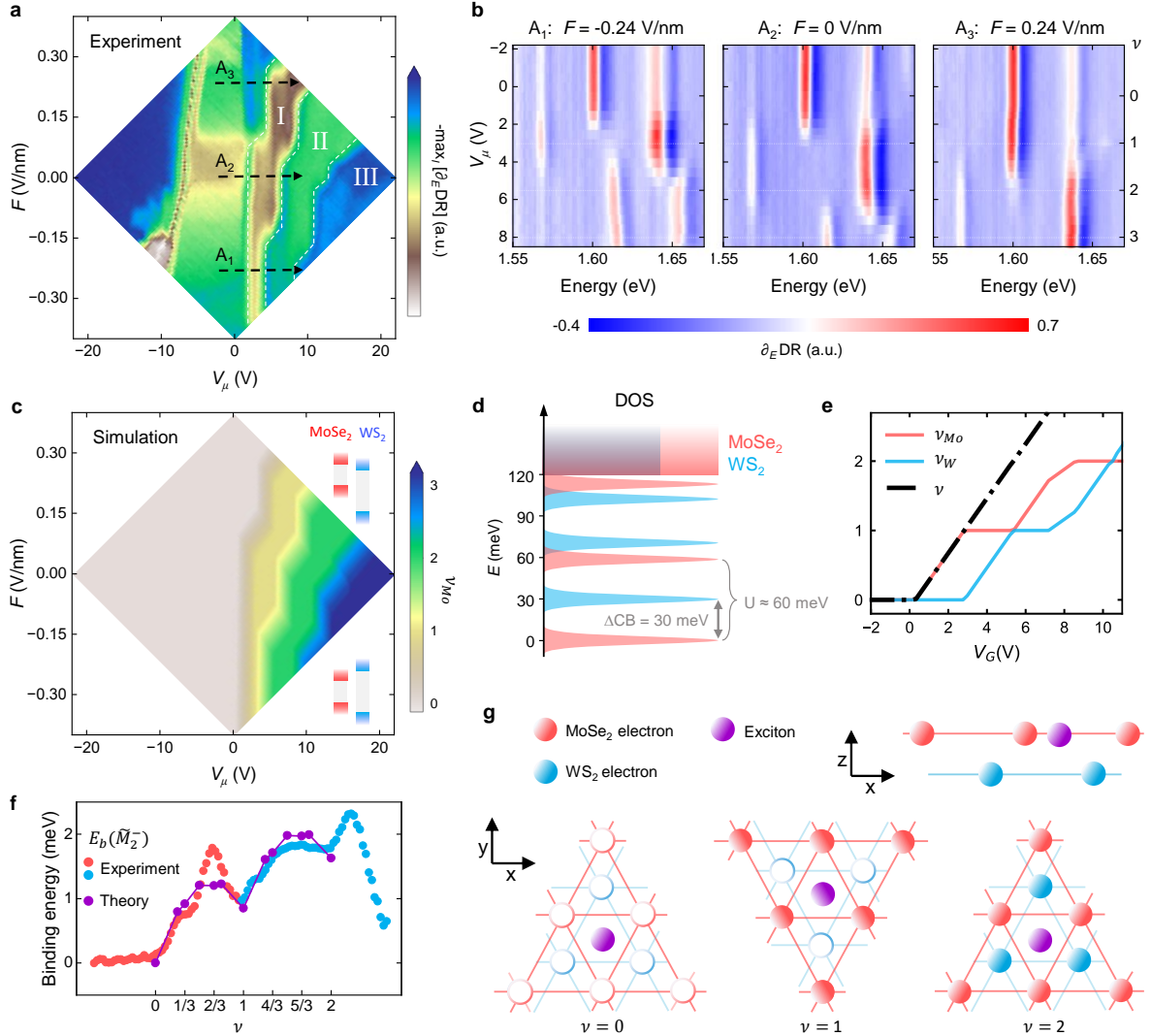


Figure 5.14: (a) Hyperspectral map of the DR signal highlighting the different charging states from the p-doped (left) through the intrinsic (central) to the n-doped (right) regime. The boundaries of the three distinct regions on the n-doped side (I, II and III) signify subsequent charging steps in the MoSe₂ layer. (b) Line-cuts of the data in (a) for representative electric fields showing a crossover from type I at negative and small positive fields (lines A_1 and A_2) to type II band alignment for elevated positive fields (line A_3). Charged excitons \tilde{M}_1^- and \tilde{M}_2^- are present throughout the region I and reflect the charge distribution among the MoSe₂ and WS₂ layers. (c) Simulation of the electron density in the MoSe₂ layer as a function of V_μ and F , reproducing the most pronounced features of electron doping. (d) Schematics of the DOS in both layers obtained from the simulation. Doping of the layers proceeds in steps of n_0 , and the step-like extent of the region I implies Coulomb repulsion of 60 meV between the first and the second electron charging event in the MoSe₂ layer. Together with the CB offset of 30 meV this leads to peculiar charging behavior shown in (e) with charging of the MoSe₂ layer up to one electron per moiré cell and subsequent charge stability upon consecutive filling of the WS₂ layer up to the same filling factor. (f) Experimental and theoretical binding energy of \tilde{M}_2^- , evaluated as the red-shift from the energy of its neutral counterpart M_2 , as a function of the electron filling factor along the line A_2 . (g) Schematics of the moiré exciton position and sublattice charge ordering at integer filling factors.

hence a change of the dielectric environment in the WS₂ layer. The excitons M_1 and M_2 in the MoSe₂ layer [15, 17, 192] are unable to form intralayer charge-bound states until electrons start filling the MoSe₂ sublattice at higher V_μ , and the emergence of M_1^- and \tilde{M}_2^- is shifted to higher voltages accordingly.

For the negative field $F = -0.24$ V/nm (left panel), on the contrary, the onset of electron doping coincides with the zero-field case, but the width of the charging region I with stability of both M_1^- and \tilde{M}_2^- is reduced by half. This behavior is more intriguing, since it indicates that for electric fields pointing from the MoSe₂ to the WS₂ layer, the second charging transition occurs earlier than at zero electric field. From a different perspective, it implies that the number of electrons added to the MoSe₂ layer along the zero-field line is reduced, resulting in an extended charge stability range of region I. Notably, this charging behavior is absent in parallel MoSe₂/WS₂ HBLs, where the moiré potential is deeper and can thus accommodate more electrons within one layer (see Fig. 5.15).

5.3.2 | From moiré to Hubbard: discretization of the density of states by on-site Coulomb repulsion

To explain the observed charging behavior, we apply the capacitance model introduced in section 4.4. Since both the geometric capacitance and the moiré density $n_0 \approx 2.0 \times 10^{12}$ cm⁻² are fixed, the only free degree of freedom pertinent to the charge carrier density is the quantum capacitance, which quantifies the cost of electrochemical energy per charge carrier induced in the HBL, $n(E) = \int_0^E \text{DOS}(E') dE'$. We assume that carrier doping happens in steps of n_0 for both layers, with each step corresponding to a peak in the DOS as shown in Fig. 5.14d. The gaps between these peaks represent energetic cost associated with on-site Coulomb repulsion U due to strong confinement in moiré potential pockets. Thus, subsequent electrons sense a flattened potential upon filling, with resulting Coulomb gaps reaching tens of meV.

To model the charging behavior of the HBL, we adjust the energy of consecutive peaks with finite DOS to recover the same extents for the regions I, II and III as in Fig. 5.14a. Figure 5.14c shows the simulation result on the electron-doped side with very good agreement with experimental data. Remarkably, the simulation implies that region I represents a regime with just one electron per moiré cell in MoSe₂, with excess electrons populating the WS₂ layer instead. Region II, with the presence of the peaks M_2^- and M_3^- , corresponds to two electrons inside MoSe₂, and the region III is characterized by reduced oscillator strength of the slightly red-shifted M_2^- and M_3^- with three and more electrons per moiré cell inside the MoSe₂ layer.

In the simulation, the CB offset between the first DOS peaks in MoSe₂ and WS₂ is fixed to 30 meV by the field F_0 , with an uncertainty of about 10% stemming from uncertainties in the thickness and the dielectric susceptibility of the HBL. The small CB offset confirms the near-

resonant alignment in MoSe₂/WS₂ [14] and allows to tune the effective energetic ordering of the two layers by out-of-plane electric fields. Importantly, to explain the non-uniform width of region I, the Coulomb gap U between the first and second electron charging events in MoSe₂ must be larger than the CB offset. This is at the origin of the difference between parallel and antiparallel MoSe₂/WS₂ HBLs, and for the latter, our calculation predicts $U \approx 60$ meV which leads to the peculiar charging behavior illustrated in Fig. 5.14e and g. At zero field, in a first step, all electrons fill the moiré potential minima inside MoSe₂ until the filling factor of $\nu = n/n_0 = 1$ is reached. In a second step, successive electrons occupy the WS₂ layer while the charge density on the MoSe₂ sublattice remains constant. Only after both layers host one electron per moiré site does the charge carrier doping into the primary MoSe₂ lattice continue. For $F \ll 0$ V/nm, on the contrary, the effective CB offset becomes larger than U , such that the second electron populates the MoSe₂ layer, leading to the continuous transition from region I to region II (cp. the left panel of Fig. 5.14b).

We emphasize that while the electrons fill the WS₂ lattice, the optical response of both M_1^- and \tilde{M}_2^- is only marginally affected. This indicates that the moiré potential minima in WS₂ are located away from both the XX and the MM sites, and implies that the two excitons act as remote sensors of the emerging secondary lattice. To confirm this scenario, we consider \tilde{M}_2^- pinned on the MM site of the moiré unit cell and subjected to Coulomb interactions with electron lattices of varying geometry for different fractional fillings. Using the variational approach introduced in section 4.5, we calculate the change in the exciton binding energy in the presence of the two laterally and vertically displaced charge lattices in MoSe₂ and WS₂ in the process of filling. The quantitative agreement between experiment and theory in Fig. 5.14f is compelling: as the filling factor is increased from zero to two electrons per moiré cell, the binding energy varies from zero up to a maximum of 2 meV, providing an estimate for the energy scale of interactions between excitons and electrons ordered on the surrounding vertically offset and laterally staggered moiré lattices with schematics in Fig. 5.14g.

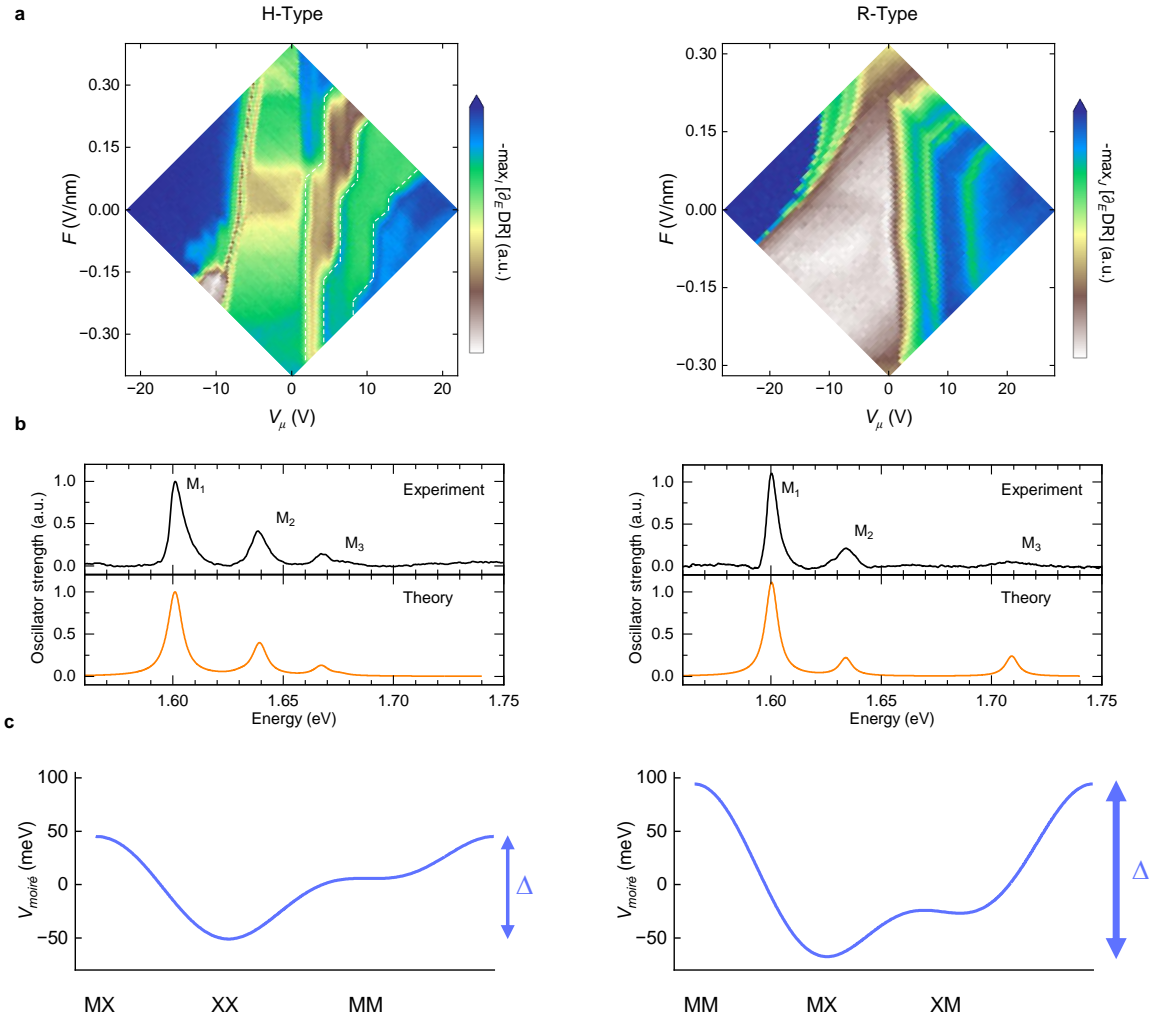


Figure 5.15: Comparison of antiparallel (H-type) and parallel (R-type) MoSe₂/WS₂ charging behavior. (a) Hyper-spectral dual gate DR data for antiparallel (left panel) and parallel (right panel) stackings in the samples S1 and S-R, respectively. The interval J for the visualization of data in the parallel heterostack is between 1.595 and 1.800 eV. Notably, the first charging step into the MoSe₂ layer does not change between negative and small positive electric fields in the parallel stack, signifying that all electrons charge the MoSe₂ layer. We attribute this behavior to a deeper moiré potential in parallel heterostacks, with a rough estimate obtained by fitting the neutral exciton spectra in (b) as detailed in Ref. [17], with peak-to-peak potential amplitudes of 100 and 170 meV shown in (c) for the antiparallel (left panel) and parallel heterostack (right panel).

5.4 | Magneto-optical signatures of bilayer spin-susceptibility

The presence of stabilized electron order in MoSe₂ between $\nu = 1$ and 2 enables detailed studies of the corresponding spin-lattice, with moiré excitons as local probes of magnetization. Previously, isolated bands in TMD moiré structures have been theoretically predicted [188] and experimentally observed [13, 214] to mimic the triangular-lattice Hubbard model, which maps onto the spin Heisenberg model with antiferromagnetic order for strong on-site Coulomb repulsion U and next-neighbor coupling only [188]. Experimentally, spin-spin interactions manifest in diverging magnetic susceptibility which, depending on the optical selection rules, can be probed either by magnetically induced circular dichroism (MCD) [16] or renormalized exciton g -factors [13, 214]. In MoSe₂/WS₂ HBLs, the M_1^- trion is a candidate for the former approach as it inherits the optical selection rules of monolayer MoSe₂ [16, 213], whereas \tilde{M}_2^- shows highly renormalized g -factors consistent with the latter method. In the following, we focus on the effective g -factor of \tilde{M}_2^- as the main probe of spin polarization. We note that the results of this section have been obtained in collaboration with Henning Schlömer, Fabian Grusdt and Annabelle Bohrdt and published verbatim in Ref. [18].

Here, we study the sample S2 that was mounted in the dilution refrigerator. To ensure the applicability of the charging behavior described above, we show a direct comparison of the doping behavior in the samples S1 and S2 in Fig. 5.16. Notably, the extended stability range of the peak \tilde{M}_2^- confirms that both samples share the distinctive layer-by-layer electron doping sequence. Figure 5.17a shows the temperature-dependent Zeeman splitting $\Delta E_Z = E^+ - E^-$ between the \tilde{M}_2^- peaks with σ^+ and σ^- polarization for a range of discrete temperatures between 0.1 and 28 K at the filling factor $\nu = 1$ in sample S2. Analogous to hole-mediated magnetism in WS₂/WSe₂ [13] or MoSe₂/WSe₂ [214], the evolution of ΔE_Z with magnetic field is highly nonlinear, with maximum slopes proportional to the effective g -factor with absolute values $|g|$ exceeding 600 at the lowest temperature. A Curie-Weiss fit to the temperature-dependence of $|g|$ in the bottom left inset of Fig. 5.17a confirms the paramagnetic response of the underlying spin lattice. Notably, the fit yields a negative Curie temperature $\theta = -40 \pm 15$ mK, which is consistent with weak antiferromagnetic interactions. The top right inset of Fig. 5.17a shows the Zeeman splitting as a function of the rescaled field B/T , and the scaling collapse confirms that the degree of spin-polarization is limited by the thermal energy scale only.

The evolution of the g -factor upon electron doping within the stability range of \tilde{M}_2^- (i.e. between $\nu = 0$ and 2.5) is shown in the upper panel of Fig. 5.17b. For all temperatures, the absolute g -factor values rise quickly around the filling factor of 0.5 until they reach their maximum at $\nu = 1$. Remarkably, and in contrast to other heterostructures [13, 214], $|g|$ remains at high values as long as the peak \tilde{M}_2^- is present. This is consistent with the understanding developed above: the MoSe₂ electron sublattice is locked in a Mott insulating state during suc-

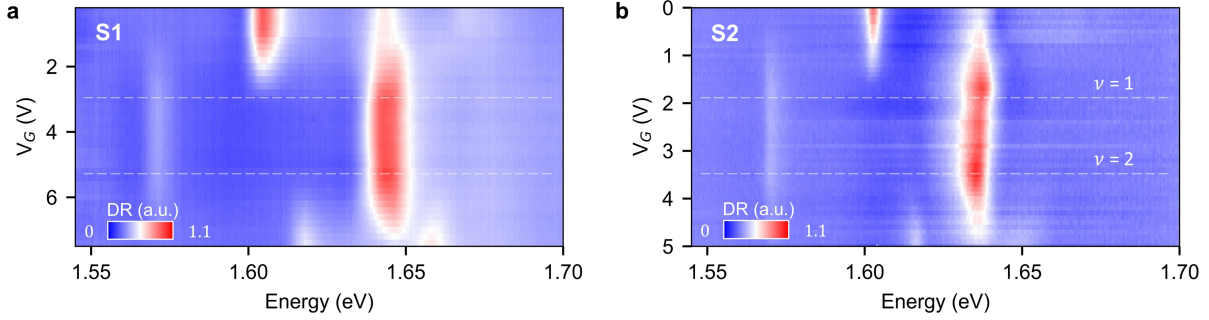


Figure 5.16: Direct comparison of charging in samples S1 and S2. Evolution of normalized DR across the first charging step. Both samples feature the same charging behavior, with peaks M_1^- and M_2^- throughout extended ranges of voltages. Sample S2 (assembled from exfoliated native crystals) exhibits a narrower linewidth than sample S1 (assembled from monolayers synthesized by chemical vapor deposition).

cessive charging of the WS₂ layer ($1 < \nu < 2$). Throughout the plateau, the g -factor values exhibit variations on the order of 10 – 15% due to emergent filling of the secondary lattice. The corresponding variations are also pronounced in the Curie temperature θ , determined from the respective Curie-Weiss fits to the data as a function of the filling factor and shown in the lower panel of Fig. 5.17b. Akin to g -factors, θ exhibits variations across the range $1 < \nu < 2$ with two distinct maxima around $\nu = 1$ and ~ 1.8 . Since negative Curie temperatures are associated with antiferromagnetic (AFM) ordering, an increase in θ towards zero indicates a weakening of AFM interactions within doping regimes highlighted in grey in the bottom panel of Fig. 5.17b.

To understand this behavior, we first focus on the g -factors at integer filling and plot the difference $\Delta|g| = |g|(\nu = 1) - |g|(\nu = 2)$ in the top panel of Fig. 5.17c as a function of the temperature. Obviously, the g -factor of the bilayer lattice ($\nu = 2$) is always below the value of the singular lattice ($\nu = 1$) throughout the experimental temperature range. This can be understood qualitatively by invoking classical Heisenberg models on the corresponding mono- and bilayer lattices and computing the magnetic susceptibility χ_S by Markov chain Monte Carlo methods (MCMC) [18]. The difference in magnetization $\Delta\chi_S = \chi_S(\nu = 1) - \chi_S(\nu = 2)$ computed for $J^\perp/J^\parallel = 1$, shown in the bottom top panel of Fig. 5.17c, confirms the experimentally observed trend. This aligns with the intuition of the magnetic structure in the bilayer Hubbard model: coupling two singular triangular lattices in antiferromagnetically ordered 120° state by finite interlayer coupling J^\perp results in enhanced frustration between the magnetic moments, canting the lattice-ordered spins out-of-plane. This in turn suppresses correlations within each layer, which results in a reduction of the susceptibility as compared to the case of a singular filled spin lattice. This qualitative correspondence between the classical spin model and the observed phenomenology of g -factors at integer fillings $\nu = 1$ and 2 suggests a non-vanishing

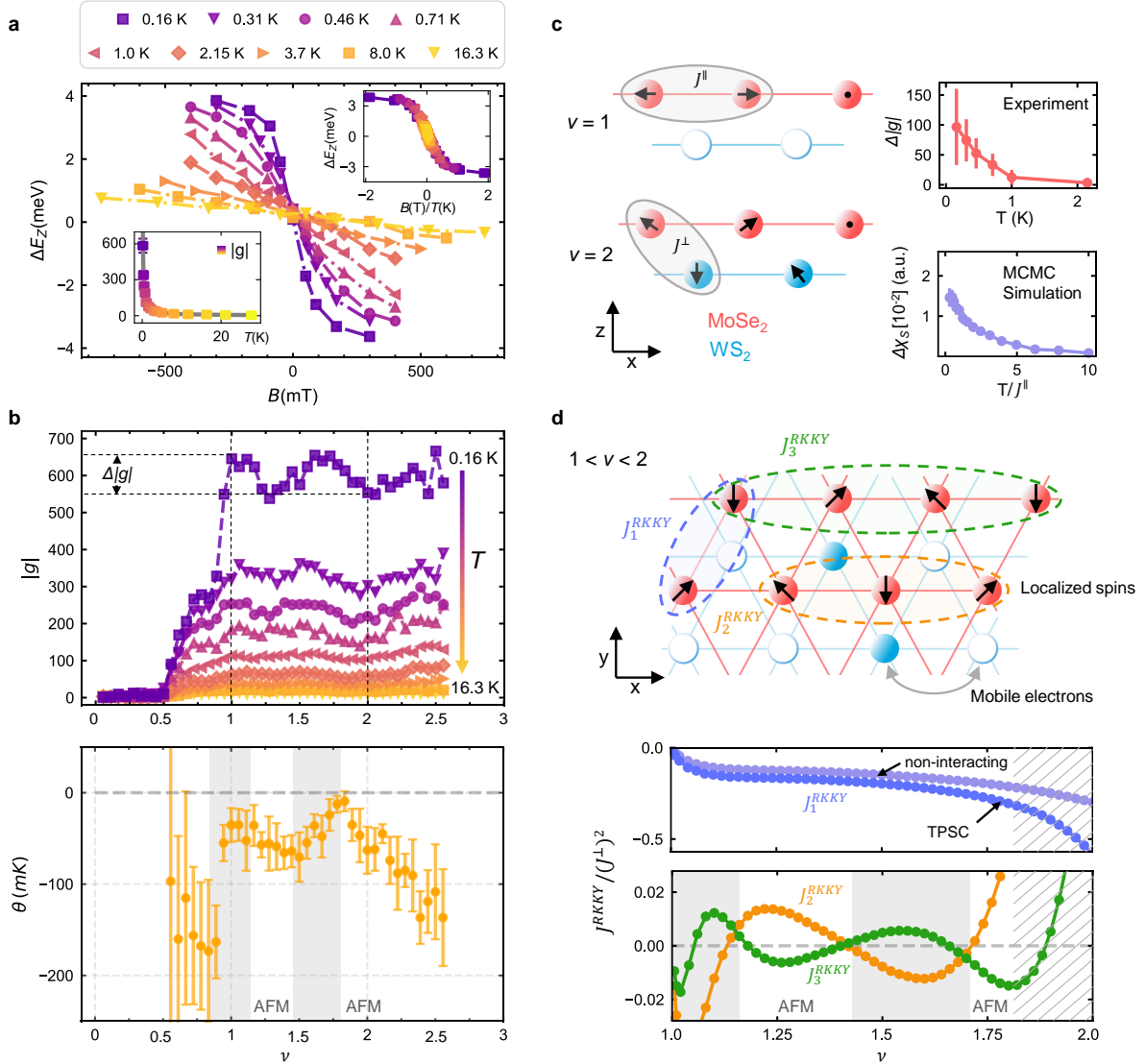


Figure 5.17: (a) Zeeman splittings of the \tilde{M}_2^- peak in σ^+ and σ^- polarization for temperatures between 0.16 and 16.3 K. Right inset: same data as a function of the rescaled field B/T ; left inset: Curie-Weiss fit (solid line) to the temperature-dependence of g -factors. (b) Top: Magnitude of the g -factors as function of the filling factor at different temperatures (top) with highlighted difference in g -factors at integer fillings $\nu = 1$ and 2 . Bottom: Curie-Weiss temperature θ extracted from fits to the data in (a). (c) Left: Schematics of spin sublattices at integer fillings $\nu = 1$ and 2 with intralattice and interlattice exchange coupling J^{\parallel} and J^{\perp} . Right: Temperature dependence of $\Delta|g|$ (top) and difference of the respective magnetic susceptibility $\Delta\chi_S$ in MCMC simulations (bottom). (d) Upper panel: Top-view schematic of the bilayer lattice for integer fillings $\nu = 1$ and 2 , with antiferromagnetic spin-exchange between rigidly locked Mott insulating electrons in the MoSe₂ layer (with interactions among the first, second and third nearest neighbors J_1^{RKKY} , J_2^{RKKY} and J_3^{RKKY}) and mobile electrons in the WS₂ layer. Central panel: Results for nearest-neighbor RKKY interactions in the MoSe₂ layer at filling fractions $\nu > 1$ from simulations of non-interacting fermions (light blue) and TPSC (dark blue). Lower panel: Longer-range RKKY interactions can act against (or in favor of) the 120° state depending on the filling factor as highlighted by the grey (white) areas. Close to the Mott insulating regime $\nu = 2$ (hatched area), the perturbative approach breaks down and other effects such as kinetic magnetism are likely to dominate.

antiferromagnetic interlayer coupling J^\perp and supports the view that the system is governed by bilayer Fermi-Hubbard physics [218].

Now we examine the regime $1 < \nu < 2$, where the primary MoSe₂ layer is locked in a Mott insulating state while the WS₂ layer fills up. For low doping of the secondary lattice, the system can be described by a weakly interacting Fermi liquid coupled to local moments in a Mott insulator. As illustrated in the schematics of Fig. 5.17c and d, finite interlayer coupling J^\perp introduces interactions between mobile electrons on the WS₂ sublattice and localized spins in the MoSe₂ lattice, leading to emergent RKKY-type intralayer interactions J^{RKKY} [219, 220]. We approximate the strength of RKKY interactions by assuming free fermions in the WS₂ layer and employing the two-particle self-consistent (TPSC) approach [221, 222]. The central panel of Fig. 5.17d shows the corresponding ferromagnetic RKKY corrections J_1^{RKKY} to the nearest-neighbor intralayer interactions J_1^\parallel (with effective nearest-neighbor intralayer interactions on the MoSe₂ sublattice $J_1^\parallel + J_1^{\text{RKKY}} < J_1^\parallel$). For low doping above unity filling of the primary sublattice ($\nu \gtrsim 1$), a rapid drop of J_1^{RKKY} is observed (central panel of Fig. 5.17d), which tends to increase the Curie temperature around $\nu = 1$ (bottom panel of Fig. 5.17b). This is also consistent with the initial drop of the g -factor value for $\nu \gtrsim 1$: reduced interactions increase the effective spin temperature in the MoSe₂ sublattice, which results in reduced susceptibility.

As doping proceeds ($\nu \gtrsim 1.5$), nearest-neighbor interactions are further renormalized, resulting in a second rise in the Curie temperature towards zero in Fig. 5.17b. The results of the free fermion and TPSC calculations in the central panel of Fig. 5.17d indicate that interactions in the WS₂ layer enhance this effect. In experiments between $1 < \nu \lesssim 1.8$, the Curie temperature exhibits a minimum at $\nu \approx 1.4$, not anticipated from simple nearest-neighbor RKKY interactions. A possible origin for this behavior is provided by longer-range RKKY couplings, shown in the lower panel of Fig. 5.17d for straight second- and third-nearest neighbors interactions J_2^{RKKY} and J_3^{RKKY} . Indeed, these higher-order effects show distinct oscillations that can act in favor or against the 120° AFM order: positive (negative) second- (third-) neighbor interactions act in favor of the 120° state and imply a decrease in the Curie temperature θ , whereas a reversed sign inhibits the 120° order as in doping regions highlighted by grey shaded areas in Fig. 5.17b and d. Away from these doping regimes (as for $1.15 \lesssim \nu \lesssim 1.45$), AFM order is supported, as signified by reduced Curie temperatures in Fig. 5.17b.

Close to the regime $\nu \lesssim 2$ (grey hatched area in Fig. 5.17d), the Fermi liquid picture of the WS₂ layer breaks down and a bilayer Mott insulator forms, implying that other effects of strongly-correlated origin likely take over. In particular, slight underdoping of a Mott insulator on a triangular lattice is known to result in kinetic effects of Haerter-Shastry type antiferromagnetism, which strongly favors the formation of a classical 120° state to minimize the kinetic energy of the vacancies [223–226]. Such kinetic effects could explain the rise in θ above doping $\nu \approx 1.8$ until $\nu = 2$ in Fig. 5.17b, overcompensating the effect of RKKY interactions. This would

align with the behavior of g -factors at $\nu = 2 - \epsilon$, close to the bilayer Mott insulator, where kinetic magnetism is expected to support AFM correlations and thus enhance the susceptibility. Kinetic magnetism in the regime at $\nu = 1 - \epsilon$ could be also responsible for the sub-plateau on the rising flank of the g -factor values in Fig. 5.17b for fillings between 0.7 and 0.9 at $T = 0.16$ K, which vanishes at higher temperatures. First, around $\nu = 0.75$, the electrons in the MoSe₂ layer become increasingly frustrated, leading to an initial saturation of the g -factor. However, for $\nu \gtrsim 0.9$, the release of kinetic frustration via Haerter-Shastry type AFM interactions would promote the g -factors to significantly higher values.

Finally, we close this section by showing the corresponding data on the spin-susceptibility acquired from the magnetic circular dichroism (MCD) of M_1^- . Similar to the g -factors of \tilde{M}_2^- , the peak M_1^- exhibits highly renormalized MCD that shows polarization values above 80% at the lowest temperatures. Just as above, the derivative of MCD with respect to the magnetic field B is a measure of the local spin-susceptibility and follows the Curie-Weiss scaling behavior with negative Curie temperatures θ , indicating weak antiferromagnetic order. Notably, the evolution of θ as function of the charge carrier density shows modulations similar to those in Fig. 5.17b. The low oscillator strength of M_1^- , however, implies that in the case of MCD measurements the signal-to-noise ratio is much lower. For this reason, we decided to focus on the peak \tilde{M}_2^- as our main sensor of magnetization and use the peak M_1^- for consistency checks.

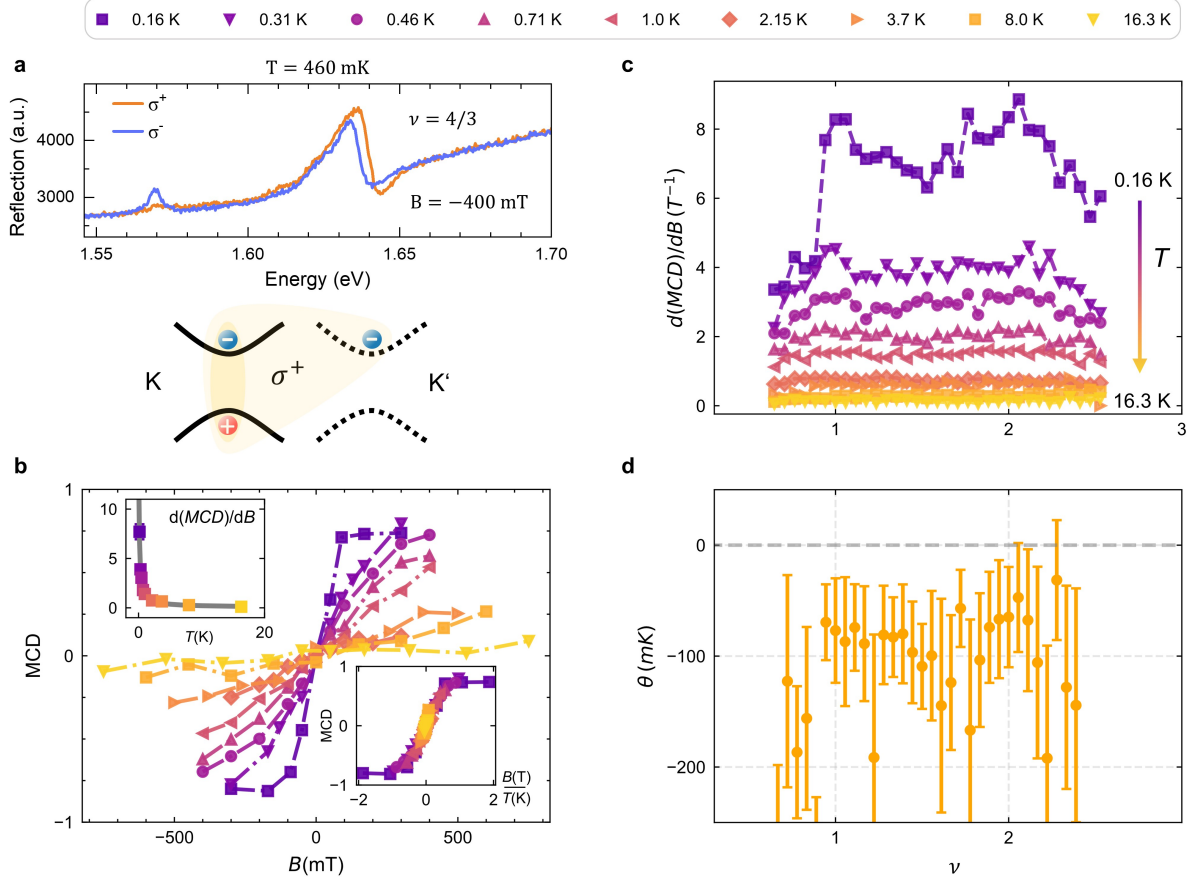


Figure 5.18: Magnetic circular dichroism (MCD) of M_1^- between $\nu = 1$ and 2 electrons per moiré cell. (a) White light reflection spectra of the sample S2 in $\sigma^{+/-}$ polarization for $\nu = 4/3$, $B = -400$ mT and $T = 460$ mK. The M_1^- peak at 1.57 eV is strongly polarized, reminiscent of the canonical trion in monolayer MoSe₂ illustrated in the schematics. (b) MCD of M_1^- , evaluated as the polarization contrast $MCD = (A_{\sigma^+} - A_{\sigma^-}) / (A_{\sigma^+} + A_{\sigma^-})$, with $A_{\sigma^{+/-}}$ being the reflection contrast of the peak M_1^- in $\sigma^{+/-}$ circular polarization, as a function of the magnetic field at $\nu = 1$ [16]. As for the g -factors of \tilde{M}_2^- shown in Fig. 5.17, the slopes $d(MCD)/dB$ decrease with increasing temperature. The left inset shows the Curie-Weiss fit of the slopes at small fields, and the right inset shows the scaling collapse of the MCD data as a function of B/T . (c) The slopes of MCD with respect to B at small fields exhibit consistently high values throughout the stability regime of M_1^- , with fluctuations on the order of 10 – 15% similar to the behavior of the g -factors of \tilde{M}_2^- . Across all temperatures there are two maxima around $\nu = 1$ and 2 as well as a local minimum around $\nu = 3/2$. (d) Curie temperatures extracted from the MCD-slopes in (c) indicate weak antiferromagnetic exchange.

Summary and outlook

Transition metal dichalcogenides are a family of layered van der Waals materials that have attracted growing interest over the last decade. In their monolayer limit, TMDs present direct band gap semiconductors with band gaps in the visible range [10, 49]. Their large effective electron and hole masses [73] in combination with reduced Coulomb screening [105] result in tightly bound excitons that are characterized by very strong light-matter coupling [75, 83], opening perspectives for future optoelectronic and photonic applications [69–72] as well as fundamental quantum research [11, 83–85, 227].

The vertical stacking of two monolayers with small mismatch in the lattice constant or rotational twist generally results in the emergence of a long-range moiré superlattice. The moiré effect is a purely geometric phenomenon [86], and the lattice constant of the moiré pattern depends sensitively on the rotation angle between the two monolayers. The periodic modulation of the interlayer atomic registries typically results in a periodic potential that greatly influences the local quasi-particle band gaps in the individual layers and provides a scaffold for ordered electronic states [11, 84, 87, 227]. By controlling parameters such as the choice of materials, their rotational alignment as well as the dielectric environment, one can engineer the structure of the emerging moiré bands and by this control the physical properties of the respective van der Waals heterostructure. This tunability established TMDs as a very versatile platform for designing artificial materials, allowing for tailored implementations of correlated many-body systems [87, 88, 227].

When talking about monolayers of TMDs, one typically considers the four materials MoS_2 , MoSe_2 , WS_2 and WSe_2 [10] (although telluride-based TMDs gain more and more interest recently). This results in a total of six possible TMD heterobilayers: $\text{MoSe}_2/\text{WSe}_2$, WS_2/WSe_2 , $\text{MoSe}_2/\text{MoS}_2$, $\text{MoS}_2/\text{WSe}_2$, $\text{MoSe}_2/\text{WS}_2$ and MoS_2/WS_2 . Given the plethora of phenomena in TMD heterostructures, whole scientific careers can be pursued by focusing on either of these six combinations. In this work, we turned our focus to the $\text{MoSe}_2/\text{WS}_2$ heterostructure which is characterized by the closely aligned conduction bands of the two constituent materials. Initially acting as a source of confusion [14, 15, 191, 192, 209, 210], the band resonance in $\text{MoSe}_2/\text{WS}_2$ ultimately allows for electrostatic tunability of the conduction band alignment and

the hybridization of both electronic and excitonic bands [17], introducing degrees of freedom unavailable in other commonly studied heterostructures such as WS_2/WSe_2 .

In the beginning of this project, the literature on $MoSe_2/WS_2$ was marked by a controversy on the underlying band alignment and the nature of its excitonic ground states [14, 15, 191, 192, 209, 210]. Throughout the course of this work and by using comprehensive theoretical and experimental tools, we arrived at the main result of this thesis which is a clarified description of the exciton physics in angle-aligned $MoSe_2/WS_2$ heterostructures. In particular, our elaborate understanding of the low-energy optoelectronics in this system enabled the discovery of the peculiar charging sequence that leads to the emergence of a bilayer spin-charge lattice in antiparallel $MoSe_2/WS_2$, establishing it as a new platform for studies of correlated many-body physics in the bilayer Fermi-Hubbard model.

In Chapter 4, we introduced the theoretical tools that have proved fundamental in the development of this thesis. In particular, this included the continuum model that combined previously separate models [180, 187, 188, 195, 196] into a single Hamiltonian that can describe an intralayer moiré potential as well as resonant interlayer coupling simultaneously. Furthermore, we provided a conceptually clarified discussion of the simple capacitance model for TMD heterostructures [134, 202–204], allowing to perform calculations with arbitrary non-linear forms of the charge density as a function of the chemical potential.

In Chapter 5, we applied the developed models to experimental data in both parallel and antiparallel $MoSe_2/WS_2$ heterostructures. With access to cryogenic temperatures, ambipolar charge carrier doping as well as electric and magnetic out-of-plane fields, we performed extensive spectroscopic studies that allowed us to unambiguously characterize the nature of the low-energy moiré excitons and their interactions with charge carriers. Our results indicate that contrary to some early reports, the conduction band offset of $MoSe_2/WS_2$ is of type I, with the band gap of the heterostructure given by that of $MoSe_2$. The CB minimum of WS_2 , however, lies only tens of meV above that of $MoSe_2$ and can be tuned in resonance with the latter by moderate electric fields. As a result, it is possible to artificially change the band alignment between type I and type II, controlling both the hybridization and the electric dipole character of the energetically lowest exciton states. Moreover, our theoretical description indicates deep moiré potentials with peak-to-peak amplitudes above 100 meV, leading to the localization of free electrons and strong Coulomb interaction effects. This results in renormalized flat bands that lead to the realization of a staggered bilayer triangular lattice of electrons. The bilayer lattice emerges due to a charge filling behavior that proceeds layer-by-layer, with the first and second electron per moiré cell consecutively occupying the $MoSe_2$ and the WS_2 layer. We described the observed charging sequence by the above electrostatic model and provided experimental evidence of spin correlations on the vertically offset and laterally staggered bilayer lattice, yielding absolute exciton Landé factors as high as 600 at lowest temperatures. The bilayer character

of the implemented spin-charge lattice allowed for electrostatic tunability of Ruderman-Kittel-Kasuya-Yosida magnetism [219, 220], establishing antiparallel MoSe₂/WS₂ heterostructures as a viable platform for studies of bilayer Hubbard model physics with exotic magnetic phases on frustrated lattices.

In summary, our work provides an in-depth characterization of the exciton physics in angle-aligned MoSe₂/WS₂ and demonstrates the emergence of a bilayer triangular electron lattice with pronounced antiferromagnetic correlations. While we provided an extensive phenomenological description, further studies are needed to fully pin down the physical properties of all of the observed phenomena. From the theoretical side, *ab initio* calculations could provide insight on the individual moiré potentials for electrons, holes and excitons, helping to elucidate the inner structure of the observed moiré excitons and their dispersion with external fields. Furthermore, many-body correlation effects such as Wigner crystallization of charge carriers are expected to play a non-negligible role in the physics of spin-charge lattices at fractional and integer filling factors. From the experimental side, neither electron densities beyond the filling factor of 2.5 nor the hole-doped side were much considered in this work. Further insight on the correlated states could be obtained by comprehensive optical and transport measurements, while advanced imaging techniques such as transmission electron microscopy (TEM) or scanning tunneling microscopy (STM) could enable one-to-one correspondence between theoretical and experimental results. Finally, exploring the full field-dependent phase space of the bilayer Hubbard model presents an avenue to implement previously unavailable model systems related to the physics of Mott insulating states and their relation to unconventional superconductivity. The possibility of tuning interlayer coupling and magnetic exchange interactions establishes antiparallel MoSe₂/WS₂ as a fertile ground for manifestations of kinetic magnetism and other theoretically predicted phases in related settings, providing compelling motivation for future experimental and theoretical work on many-body phenomena and magnetism in antiparallel MoSe₂/WS₂ heterostacks.

Software development in Python

We have already mentioned in Chapter 3 that in a modern laboratory, it is imperative to design efficient tools for both data acquisition and analysis. The pipelines in data acquisition typically rely on third-party packages and straightforward control structures. While some of the device manufacturers (e.g. attocube) provide C++ dynamically linked libraries (DLLs) that can be used from within Python, other devices (e.g. the inevitable Yokogawa 7561) can be controlled through open-source libraries such as *PyMeasure* that builds upon *PyVISA*.

For data analysis, on the other hand, new scientific questions often require the development of new evaluation tools appropriate for the respective problem. In the present work, the amount of spectroscopic data necessitated efficient high-throughput routines that would barely be possible with traditional plotting software such as *Origin*. As a solution, we relied heavily on the software language Python and its common scientific packages *numpy*, *scipy* and *matplotlib*.

In this appendix, we present two abstract classes that played a key role in the data evaluation by allowing live interaction with the acquired data, and we hope that they turn out to be useful in case the reader wishes to develop his own tools. The first one – called *InteractiveCursor* in the following code example – provides basic GUI methods to link mouse events to custom Python functions.

```
1 class InteractiveCursor():
2     '''
3     Abstract class to create an interactive cursor for matplotlib figures.
4     The class instance needs to register a matplotlib axis
5     and method(s) to be called when clicking events occur.
6
7     Parameters for initialization
8     -----
9     axis : matplotlib axis instance, the cursor will be responsive in this axis
10    only.
11    method_offclick : function to be called when the mouse button is released.
12    DEFAULT is NONE
```

```
11     *method_moved : function to be called when the mouse is moved while being
12     clicked. DEFAULT is equal to method_offclick
13     '''
14     def __init__(self, axis, method_offclick=None, *method_moved):
15         '''
16         The methods provided are called everytime the corresponding event occurs. When
17         not provided, 'method_moved' is set equal to 'method_offclick'.
18         '''
19         self.axis=axis
20         self.current_pos=[0,0]
21
22         self.fig=plt.gcf()   ### Get current figure for event handling
23
24         ### Tools for interactive mouse events
25         self.connection_onclick=self.fig.canvas.mpl_connect('button_press_event',
26 self. onclick)
27         self.method_offclick=method_offclick
28
29         if method_moved == True:
30             self.method_moved=method_moved[0]
31         else: self.method_moved=method_offclick
32
33     def onclick(self,event):
34         '''
35         When the mouse is clicked, a GUI connection for mouse moving and releasing
36         events is established
37         '''
38         if event.inaxes !=self.axis:
39             return
40
41         self.connection_mouse_clicked=self.fig.canvas.mpl_connect('
42 motion_notify_event', self.move_mouse_while_clicked)
43         self.connection_offclick=self.fig.canvas.mpl_connect('button_release_event'
44 , self.offclick)
45         return
46
47     def offclick(self,event):
48         '''
49         When the mouse is released within the interactive axis, method_offclick()
50         is called, all GUI connections are disconnected, and the current position of
51         the mouse is returned
52         '''
53         if event.inaxes != self.axis:
54             return
55
56         self.current_pos=[event.xdata, event.ydata]
57         self.fig.canvas.mpl_disconnect(self.connection_mouse_clicked)
```

```

48     self.fig.canvas.mpl_disconnect(self.connection_offclick)
49     self.method_offclick()
50     return self.current_pos
51
52     def move_mouse_while_clicked(self, event):
53         '''
54         When the mouse is moved while being clicked, method_moved() is called and
55         the current position is returned
56         '''
57         if event.inaxes != self.axis:
58             return
59         self.current_pos=[event.xdata, event.ydata]
60         self.method_moved()
61         return self.current_pos
62
63     def get_position(self, swap_coordinates=False):
64         '''
65         Returns the current position of the cursor
66         '''
67         if swap_coordinates == False:
68             return self.current_pos
69         else:
70             return [self.current_pos[1], self.current_pos[0]]

```

Python code A.1: A class to create interactive matplotlib figures.

It can be used inside another class to enable interactive updates of a *matplotlib* axis by calling a custom function as shown in the following minimal working example:

```

1 self.map_cursor=InteractiveCursor(axis=self.ax_map, method_offclick=self.
2 mouse_update ) ### interactive cursor control, calls self.mouse_update upon
3 releasing/moving a clicked mouse button
4
5 def mouse_update(self): ### function called when you navigate with the cursor
6 self.current_pixel=np.array([int(round(x)) for x in self.map_cursor.
7 get_position(swap_coordinates=True)]) ### obtain the pixel coordinates of the
8 cursor position
9 self.spectral_plot.set_ydata(self.spectra[self.current_pixel[0],self.
10 current_pixel[1],:]) ### update the spectral plot
11 self.current_pos_cursor.set_offsets([self.current_pixel[1],self.current_pixel
12 [0]]) ### update the position of the red cursor
13
14 plt.draw()

```

Python code A.2: A minimal working example for using the InteractiveCursor.

In Fig. A.1, we show a typical application for visualization of hyperspectral data (i.e. three-dimensional data where a one-dimensional spectrum is acquired for a two-dimensional array of pixels that can represent spatial position or electrostatic gate voltages). Here, the spectral signal is projected onto its maximum inside a given spectral range and then visualized in a heatmap for an array of pixels that correspond to different top and bottom gate voltages. By virtue of the InteractiveCursor, it is possible to explore the whole 2D voltage-space in very short time.

The second class presented here is called LineDrawer and is shown in the code example A.3 below. It builds on a similar idea and employs basic GUI methods accessible in *matplotlib* in order to draw custom functions. This allows one to interactively define and pass arbitrary functional forms to other routines such as the capacitance model introduced in section 4.4. In particular, the à priori non-linear behavior of the charge density $n(E) = \int_0^E \text{DOS}(E') dE'$ inhibits automatic fitting procedures except in the case of well-defined functional forms that can be quantified by a limited set of numbers. The LineDrawer class, on the other hand, enables a fast-paced way to fit the true form of $n(E)$ by trial-and-error without arbitrary limitations on the form of the test functions. In particular, it was a key tool in fitting the non-trivial charging behavior of sample S1 in section 5.3 and obtaining the peaked density of states presented in Fig. 5.14c.

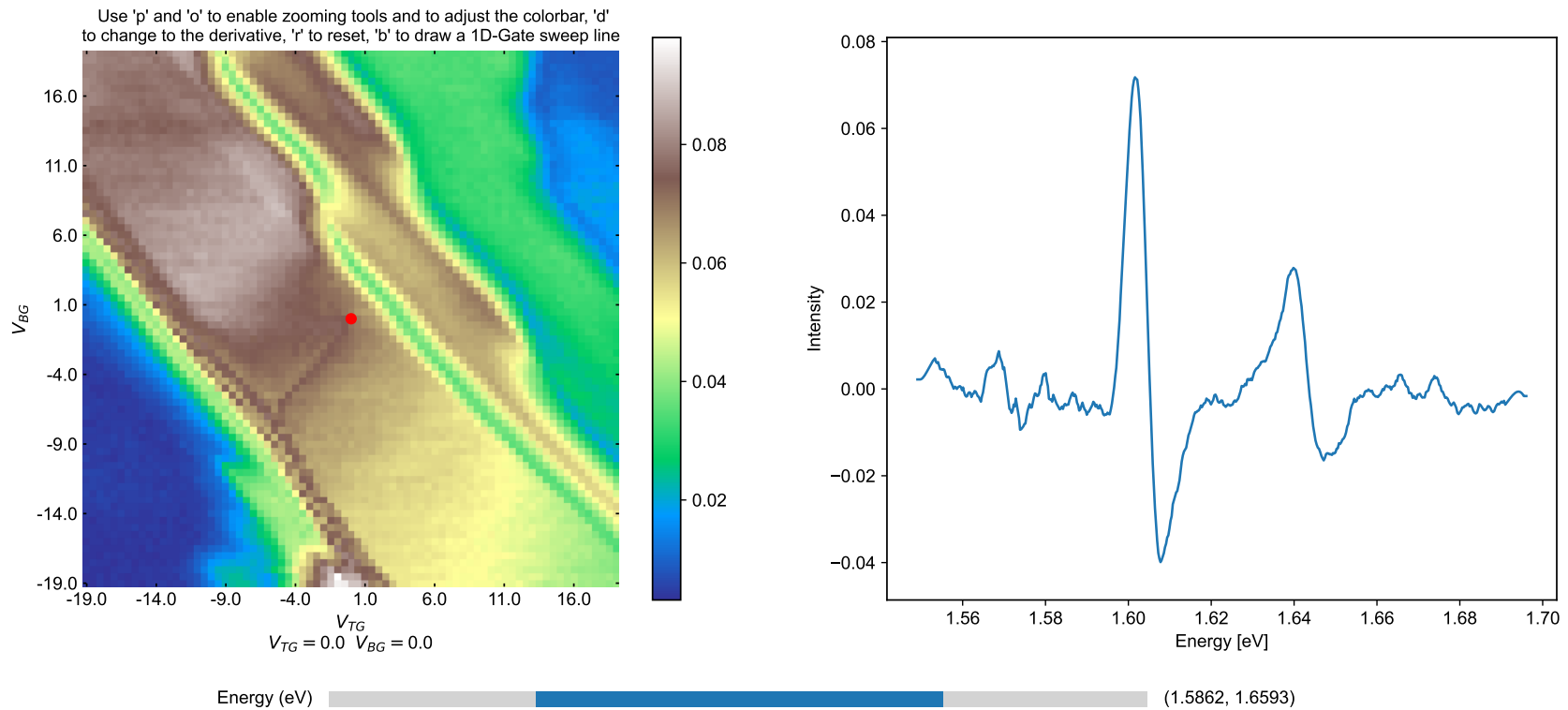


Figure A.1: Interface of the interactive analysis script for three-dimensional data (here gate voltage dependent DR). In the map on the left, the spectral signal is projected onto its maximum inside the range defined by the slider in the bottom. The red dot inside the map can be moved interactively in order to display the spectrum at any given position.

```
1 class LineDrawer:
2     def __init__(self, line, offclick_call=None):
3         self.line = line
4         self.fig = line.figure
5         self.xs = list(line.get_xdata())
6         self.ys = list(line.get_ydata())
7         self.function = None
8         if offclick_call is not None:
9             self.offclick_call = offclick_call
10        self.conn_mouse_click=self.fig.canvas.mpl_connect('button_press_event',
self.mouse_clicked_on)
11
12    def mouse_clicked_on(self,event):
13        if event.inaxes !=self.line.axes:
14            return
15        self.conn_mouse_release=self.fig.canvas.mpl_connect('button_release_event',
self.mouse_released_on)
16        self.conn_mouse_clicked=self.fig.canvas.mpl_connect('motion_notify_event',
self.move_mouse_while_clicked)
17
18    def mouse_released_on(self,event):
19        if event.inaxes !=self.line.axes:
20            return
21
22        self.fig.canvas.mpl_disconnect(self.conn_mouse_clicked)
23        self.fig.canvas.mpl_disconnect(self.conn_mouse_release)
24
25        self.function = scipy.interpolate.interpld(self.xs, self.ys, bounds_error=
False, fill_value='extrapolate')
26        self.offclick_call()
27
28    def move_mouse_while_clicked(self,event):
29        if event.inaxes !=self.line.axes:
30            return
31        if len(self.xs) == 0:
32            self.xs.append(event.xdata)
33            self.ys.append(event.ydata)
34        elif event.xdata > self.xs[-1]:
35            self.xs.append(event.xdata)
36            self.ys.append(max(event.ydata, self.ys[-1]))
37        self.line.set_data(self.xs, self.ys)
38        self.line.figure.canvas.draw()
```

Python code A.3: A class to interactively draw custom functions.

Bibliography

1. Einstein, A. "Über einen die Erzeugung und Verwandlung des Lichtes betreffenden heuristischen Gesichtspunkt". *Ann. Phys.* **322**, 132–148 (Jan. 1905).
2. Tomm, N., Javadi, A., Antoniadis, N. O., *et al.* "A bright and fast source of coherent single photons". *Nat. Nanotechnol.* **16**, 399–403 (Apr. 2021).
3. Chang, J. & Esmail Zadeh, I. "Superconducting single-photon detectors get hot". *Nat. Nanotechnol.* **18**, 322–323 (Apr. 2023).
4. Seitz, F. & Einspruch, N. G. *Electronic Genie: The Tangled History of Silicon* (University of Illinois Press, 1998).
5. Jaeger, L. *The Stumbling Progress of 20th Century Science* (Springer International Publishing, Cham, Switzerland).
6. Ifrah, G. *The Universal History of Computing: From the Abacus to the Quantum Computer* (Wiley, Hoboken, NJ, USA, Jan. 2002).
7. Christensen, D. V., Dittmann, R., Linares-Barranco, B., *et al.* "2022 roadmap on neuromorphic computing and engineering". *Neuromorph. Comput. Eng.* **2**, 022501 (May 2022).
8. Zheng, H., Liu, Q., Kravchenko, I. I., *et al.* "Multichannel meta-imagers for accelerating machine vision". *Nat. Nanotechnol.* (Jan. 2024).
9. Kim, J., Roh, J., Park, M., *et al.* "Recent Advances and Challenges of Colloidal Quantum Dot Light-Emitting Diodes for Display Applications". *Adv. Mater.*, 2212220 (Feb. 2023).
10. Manzeli, S., Ovchinnikov, D., Pasquier, D., *et al.* "2D transition metal dichalcogenides". *Nat. Rev. Mater.* **2**, 17033 (June 2017).
11. Mak, K. F. & Shan, J. "Semiconductor moiré materials". *Nat. Nanotechnol.* **17**, 686–695 (July 2022).
12. Zhao, S., Li, Z., Huang, X., *et al.* "Excitons in mesoscopically reconstructed moiré heterostructures". *Nat. Nanotechnol.* **18**, 572–579 (June 2023).

13. Tang, Y., Li, L., Li, T., *et al.* "Simulation of Hubbard model physics in WSe₂/WS₂ moiré superlattices". *Nature* **579**, 353–358 (Mar. 2020).
14. Zhang, C., Gong, C., Nie, Y., *et al.* "Systematic study of electronic structure and band alignment of monolayer transition metal dichalcogenides in van der Waals heterostructures". *2D Mater.* **4**, 015026 (Nov. 2016).
15. Tang, Y., Gu, J., Liu, S., *et al.* "Dielectric catastrophe at the Wigner-Mott transition in a moiré superlattice". *Nat. Commun.* **13**, 4271 (July 2022).
16. Ciorciaro, L., Smoleński, T., Morera, I., *et al.* "Kinetic magnetism in triangular moiré materials". *Nature* **623**, 509–513 (Nov. 2023).
17. Polovnikov, B., Scherzer, J., Misra, S., *et al.* "Field-Induced Hybridization of Moiré Excitons in MoSe₂/WS₂ Heterobilayers". *Phys. Rev. Lett.* **132**, 076902 (Feb. 2024).
18. Polovnikov, B., Scherzer, J., Misra, S., *et al.* "Implementation of the bilayer Hubbard model in a moiré heterostructure". arXiv: 2404.05494 (Apr. 2024).
19. Klitzing, K. v., Dorda, G. & Pepper, M. "New Method for High-Accuracy Determination of the Fine-Structure Constant Based on Quantized Hall Resistance". *Phys. Rev. Lett.* **45**, 494–497 (Aug. 1980).
20. Zory Jr., P. S. *Quantum Well Lasers* (Elsevier, Academic Press, 1993).
21. Momma, K. & Izumi, F. "VESTA 3 for three-dimensional visualization of crystal, volumetric and morphology data". *J. Appl. Crystallogr.* **44**, 1272–1276 (Dec. 2011).
22. Wallace, P. R. "The band theory of graphite". *Physical review* **71**, 622 (1947).
23. Boehm, H. P., Clauss, A., Fischer, G., *et al.* "SURFACE PROPERTIES OF EXTREMELY THIN GRAPHITE LAMELLAE". *Proceedings of the Fifth Conference on Carbon*, 73–80 (Jan. 1962).
24. Saito, R., Fujita, M., Dresselhaus, G., *et al.* "Electronic structure of graphene tubules based on C₆₀". *Phys. Rev. B* **46**, 1804–1811 (July 1992).
25. Oshima, C. & Nagashima, A. "Ultra-thin epitaxial films of graphite and hexagonal boron nitride on solid surfaces". *J. Phys.: Condens. Matter* **9**, 1 (Jan. 1997).
26. Geim, A. K. & Novoselov, K. S. "The rise of graphene". *Nat. Mater.* **6**, 183–191 (Mar. 2007).
27. Castro Neto, A. H., Guinea, F., Peres, N. M. R., *et al.* "The electronic properties of graphene". *Rev. Mod. Phys.* **81**, 109–162 (Jan. 2009).
28. Cooper, D. R., D'Anjou, B., Ghattamaneni, N., *et al.* "Experimental Review of Graphene". *International Scholarly Research Notices* **2012**, 501686 (Apr. 2012).

29. Novoselov, K. S., Geim, A. K., Morozov, S. V., *et al.* "Electric Field Effect in Atomically Thin Carbon Films". *Science* **306**, 666–669 (Oct. 2004).
30. Gusynin, V. P. & Sharapov, S. G. "Unconventional Integer Quantum Hall Effect in Graphene". *Phys. Rev. Lett.* **95**, 146801 (Sept. 2005).
31. Novoselov, K. S., McCann, E., Morozov, S. V., *et al.* "Unconventional quantum Hall effect and Berry's phase of 2π in bilayer graphene". *Nat. Phys.* **2**, 177–180 (Mar. 2006).
32. Nomura, K. & MacDonald, A. H. "Quantum Hall Ferromagnetism in Graphene". *Phys. Rev. Lett.* **96**, 256602 (June 2006).
33. Katsnelson, M. I., Novoselov, K. S. & Geim, A. K. "Chiral tunnelling and the Klein paradox in graphene". *Nat. Phys.* **2**, 620–625 (Sept. 2006).
34. Novoselov, K. S., Jiang, Z., Zhang, Y., *et al.* "Room-Temperature Quantum Hall Effect in Graphene". *Science* **315**, 1379 (Mar. 2007).
35. Ponomarenko, L. A., Geim, A. K., Zhukov, A. A., *et al.* "Tunable metal–insulator transition in double-layer graphene heterostructures". *Nat. Phys.* **7**, 958–961 (Dec. 2011).
36. Cao, Y., Fatemi, V., Fang, S., *et al.* "Unconventional superconductivity in magic-angle graphene superlattices". *Nature* **556**, 43–50 (Apr. 2018).
37. Novoselov, K. S., Fal'ko, V. I., Colombo, L., *et al.* "A roadmap for graphene". *Nature* **490**, 192–200 (Oct. 2012).
38. Haigh, S. J., Gholinia, A., Jalil, R., *et al.* "Cross-sectional imaging of individual layers and buried interfaces of graphene-based heterostructures and superlattices". *Nat. Mater.* **11**, 764–767 (Sept. 2012).
39. Dean, C. R., Wang, L., Maher, P., *et al.* "Hofstadter's butterfly and the fractal quantum Hall effect in moiré superlattices". *Nature* **497**, 598–602 (May 2013).
40. Geim, A. K. & Grigorieva, I. V. "Van der Waals heterostructures". *Nature* **499**, 419–425 (July 2013).
41. Withers, F., Del Pozo-Zamudio, O., Mishchenko, A., *et al.* "Light-emitting diodes by band-structure engineering in van der Waals heterostructures". *Nat. Mater.* **14**, 301–306 (Mar. 2015).
42. Novoselov, K. S., Mishchenko, A., Carvalho, A., *et al.* "2D materials and van der Waals heterostructures". *Science* **353**, 6298 (July 2016).
43. Liu, Y., Weiss, N. O., Duan, X., *et al.* "Van der Waals heterostructures and devices". *Nat. Rev. Mater.* **1**, 16042 (July 2016).

44. Mounet, N., Gibertini, M., Schwaller, P., *et al.* "Two-dimensional materials from high-throughput computational exfoliation of experimentally known compounds". *Nat. Nanotechnol.* **13**, 246–252 (Mar. 2018).
45. Li, L. J., O'Farrell, E. C. T., Loh, K. P., *et al.* "Controlling many-body states by the electric-field effect in a two-dimensional material". *Nature* **529**, 185–189 (Jan. 2016).
46. Tsen, A. W., Hunt, B., Kim, Y. D., *et al.* "Nature of the quantum metal in a two-dimensional crystalline superconductor". *Nat. Phys.* **12**, 208–212 (Mar. 2016).
47. Yu, Y., Ma, L., Cai, P., *et al.* "High-temperature superconductivity in monolayer $\text{Bi}_2\text{Sr}_2\text{CaCu}_2\text{O}_{8+\delta}$ ". *Nature* **575**, 156–163 (Nov. 2019).
48. Castellanos-Gomez, A. "Why all the fuss about 2D semiconductors?" *Nat. Photonics* **10**, 202–204 (Apr. 2016).
49. Chaves, A., Azadani, J. G., Alsalman, H., *et al.* "Bandgap engineering of two-dimensional semiconductor materials". *npj 2D Mater. Appl.* **4**, 29 (Aug. 2020).
50. Dean, C. R., Young, A. F., Meric, I., *et al.* "Boron nitride substrates for high-quality graphene electronics". *Nat. Nanotechnol.* **5**, 722–726 (Oct. 2010).
51. Gong, C. & Zhang, X. "Two-dimensional magnetic crystals and emergent heterostructure devices". *Science* **363**, 6428 (Feb. 2019).
52. Gibertini, M., Koperski, M., Morpurgo, A. F., *et al.* "Magnetic 2D materials and heterostructures". *Nat. Nanotechnol.* **14**, 408–419 (May 2019).
53. Xu, S.-Y., Ma, Q., Shen, H., *et al.* "Electrically switchable Berry curvature dipole in the monolayer topological insulator WTe_2 ". *Nat. Phys.* **14**, 900–906 (Sept. 2018).
54. Hu, X.-k., Pang, Z.-x., Zhang, C.-w., *et al.* "A two-dimensional robust topological insulator with coexisting ferroelectric and valley polarization". *J. Mater. Chem. C* **7**, 9406–9412 (Aug. 2019).
55. Xu, M., Liang, T., Shi, M., *et al.* "Graphene-Like Two-Dimensional Materials". *Chem. Rev.* **113**, 3766–3798 (May 2013).
56. Molaei, M. J., Younas, M. & Rezakazemi, M. "A Comprehensive Review on Recent Advances in Two-Dimensional (2D) Hexagonal Boron Nitride". *ACS Appl. Electron. Mater.* **3**, 5165–5187 (Dec. 2021).
57. Greim, J. & Schwetz, K. A. in *Ullmann's Encyclopedia of Industrial Chemistry* (Wiley-VCH Verlag GmbH & Co. KGaA, Weinheim, Germany, Dec. 2006).
58. Watanabe, K., Taniguchi, T. & Kanda, H. "Direct-bandgap properties and evidence for ultraviolet lasing of hexagonal boron nitride single crystal". *Nat. Mater.* **3**, 404–409 (June 2004).

59. Kubota, Y., Watanabe, K., Tsuda, O., *et al.* "Deep Ultraviolet Light-Emitting Hexagonal Boron Nitride Synthesized at Atmospheric Pressure". *Science* **317**, 932–934 (Aug. 2007).
60. Caldwell, J. D., Aharonovich, I., Cassabois, G., *et al.* "Photonics with hexagonal boron nitride". *Nat. Rev. Mater.* **4**, 552–567 (Aug. 2019).
61. Rhodes, D., Chae, S. H., Ribeiro-Palau, R., *et al.* "Disorder in van der Waals heterostructures of 2D materials". *Nat. Mater.* **18**, 541–549 (June 2019).
62. Cadiz, F., Courtade, E., Robert, C., *et al.* "Excitonic Linewidth Approaching the Homogeneous Limit in MoS₂-Based van der Waals Heterostructures". *Phys. Rev. X* **7**, 021026 (May 2017).
63. Shao, F., Woo, S. Y., Wu, N., *et al.* "Substrate influence on transition metal dichalcogenide monolayer exciton absorption linewidth broadening". *Phys. Rev. Mater.* **6**, 074005 (July 2022).
64. Shree, S., Paradisanos, I., Marie, X., *et al.* "Guide to optical spectroscopy of layered semiconductors". *Nat. Rev. Phys.* **3**, 39–54 (Jan. 2021).
65. Wilson, J. A. & Yoffe, A. D. "The transition metal dichalcogenides discussion and interpretation of the observed optical, electrical and structural properties". *Advances in Physics* **18**, 193–335 (June 1969).
66. Novoselov, K. S., Jiang, D., Schedin, F., *et al.* "Two-dimensional atomic crystals". *Proc. Natl. Acad. Sci. U.S.A.* **102**, 10451–10453 (July 2005).
67. Splendiani, A., Sun, L., Zhang, Y., *et al.* "Emerging Photoluminescence in Monolayer MoS₂". *Nano Lett.* **10**, 1271–1275 (Apr. 2010).
68. Mak, K. F., Lee, C., Hone, J., *et al.* "Atomically Thin MoS₂: A New Direct-Gap Semiconductor". *Phys. Rev. Lett.* **105**, 136805 (Sept. 2010).
69. Radisavljevic, B., Radenovic, A., Brivio, J., *et al.* "Single-layer MoS₂ transistors". *Nat. Nanotechnol.* **6**, 147–150 (Mar. 2011).
70. Wang, Q. H., Kalantar-Zadeh, K., Kis, A., *et al.* "Electronics and optoelectronics of two-dimensional transition metal dichalcogenides". *Nat. Nanotechnol.* **7**, 699–712 (Nov. 2012).
71. Yu, W. J., Li, Z., Zhou, H., *et al.* "Vertically stacked multi-heterostructures of layered materials for logic transistors and complementary inverters". *Nat. Mater.* **12**, 246–252 (Mar. 2013).
72. Lopez-Sanchez, O., Lembke, D., Kayci, M., *et al.* "Ultrasensitive photodetectors based on monolayer MoS₂". *Nat. Nanotechnol.* **8**, 497–501 (July 2013).

73. Kormányos, A., Burkard, G., Gmitra, M., *et al.* “k·p theory for two-dimensional transition metal dichalcogenide semiconductors”. *2D Mater.* **2**, 022001 (Apr. 2015).
74. Mak, K. F. & Shan, J. “Photonics and optoelectronics of 2D semiconductor transition metal dichalcogenides”. *Nat. Photonics* **10**, 216–226 (Apr. 2016).
75. Wang, G., Chernikov, A., Glazov, M. M., *et al.* “Colloquium: Excitons in atomically thin transition metal dichalcogenides”. *Rev. Mod. Phys.* **90**, 021001 (2 Apr. 2018).
76. Xiao, D., Liu, G.-B., Feng, W., *et al.* “Coupled Spin and Valley Physics in Monolayers of MoS₂ and Other Group-VI Dichalcogenides”. *Phys. Rev. Lett.* **108**, 196802 (May 2012).
77. Kośmider, K., González, J. W. & Fernández-Rossier, J. “Large spin splitting in the conduction band of transition metal dichalcogenide monolayers”. *Phys. Rev. B* **88**, 245436 (Dec. 2013).
78. Cao, T., Wang, G., Han, W., *et al.* “Valley-selective circular dichroism of monolayer molybdenum disulphide”. *Nat. Commun.* **3**, 887 (June 2012).
79. Schaibley, J. R., Yu, H., Clark, G., *et al.* “Valleytronics in 2D materials”. *Nat. Rev. Mater.* **1**, 16055 (Aug. 2016).
80. Yu, H., Cui, X., Xu, X., *et al.* “Valley excitons in two-dimensional semiconductors”. *Natl. Sci. Rev.* **2**, 57–70 (Mar. 2015).
81. Koperski, M., Molas, M. R., Arora, A., *et al.* “Optical properties of atomically thin transition metal dichalcogenides: observations and puzzles”. *Nanophotonics* **6**, 1289–1308 (2017).
82. Mak, K. F., He, K., Lee, C., *et al.* “Tightly bound trions in monolayer MoS₂”. *Nat. Mater.* **12**, 207–211 (Mar. 2013).
83. Wilson, N. P., Yao, W., Shan, J., *et al.* “Excitons and emergent quantum phenomena in stacked 2D semiconductors”. *Nature* **599**, 383–392 (Nov. 2021).
84. Kennes, D. M., Claassen, M., Xian, L., *et al.* “Moiré heterostructures as a condensed-matter quantum simulator”. *Nat. Phys.* **17**, 155–163 (Feb. 2021).
85. Huang, D., Choi, J., Shih, C.-K., *et al.* “Excitons in semiconductor moiré superlattices”. *Nat. Nanotechnol.* **17**, 227–238 (Mar. 2022).
86. Hermann, K. “Periodic overlayers and moiré patterns: theoretical studies of geometric properties”. *J. Phys.: Condens. Matter* **24**, 314210 (July 2012).
87. Balents, L., Dean, C. R., Efetov, D. K., *et al.* “Superconductivity and strong correlations in moiré flat bands”. *Nat. Phys.* **16**, 725–733 (July 2020).

88. Bistritzer, R. & MacDonald, A. H. "Moiré bands in twisted double-layer graphene". *Proc. Natl. Acad. Sci. U.S.A.* **108**, 12233–12237 (July 2011).
89. Li, H., Li, S., Regan, E. C., *et al.* "Imaging two-dimensional generalized Wigner crystals". *Nature* **597**, 650–654 (2021).
90. Ribeiro, R. M. & Peres, N. M. R. "Stability of boron nitride bilayers: Ground-state energies, interlayer distances, and tight-binding description". *Phys. Rev. B* **83**, 235312 (June 2011).
91. Zhu, Z. Y., Cheng, Y. C. & Schwingenschlögl, U. "Giant spin-orbit-induced spin splitting in two-dimensional transition-metal dichalcogenide semiconductors". *Phys. Rev. B* **84**, 153402 (Oct. 2011).
92. Cheiwchanchamnangij, T. & Lambrecht, W. R. L. "Quasiparticle band structure calculation of monolayer, bilayer, and bulk MoS₂". *Phys. Rev. B* **85**, 205302 (May 2012).
93. Kumar, A. & Ahluwalia, P. K. "Electronic structure of transition metal dichalcogenides monolayers 1H-MX₂ (M = Mo, W; X = S, Se, Te) from ab-initio theory: new direct band gap semiconductors". *Eur. Phys. J. B* **85**, 186 (June 2012).
94. Komsa, H.-P. & Krasheninnikov, A. V. "Effects of confinement and environment on the electronic structure and exciton binding energy of MoS₂ from first principles". *Phys. Rev. B* **86**, 241201 (Dec. 2012).
95. Molina-Sánchez, A., Sangalli, D., Hummer, K., *et al.* "Effect of spin-orbit interaction on the optical spectra of single-layer, double-layer, and bulk MoS₂". *Phys. Rev. B* **88**, 045412 (July 2013).
96. Qiu, D. Y., da Jornada, F. H. & Louie, S. G. "Optical Spectrum of MoS₂: Many-Body Effects and Diversity of Exciton States". *Phys. Rev. Lett.* **111**, 216805 (Nov. 2013).
97. Liu, G.-B., Shan, W.-Y., Yao, Y., *et al.* "Three-band tight-binding model for monolayers of group-VIB transition metal dichalcogenides". *Phys. Rev. B* **88**, 085433 (Aug. 2013).
98. Jorissen, B., Covaci, L. & Partoens, B. "Comparative analysis of tight-binding models for transition metal dichalcogenides". *SciPost Phys. Core* **7**, 004 (Feb. 2024).
99. Yu, P. Y. & Cardona, M. *Fundamentals of Semiconductors* (Springer, Berlin, Germany).
100. Haug, H. & Koch, S. W. *Quantum Theory of the Optical and Electronic Properties of Semiconductors* (World Scientific Publishing Company, Singapore, Jan. 2009).
101. Frenkel, J. "On the Transformation of light into Heat in Solids. I". *Phys. Rev.* **37**, 17–44 (Jan. 1931).

102. Wannier, G. H. "The Structure of Electronic Excitation Levels in Insulating Crystals". *Phys. Rev.* **52**, 191–197 (Aug. 1937).
103. Mott, N. F. "Conduction in polar crystals. II. The conduction band and ultra-violet absorption of alkali-halide crystals". *Trans. Faraday Soc.* **34**, 500–506 (Jan. 1938).
104. Beal, A. R. & Liang, W. Y. "Excitons in 2H-WSe₂ and 3R-WS₂". *J. Phys. C: Solid State Phys.* **9**, 2459 (June 1976).
105. Durnev, M. V. & Glazov, M. M. "Excitons and trions in two-dimensional semiconductors based on transition metal dichalcogenides". *Phys.-Usp.* **61**, 825 (Dec. 2018).
106. Cudazzo, P., Tokatly, I. V. & Rubio, A. "Dielectric screening in two-dimensional insulators: Implications for excitonic and impurity states in graphane". *Phys. Rev. B* **84**, 085406 (Aug. 2011).
107. Chernikov, A., Berkelbach, T. C., Hill, H. M., *et al.* "Exciton Binding Energy and Nonhydrogenic Rydberg Series in Monolayer WS₂". *Phys. Rev. Lett.* **113**, 076802 (7 Aug. 2014).
108. Robert, C., Lagarde, D., Cadiz, F., *et al.* "Exciton radiative lifetime in transition metal dichalcogenide monolayers". *Phys. Rev. B* **93**, 205423 (May 2016).
109. Ramasubramaniam, A. "Large excitonic effects in monolayers of molybdenum and tungsten dichalcogenides". *Phys. Rev. B* **86**, 115409 (Sept. 2012).
110. Glazov, M. M. "Optical properties of charged excitons in two-dimensional semiconductors". *J. Chem. Phys.* **153**, 034703 (July 2020).
111. Schmidt, R., Enss, T., Pietilä, V., *et al.* "Fermi polarons in two dimensions". *Phys. Rev. A* **85**, 021602 (Feb. 2012).
112. Efimkin, D. K. & MacDonald, A. H. "Many-body theory of trion absorption features in two-dimensional semiconductors". *Phys. Rev. B* **95**, 035417 (Jan. 2017).
113. Sidler, M., Back, P., Cotlet, O., *et al.* "Fermi polaron-polaritons in charge-tunable atomically thin semiconductors". *Nat. Phys.* **13**, 255–261 (2017).
114. Carbone, M. R., Mayers, M. Z. & Reichman, D. R. "Microscopic model of the doping dependence of linewidths in monolayer transition metal dichalcogenides". *J. Chem. Phys.* **152**, 194705 (May 2020).
115. Ross, J. S., Wu, S., Yu, H., *et al.* "Electrical control of neutral and charged excitons in a monolayer semiconductor". *Nat. Commun.* **4**, 1474 (Feb. 2013).
116. Singh, A., Moody, G., Tran, K., *et al.* "Trion formation dynamics in monolayer transition metal dichalcogenides". *Phys. Rev. B* **93**, 041401 (Jan. 2016).

117. Courtade, E., Semina, M., Manca, M., *et al.* "Charged excitons in monolayer WSe₂: Experiment and theory". *Phys. Rev. B* **96**, 085302 (Aug. 2017).
118. Esser, A., Zimmermann, R. & Runge, E. "Theory of Trion Spectra in Semiconductor Nanostructures". *Phys. Status Solidi B* **227**, 317–330 (Oct. 2001).
119. Zipfel, J., Holler, J., Mitioglu, A. A., *et al.* "Spatial extent of the excited exciton states in WS₂ monolayers from diamagnetic shifts". *Phys. Rev. B* **98**, 075438 (Aug. 2018).
120. Smoleński, T., Cotlet, O., Popert, A., *et al.* "Interaction-Induced Shubnikov–de Haas Oscillations in Optical Conductivity of Monolayer MoSe₂". *Phys. Rev. Lett.* **123**, 097403 (Aug. 2019).
121. Robert, C., Han, B., Kapuscinski, P., *et al.* "Measurement of the spin-forbidden dark excitons in MoS₂ and MoSe₂ monolayers". *Nat. Commun.* **11**, 4037 (Aug. 2020).
122. Smoleński, T., Watanabe, K., Taniguchi, T., *et al.* "Spin-Valley Relaxation and Exciton-Induced Depolarization Dynamics of Landau-Quantized Electrons in MoSe₂ Monolayer". *Phys. Rev. Lett.* **128**, 127402 (Mar. 2022).
123. Thureja, D., Imamoglu, A., Smoleński, T., *et al.* "Electrically tunable quantum confinement of neutral excitons". *Nature* **606**, 298–304 (June 2022).
124. Yao, W., Xiao, D. & Niu, Q. "Valley-dependent optoelectronics from inversion symmetry breaking". *Phys. Rev. B* **77**, 235406 (June 2008).
125. Zeng, H., Dai, J., Yao, W., *et al.* "Valley polarization in MoS₂ monolayers by optical pumping". *Nat. Nanotechnol.* **7**, 490–493 (Aug. 2012).
126. Mak, K. F., He, K., Shan, J., *et al.* "Control of valley polarization in monolayer MoS₂ by optical helicity". *Nat. Nanotechnol.* **7**, 494–498 (Aug. 2012).
127. Wang, G., Bouet, L., Lagarde, D., *et al.* "Valley dynamics probed through charged and neutral exciton emission in monolayer WSe₂". *Phys. Rev. B* **90**, 075413 (Aug. 2014).
128. Li, Y., Ludwig, J., Low, T., *et al.* "Valley Splitting and Polarization by the Zeeman Effect in Monolayer MoSe₂". *Phys. Rev. Lett.* **113**, 266804 (Dec. 2014).
129. Srivastava, A., Sidler, M., Allain, A. V., *et al.* "Valley Zeeman effect in elementary optical excitations of monolayer WSe₂". *Nat. Phys.* **11**, 141–147 (Feb. 2015).
130. Stier, A. V., McCreary, K. M., Jonker, B. T., *et al.* "Exciton diamagnetic shifts and valley Zeeman effects in monolayer WS₂ and MoS₂ to 65 Tesla". *Nat. Commun.* **7**, 10643 (Feb. 2016).
131. Goryca, M., Li, J., Stier, A. V., *et al.* "Revealing exciton masses and dielectric properties of monolayer semiconductors with high magnetic fields". *Nat. Commun.* **10**, 4172 (2019).

132. Förste, J., Tepliakov, N. V., Kruchinin, S. Y., *et al.* "Exciton g -factors in monolayer and bilayer WSe_2 from experiment and theory". *Nat. Commun.* **11**, 4539 (Sept. 2020).
133. Woźniak, T., Faria Junior, P. E., Seifert, G., *et al.* "Exciton g factors of van der Waals heterostructures from first-principles calculations". *Phys. Rev. B* **101**, 235408 (23 June 2020).
134. Wang, Z., Chiu, Y.-H., Honz, K., *et al.* "Electrical Tuning of Interlayer Exciton Gases in WSe_2 Bilayers". *Nano Lett.* **18**, 137–143 (Jan. 2018).
135. Jauregui, L. A., Joe, A. Y., Pistunova, K., *et al.* "Electrical control of interlayer exciton dynamics in atomically thin heterostructures". *Science* **366**, 870–875 (Nov. 2019).
136. Gustafson, J. L. in *Encyclopedia of Parallel Computing* 1177–1184 (Springer, Boston, MA, Boston, MA, USA, 2011).
137. Venema, L. "Silicon electronics and beyond - Nature". *Nature* **479**, 309 (Nov. 2011).
138. Krömer, H. *The Nobel Prize in Physics 2000, Lecture*. [Online; accessed 29. Feb. 2024]. Feb. 2024.
139. Mikhail Kats. [Twitter; accessed 29. Feb. 2024]. May 2021.
140. Wang, X., Gong, Y., Shi, G., *et al.* "Chemical Vapor Deposition Growth of Crystalline Monolayer MoSe_2 ". *ACS Nano* **8**, 5125–5131 (May 2014).
141. Bilgin, I., Liu, F., Vargas, A., *et al.* "Chemical Vapor Deposition Synthesized Atomically Thin Molybdenum Disulfide with Optoelectronic-Grade Crystalline Quality". *ACS Nano* **9**, 8822–8832 (Sept. 2015).
142. Liu, B., Fathi, M., Chen, L., *et al.* "Chemical Vapor Deposition Growth of Monolayer WSe_2 with Tunable Device Characteristics and Growth Mechanism Study". *ACS Nano* **9**, 6119–6127 (June 2015).
143. Shen, D., Jin, Y., Zhang, Z., *et al.* "Recent Advances in Spin-coating Precursor Mediated Chemical Vapor Deposition of Two-Dimensional Transition Metal Dichalcogenides". *Precision Chemistry* **2024** (Feb. 2024).
144. Pizzocchero, F., Gammelgaard, L., Jessen, B. S., *et al.* "The hot pick-up technique for batch assembly of van der Waals heterostructures". *Nat. Commun.* **7**, 1–10 (June 2016).
145. Purdie, D. G., Pugno, N. M., Taniguchi, T., *et al.* "Cleaning interfaces in layered materials heterostructures". *Nat. Commun.* **9**, 5387 (Dec. 2018).
146. Onodera, M., Wakafuji, Y., Hashimoto, T., *et al.* "All-dry flip-over stacking of van der Waals junctions of 2D materials using polyvinyl chloride". *Sci. Rep.* **12**, 21963 (Dec. 2022).

147. Sze, S. M. & Ng, K. K. *Physics of Semiconductor Devices* (Apr. 2006).
148. Wu, C.-L., Yuan, H., Li, Y., *et al.* "Gate-Induced Metal–Insulator Transition in MoS₂ by Solid Superionic Conductor LaF₃". *Nano Lett.* **18**, 2387–2392 (Apr. 2018).
149. Zu, H., Dai, W. & de Waele, A. T. A. M. "Development of dilution refrigerators - A review". *Cryogenics* **121**, 103390 (Jan. 2022).
150. Radebaugh, R. & Siegwarth, J. D. "Dilution refrigerator technology". *Cryogenics* **11**, 368–384 (Oct. 1971).
151. Duthil, P. "Material Properties at Low Temperature". *CERN Document Server*, 77–95 (Jan. 2015).
152. Bowers, R. "Magnetic Susceptibility of Copper Metal at Low Temperatures". *Phys. Rev.* **102**, 1486–1488 (June 1956).
153. Trovatiello, C., Katsch, F., Borys, N. J., *et al.* "The ultrafast onset of exciton formation in 2D semiconductors". *Nat. Commun.* **11**, 5277 (Oct. 2020).
154. Madéo, J., Man, M. K. L., Sahoo, C., *et al.* "Directly visualizing the momentum-forbidden dark excitons and their dynamics in atomically thin semiconductors". *Science* **370**, 1199–1204 (Dec. 2020).
155. Karni, O., Esin, I. & Dani, K. M. "Through the Lens of a Momentum Microscope: Viewing Light-Induced Quantum Phenomena in 2D Materials". *Adv. Mater.* **35**, 2204120 (July 2023).
156. Puppini, M., Nicholson, C. W., Monney, C., *et al.* "Excited-state band structure mapping". *Phys. Rev. B* **105**, 075417 (Feb. 2022).
157. Su, H., Xu, D., Cheng, S.-W., *et al.* "Dark-Exciton Driven Energy Funneling into Dielectric Inhomogeneities in Two-Dimensional Semiconductors". *Nano Lett.* **22**, 2843–2850 (Apr. 2022).
158. Wang, G., Marie, X., Gerber, I., *et al.* "Giant Enhancement of the Optical Second-Harmonic Emission of WSe₂ Monolayers by Laser Excitation at Exciton Resonances". *Phys. Rev. Lett.* **114**, 097403 (Mar. 2015).
159. Saito, R., Tatsumi, Y., Huang, S., *et al.* "Raman spectroscopy of transition metal dichalcogenides". *J. Phys.: Condens. Matter* **28**, 353002 (July 2016).
160. Zhang, S., Li, B., Chen, X., *et al.* "Nano-spectroscopy of excitons in atomically thin transition metal dichalcogenides". *Nat. Commun.* **13**, 542 (Jan. 2022).
161. Miroshnichenko, A. E., Flach, S. & Kivshar, Y. S. "Fano resonances in nanoscale structures". *Rev. Mod. Phys.* **82**, 2257–2298 (Aug. 2010).

162. Limonov, M. F., Rybin, M. V., Poddubny, A. N., *et al.* "Fano resonances in photonics". *Nat. Photonics* **11**, 543–554 (Sept. 2017).
163. McIntyre, J. D. E. & Aspnes, D. E. "Differential reflection spectroscopy of very thin surface films". *Surf. Sci.* **24**, 417–434 (Feb. 1971).
164. Arora, A., Mandal, A., Chakrabarti, S., *et al.* "Magneto-optical Kerr effect spectroscopy based study of Landé g-factor for holes in GaAs/AlGaAs single quantum wells under low magnetic fields". *J. Appl. Phys.* **113**, 213505 (June 2013).
165. Jin, C., Regan, E. C., Yan, A., *et al.* "Observation of moiré excitons in WSe₂/WS₂ heterostructure superlattices". *Nature* **567**, 76–80 (Mar. 2019).
166. Steinleitner, P., Merkl, P., Nagler, P., *et al.* "Direct Observation of Ultrafast Exciton Formation in a Monolayer of WSe₂". *Nano Lett.* **17**, 1455–1460 (Mar. 2017).
167. Li, Z., Wang, T., Jin, C., *et al.* "Emerging photoluminescence from the dark-exciton phonon replica in monolayer WSe₂". *Nat. Commun.* **10**, 2469 (June 2019).
168. He, M., Rivera, P., Van Tuan, D., *et al.* "Valley phonons and exciton complexes in a monolayer semiconductor". *Nat. Commun.* **11**, 618 (Jan. 2020).
169. Alén, B., Bickel, F., Karrai, K., *et al.* "Stark-shift modulation absorption spectroscopy of single quantum dots". *Appl. Phys. Lett.* **83**, 2235–2237 (Sept. 2003).
170. Högele, A., Alén, B., Bickel, F., *et al.* "Exciton fine structure splitting of single InGaAs self-assembled quantum dots". *Physica E* **21**, 175–179 (Mar. 2004).
171. Barré, E., Karni, O., Liu, E., *et al.* "Optical absorption of interlayer excitons in transition-metal dichalcogenide heterostructures". *Science* **376**, 406–410 (2022).
172. Sandvik, A. W. & Vidal, G. "Variational Quantum Monte Carlo Simulations with Tensor-Network States". *Phys. Rev. Lett.* **99**, 220602 (Nov. 2007).
173. Orús, R. "Tensor networks for complex quantum systems". *Nat. Rev. Phys.* **1**, 538–550 (Sept. 2019).
174. Giannozzi, P., Baroni, S., Bonini, N., *et al.* "QUANTUM ESPRESSO: a modular and open-source software project for quantum". *J. Phys.: Condens. Matter* **21**, 395502 (Sept. 2009).
175. Weston, A., Zou, Y., Enaldiev, V., *et al.* "Atomic reconstruction in twisted bilayers of transition metal dichalcogenides". *Nat. Nanotechnol.* **15**, 592–597 (July 2020).
176. McGilly, L. J., Kerelsky, A., Finney, N. R., *et al.* "Visualization of moiré superlattices". *Nat. Nanotechnol.* **15**, 580–584 (2020).

177. Rosenberger, M. R., Chuang, H.-J., Phillips, M., *et al.* "Twist Angle-Dependent Atomic Reconstruction and Moiré Patterns in Transition Metal Dichalcogenide Heterostructures". *ACS Nano* **14**, 4550–4558 (Apr. 2020).
178. Halbertal, D., Finney, N. R., Sunku, S. S., *et al.* "Moiré metrology of energy landscapes in van der Waals heterostructures". *Nat. Commun.* **12**, 242 (Jan. 2021).
179. Shabani, S., Halbertal, D., Wu, W., *et al.* "Deep moiré potentials in twisted transition metal dichalcogenide bilayers". *Nat. Phys.* **17**, 720–725 (June 2021).
180. Wu, F., Lovorn, T. & MacDonald, A. H. "Topological Exciton Bands in Moiré Heterojunctions". *Phys. Rev. Lett.* **118**, 147401 (Apr. 2017).
181. Regan, E. C., Wang, D., Jin, C., *et al.* "Mott and generalized Wigner crystal states in WSe₂/WS₂ moiré superlattices". *Nature* **579**, 359–363 (Mar. 2020).
182. Wang, L., Shih, E.-M., Ghiotto, A., *et al.* "Correlated electronic phases in twisted bilayer transition metal dichalcogenides". *Nat. Mater.* **19**, 861–866 (2020).
183. Huang, X., Wang, T., Miao, S., *et al.* "Correlated insulating states at fractional fillings of the WS₂/WSe₂ moiré lattice". *Nat. Phys.* **17**, 715–719 (2021).
184. Ghiotto, A., Shih, E.-M., Pereira, G. S. S. G., *et al.* "Quantum criticality in twisted transition metal dichalcogenides". *Nature* **597**, 345–349 (2021).
185. Xu, Y., Liu, S., Rhodes, D. A., *et al.* "Correlated insulating states at fractional fillings of moiré superlattices". *Nature* **587**, 214–218 (2020).
186. Jin, C., Tao, Z., Li, T., *et al.* "Stripe phases in WSe₂/WS₂ moiré superlattices". *Nat. Mater.* **20**, 940–944 (2021).
187. Wu, F., Lovorn, T. & MacDonald, A. H. "Theory of optical absorption by interlayer excitons in transition metal dichalcogenide heterobilayers". *Phys. Rev. B* **97**, 035306 (3 Jan. 2018).
188. Wu, F., Lovorn, T., Tutuc, E., *et al.* "Hubbard Model Physics in Transition Metal Dichalcogenide Moiré Bands". *Phys. Rev. Lett.* **121**, 026402 (July 2018).
189. Tong, Q., Chen, M., Xiao, F., *et al.* "Interferences of electrostatic moiré potentials and bichromatic superlattices of electrons and excitons in transition metal dichalcogenides". *2D Mater.* **8**, 025007 (Dec. 2020).
190. Zhang, L., Zhang, Z., Wu, F., *et al.* "Twist-angle dependence of moiré excitons in WS₂/MoSe₂ heterobilayers". *Nat. Commun.* **11**, 5888 (Nov. 2020).
191. Alexeev, E. M., Ruiz-Tijerina, D. A., Danovich, M., *et al.* "Resonantly hybridized excitons in moiré superlattices in van der Waals heterostructures". *Nature* **567**, 81–86 (Mar. 2019).

192. Tang, Y., Gu, J., Liu, S., *et al.* "Tuning layer-hybridized moiré excitons by the quantum-confined Stark effect". *Nat. Nanotechnol.* **16**, 52–57 (2021).
193. Naik, M. H., Regan, E. C., Zhang, Z., *et al.* "Intralayer charge-transfer moiré excitons in van der Waals superlattices". *Nature* **609**, 52–57 (Sept. 2022).
194. Tran, K., Moody, G., Wu, F., *et al.* "Evidence for moiré excitons in van der Waals heterostructures". *Nature* **567**, 71–75 (Mar. 2019).
195. Wang, Y., Wang, Z., Yao, W., *et al.* "Interlayer coupling in commensurate and incommensurate bilayer structures of transition-metal dichalcogenides". *Phys. Rev. B* **95**, 115429 (11 Mar. 2017).
196. Ruiz-Tijerina, D. A. & Fal'ko, V. I. "Interlayer hybridization and moiré superlattice minibands for electrons and excitons in heterobilayers of transition-metal dichalcogenides". *Phys. Rev. B* **99**, 125424 (12 Mar. 2019).
197. Zhang, Y., Devakul, T. & Fu, L. "Spin-textured Chern bands in AB-stacked transition metal dichalcogenide bilayers". *Proc. Natl. Acad. Sci. U.S.A.* **118**, e2112673118 (Sept. 2021).
198. Reddy, A. P., Alsallom, F., Zhang, Y., *et al.* "Fractional quantum anomalous Hall states in twisted bilayer MoTe₂ and WSe₂". *Phys. Rev. B* **108**, 085117 (Aug. 2023).
199. Chang, Y.-W. "Continuum model study of optical absorption by hybridized moiré excitons in transition metal dichalcogenide heterobilayers". *Phys. Rev. B* **108**, 155424 (Oct. 2023).
200. Boettcher, S. W., Oener, S. Z., Lonergan, M. C., *et al.* "Potentially Confusing: Potentials in Electrochemistry". *ACS Energy Lett.* **6**, 261–266 (Jan. 2021).
201. Ashcroft, N. W. & Mermin, N. D. *Solid State Physics* (Holt-Saunders, 1976).
202. Tan, Q., Rasmita, A., Zhang, Z., *et al.* "Layer-dependent correlated phases in WSe₂/MoS₂ moiré superlattice". *Nat. Mater.* **22**, 605–611 (May 2023).
203. Popert, A. *Optically Probing Graphene - Excitonic Sensing of Electronic States*. PhD thesis (ETH, Zürich, Switzerland, 2022).
204. Ma, L., Nguyen, P. X., Wang, Z., *et al.* "Strongly correlated excitonic insulator in atomic double layers". *Nature* **598**, 585–589 (Oct. 2021).
205. Keldysh, L. V. "Coulomb interaction in thin semiconductor and semimetal films". *Soviet Journal of Experimental and Theoretical Physics Letters* **29**, 658 (June 1979).
206. Courtade, E., Semina, M., Manca, M., *et al.* "Charged excitons in monolayer WSe₂: Experiment and theory". *Phys. Rev. B* **96**, 085302 (8 Aug. 2017).

207. Semina, M. A. "Excitons and Trions in Bilayer van der Waals Heterostructures". *Phys. Solid State* **61**, 2218–2223 (Nov. 2019).
208. Yang, X. L., Guo, S. H., Chan, F. T., *et al.* "Analytic solution of a two-dimensional hydrogen atom. I. Nonrelativistic theory". *Phys. Rev. A* **43**, 1186–1196 (3 Feb. 1991).
209. Ceballos, F., Bellus, M. Z., Chiu, H.-Y., *et al.* "Probing charge transfer excitons in a MoSe₂–WS₂ van der Waals heterostructure". *Nanoscale* **7**, 17523–17528 (41 2015).
210. Meng, Y., Wang, T., Jin, C., *et al.* "Electrical switching between exciton dissociation to exciton funneling in MoSe₂/WS₂ heterostructure". *Nat. Commun.* **11**, 2640 (May 2020).
211. Gong, C., Zhang, H., Wang, W., *et al.* "Band alignment of two-dimensional transition metal dichalcogenides: Application in tunnel field effect transistors". *Appl. Phys. Lett.* **103**, 053513 (July 2013).
212. Gong, C., Zhang, H., Wang, W., *et al.* "Erratum: "Band alignment of two-dimensional transition metal dichalcogenides: Application in tunnel field effect transistors"". *Appl. Phys. Lett.* **107** (Sept. 2015).
213. Back, P., Sidler, M., Cotlet, O., *et al.* "Giant Paramagnetism-Induced Valley Polarization of Electrons in Charge-Tunable Monolayer MoSe₂". *Phys. Rev. Lett.* **118**, 237404 (June 2017).
214. Campbell, A. J., Brotons-Gisbert, M., Baek, H., *et al.* "Exciton-polarons in the presence of strongly correlated electronic states in a MoSe₂/WSe₂ moiré superlattice". *npj 2D Mater. Appl.* **6**, 79 (Nov. 2022).
215. Faria Junior, P. E. & Fabian, J. "Signatures of Electric Field and Layer Separation Effects on the Spin-Valley Physics of MoSe₂/WSe₂ Heterobilayers: From Energy Bands to Dipolar Excitons". *Nanomaterials* **13**, 1187 (Mar. 2023).
216. Gobato, Y. G., de Brito, C. S., Chaves, A., *et al.* "Distinctive g-Factor of Moiré-Confined Excitons in van der Waals Heterostructures". *Nano Lett.* **22**, 8641–8646 (Nov. 2022).
217. Wang, Y., Kim, J. C., Li, Y., *et al.* "P-type electrical contacts for 2D transition-metal dichalcogenides". *Nature* **610**, 61–66 (Oct. 2022).
218. Xu, Y., Kang, K., Watanabe, K., *et al.* "A tunable bilayer Hubbard model in twisted WSe₂". *Nat. Nanotechnol.* **17**, 934–939 (Sept. 2022).
219. Ruderman, M. A. & Kittel, C. "Indirect Exchange Coupling of Nuclear Magnetic Moments by Conduction Electrons". *Phys. Rev.* **96**, 99–102 (1 Oct. 1954).
220. Coleman, P. *Introduction to Many-Body Physics* (Cambridge University Press, 2015).

221. Y.M. Vilk & A.-M.S. Tremblay. “Non-Perturbative Many-Body Approach to the Hubbard Model and Single-Particle Pseudogap”. *J. Phys. I France* **7**, 1309–1368 (1997).
222. Tremblay, A.-M. S. in *Strongly Correlated Systems: Theoretical Methods* (eds Avella, A. & Mancini, F.) 409–453 (Springer Berlin Heidelberg, Berlin, Heidelberg, 2012).
223. Haerter, J. O. & Shastry, B. S. “Kinetic Antiferromagnetism in the Triangular Lattice”. *Phys. Rev. Lett.* **95**, 087202 (8 Aug. 2005).
224. Sposetti, C. N., Bravo, B., Trumper, A. E., *et al.* “Classical Antiferromagnetism in Kinetically Frustrated Electronic Models”. *Phys. Rev. Lett.* **112**, 187204 (18 May 2014).
225. Morera, I., Kanász-Nagy, M., Smolenski, T., *et al.* “High-temperature kinetic magnetism in triangular lattices”. *Phys. Rev. Res.* **5**, L022048 (2 June 2023).
226. Schlömer, H., Schollwöck, U., Bohrdt, A., *et al.* “Kinetic-to-magnetic frustration crossover and linear confinement in the doped triangular $t - J$ model”. arXiv: 2305 . 02342 (2023).
227. Zhang, Z., Wang, Y., Watanabe, K., *et al.* “Flat bands in twisted bilayer transition metal dichalcogenides”. *Nat. Phys.* **16**, 1093–1096 (2020).

Acknowledgments

It is hard to believe that my journey of the last four years is coming to an end, and I wish to thank all the people who have accompanied and supported me throughout the way. The time of my PhD has been both intense and sprinkled with phases of boredom and creativity, and it gave me the rare opportunity to experience the joy of fighting the unknown and creating knowledge.

It is by pure chance that my scientific pilgrimage has brought me to the field of semiconductor optics. After being trained as a classical statistical physicist, I remember being the only candidate for the *International Max Planck Research School on Quantum Science and Technology* program to have started the presentation by stating $\hbar := 0$. Despite this little 'handicap', I was fortunate to have your trust and support, Alex. Thank you for believing in my abilities and providing me the opportunity to dive into a new field of research. Through your guidance and advice, you helped to shape my scientific worldview, to develop a taste for Soviet style do-it-yourself research tools, and to find a sense of down-to-earth attitude in the too often overhyped scientific landscape.

The frictionless transition to my PhD would also not have been possible without the backing of Erwin Frey who never hesitated to support my decision of switching fields. Thank you for your mentorship and for the continued commitment to our research project from my Master's studies. It has taught me invaluable insights about the scientific process and resulted in my first publication, which will forever keep a place close to my heart.

Next, it goes of course without saying how grateful I am for the amazing group of the Högele lab. Johannes Scherzer, Subhradeep Misra and Anvar Baimuratov – you have been an incredible team and the best example that research is inevitably collaborative. Throughout our project, we have been complementing each other's strengths and weaknesses which resulted in the kind of synergies that lead to unanticipated progress. Without your expertise and dedication, our understanding of the MoSe₂/WS₂ platform would barely be as developed as it is today, and the credit for the results of this work should definitely go to the whole team rather than to a single person. Moreover, I wish to thank everyone else who was involved in different stages of our project, in particular Christian Mohl, Jonathan Förste, Ismail Bilgin, Jonas Göser, Zhijie Li, Xin Huang, and Julian Trapp.

Apart from that, I want to express my gratitude to all my colleagues for the constant support and the positive environment in our workplace, in particular to Viktor Funk, Jonathan Förste and Shen Zhao for their guiding of my inexperienced hands in how to do optical spectroscopy, Jonathan for his outstanding kindness and for introducing me to the culture of good coffee, Samarth Vadia, Lukas Husel and Anna Rupp for our enriching discussions on philosophy, science and the universe, Anvar and Farsane Tabataba-Vakili for your friendship, and Tim Wedl for your frequent reminders that there is still a life outside the scope of a PhD. Moreover, I would like to thank the colleagues of the former Chair Kotthaus – namely Stefan Manus, Heribert Lorenz, Christian Obermayer, Philipp Altpeter, Anton Heindl, and Dayse Ferreira e Silva – for their constant help in keeping things running.

I further wish to thank our theoretical collaborators Henning Schlömer, Fabian Grusdt and Annabelle Bohrdt for their enthusiasm and the help of making sense of our experimental data. Two years ago I would not have expected to get in touch with the field of correlated many-body physics, but your energy and excitement have shown me how interconnected different parts of physics are.

Finally, I am infinitely thankful to all my family and friends who were there all along my journey and helped me to become who I am. Thank you for your love and your backing!

List of publications

- P1 Polovnikov, B., Wilke, P., and Frey E., “Subdiffusive Activity Spreading in the Diffusive Epidemic Process”. *Phys. Rev. Lett.* 128, 078302 (Feb. 2022).
- P2 Polovnikov, B., Scherzer, J., Misra, S., et al. “Field-Induced Hybridization of Moiré Excitons in MoSe₂/WS₂ Heterobilayers”. *Phys. Rev. Lett.* 132, 076902 (Feb. 2024).
- P3 Polovnikov, B., Scherzer, J., Misra, S., et al. “Implementation of the bilayer Hubbard model in a moiré heterostructure”. arXiv: 2404.05494 (Apr. 2024).
- P4 Husel, L., Trapp, J., Scherzer, J., et al. “Cavity-enhanced photon indistinguishability at room temperature and telecom wavelengths”. *Nat. Commun.* 15, 3989 (2024).
- P5 Scherzer, J., Lackner L., Han B., Polovnikov B., et al. “Correlated magnetism of moiré exciton-polaritons on a triangular electron-spin lattice”. arXiv: 2405.12698 (May 2024).

List of abbreviations

TMD	Transition metal dichalcogenides
RKKY	Ruderman-Kittel-Kasuya-Yosida
vdW	van der Waals
hBN	hexagonal Boron Nitride
SOC	Spin-orbit coupling
CVD	Chemical vapor deposition
PL	Photoluminescence
DR	Differential reflectance
2D	Two-dimensional
mBZ	mini Brillouin zone
X	Exciton
IX	Interlayer exciton
CB	Conduction band
VB	Valence band
DOS	Density of states
MCMC	Markov chain Monte Carlo
TPSC	Two-particle self-consistent
MCD	Magnetic circular dichroism